ANALYTICAL INVESTIGATION OF REPAIR METHODS FOR FATIGUE CRACKS IN STEEL BRIDGES

By

Temple I. Richardson

Submitted to the graduate degree program in Civil, Environmental and Architectural Engineering and the Graduate Faculty of the University of Kansas in partial fulfillment of the requirements for the degree of Master of Science.

_____

Co-Chairperson Dr. Caroline Bennett

_____

Co-Chairperson Dr. Adolfo Matamoros

_____

Dr. Stanley Rolfe

Date Defended: May 25, 2012

The Thesis Committee for Temple I. Richardson
certifies that this is the approved version of the following thesis:

ANALYTICAL INVESTIGATION OF REPAIR METHODS FOR FATIGUE
CRACKS IN STEEL BRIDGES

_____

Co-Chairperson Dr. Caroline Bennett

_____

Co-Chairperson Dr. Adolfo Matamoros

_____

Dr. Stanley Rolfe

Date approved: May 31, 2012

EXECUTIVE SUMMARY

Numerous retrofits have been used to stop distortion-induced fatigue cracks from initiating and propagating in steel bridges. Some decrease stiffness in the web gap region to transfer the load path to an area of higher stiffness, while others increase the stiffness of the region to increase the capacity of the flexible web gap. The behavior of a bridge once a retrofit has been applied needs to be carefully considered because some retrofits may cause cracks to initiate in other locations or increase crack propagation rates. An analytical investigation of numerous retrofits is presented herein on a 2.7-m (9-ft) and a full bridge model with comparisons to configurations prior to retrofit application. This research is presented to extend the number of retrofit options to bridge maintenance engineers.

This thesis is divided into three parts. Part I, "Evaluation of the Performance of Retrofit Measures for Distortion Induced Fatigue Using Finite Element Analysis" was presented at the joint conference of the National Steel Bridge Alliance and the World Steel Bridge Symposium in April 2012. The second part, "Finite Element Modeling Techniques for Crack Prediction and Control in Steel Bridge Girders" will be submitted for later publication. The final section, "Repair of Distortion-Induced Fatigue Cracks on 135-87-43/44 over Chisholm Creek" is a precursor to a final report that will be presented to the Kansas Department of Transportation.

ACKNOWLEDGEMENTS

TABLE OF CONTENTS

Part I: Evaluation of the Performance of Retrofit Measures for Distortion Induced Fatigue Using Finite Element Analysis

Part II: Finite Element Modeling Techniques for Crack Prediction and Control in Steel Bridge Girders

Part III: Repair of Distortion-Induced Fatigue Cracks on 135-87-43/44 over Chisholm Creek

Appendix A: Original 1964 Bridge Plans

Appendix B: Bolt Modeling Techniques

LIST OF TABLES

LIST OF FIGURES

Part I: Evaluation of the Performance of Retrofit Measures for Distortion Induced Fatigue Using Finite Element Analysis

Part II: Finite Element Modeling Techniques for Crack Prediction and Control in Steel Bridge Girders

Part III: Repair of Distortion-Induced Fatigue Cracks on 135-87-43/44 over Chisholm Creek

Appendix A: Original 1964 Bridge Plans

Appendix B: Bolt Modeling Techniques

PART I: EVALUATION OF THE PERFORMANCE OF RETROFIT MEASURES FOR DISTORTION INDUCED FATIGUE USING FINITE ELEMENT ANALYSIS

T.I. Richardson[1], F. Alemdar[2], C.R. Bennett[3], A.B. Matamoros[4], S.T. Rolfe[5]

Abstract

Many existing steel girder bridges designed prior to the mid-1980s were fabricated leaving a flexible gap in the girder web, between the connection plate of transverse cross frames and the girder flange. These flexible web gaps are susceptible to out-of-plane distortion damage due to transverse forces induced by cross-frame forces when the adjacent girder is subjected to a larger deflection. Various retrofit measures have been developed to address this problem including the drilling of crack-arrest holes, installation of tensioned bolts, use of composite materials, back-up stiffeners, and installation of steel angles to directly transfer the forces from the connection plate to the flange. All these measures are intended to reduce the rate of growth of the cracks and to prevent the further initiation of cracks.

This study focuses on evaluating retrofit measures for steel bridges with distortion-induced fatigue damage. Simulations using finite element models (FEM) were performed to analyze the complex stress field that develops in the web-gap region of bridge girders affected by distortion-induced fatigue. The Extended Finite Element Method (XFEM) was used to study the stress field

University of Kansas, 1530 W. 15th St., Lawrence, KS 66045
[1]Temple I. Richardson, Graduate Research Assistant, University of Kansas, temple10@ku.edu
[2] Fatih Alemdar, Graduate Research Assistant, University of Kansas, alemdar@ku.edu
[3] Caroline R. Bennett, PhD, Assistant Professor, University of Kansas, crb@ku.edu
[4] Adolfo B. Matamoros, PhD, Associate Professor, University of Kansas, abm@ku.edu
[5] Stanley T. Rolfe, PhD, A.P. Learned Distinguished Professor, University of Kansas, srolfe@ku.edu

in the web-gap regions of girders with existing fatigue cracks and the potential for crack growth after a retrofit measure has been installed.

Finite element models created using ABAQUS 6.10 were calibrated with experimental results from 9-ft girder assemblies that were tested under fatigue loading. The calibrated models were used to evaluate the expected performance of various retrofit measures in terms of the effect of the retrofit measure on stresses and the potential for existing crack growth.

Simulation results show that two newly developed retrofit measures utilizing composite materials and attaching steel angles to the connection plate and web of the girder were the most effective in reducing the potential for further fatigue damage.

Introduction

Background

Damage due to distortion-induced fatigue is a problem commonly found in structural steel bridges built prior to the mid-1980s. This type of fatigue damage often occurs in cross-frame-to-girder connections, in an area called the web gap region, and is caused by the action of secondary stresses neglected during the original design of the structure. A web gap can be described as a short length of a girder web bounded on one end by the girder flange and on the other by the termination of the cross-frame connection stiffener. When the connection stiffener is not attached to the girder flange, a short flexible segment of girder web is created between the connection stiffener and the girder flange that must transfer the out-of-plane forces induced in the cross frame to the slab or girder flange. The problem is exacerbated by the presence of geometric discontinuities that give rise to stress concentrations in this region of the girder. Two locations in the web gap that are particularly vulnerable to fatigue damage are the connection

stiffener-to-web weld and the flange-to-web weld. The combination of high stress and geometric discontinuities in these two locations often leads to the formation of fatigue cracks.

When secondary stresses lead to cracking in the web gap region, bridge engineers are faced with designing an appropriate retrofit measure to completely halt crack propagation or at least reduce the rate of crack growth so the fatigue life of the bridge can be extended while other options are pursued. A "toolkit" of existing retrofit techniques for distortion-induced fatigue are currently available for this purpose, including drilling crack-arrest holes; stiffening the web gap region by providing a direct connection of the stiffener with the flange; and softening the web gap region through removal of material from the connection stiffener.

The most common measure applied to bridges with fatigue cracks consists of drilling crack-arrest holes at the tips of cracks. This technique is intended to eliminate the sharp termination of the crack and replace it with a smooth radius, lowering crack growth propensity by reducing the stress-concentration factor. Expressions to calculate the diameter of crack-arrest holes have been proposed (1) based on experimental results from steel plates subjected to in-plane stresses (Eq. 1).

$$\frac{\Delta K}{\sqrt{\rho}} < 10\sqrt{\sigma_y} \qquad\qquad (Eq.1)$$

In Eq. 1 the crack-arrest hole diameter, ρ, depends on the stress intensity factor, K, and the yield strength of the material, σ_y. Although Eq. 1 was not developed for out-of-plane fatigue loading (1), crack-arrest holes proportioned with this equation are often employed to temporarily halt the propagation of fatigue cracks caused by distortion-induced fatigue because the drilling of the hole serves to eliminate the sharp tip at the end of the crack. When cracks re-initiate and

3

continue to propagate, more holes are drilled, resulting in a progressive weakening of the web gap region. In a study performed by Fisher (2), the diameter of crack arrest holes varied from 19 to 76 mm (0.75 to 3 in.).

Roddis and Zhao (3) performed high-resolution computer simulations to compare the relative performance of introducing a slot in the connection stiffener, intended to reduce the stress at the web gap by making the cross-frame-to-girder connection more flexible, and a retrofit measure consisting of welding the connection stiffener to the compression flange, which reduces the stress at the web gap by adding connectivity between the stiffener and the flange. In the case study presented the authors concluded that the slotting retrofit measure was ineffective, and a final repair was recommended in which the connection stiffener was welded to the compression flanges. While the geometry of the slot used by Roddis and Zhao (3) could have been modified following the recommendations by Fisher (2) to improve its effectiveness, FE results showed that the reduction in stress at the web gap region associated with creating connectivity between the stiffener and the flange was indicative of excellent performance.

Not all retrofit measures that rely on stiffening of the connection lead to the same outcome. For example, welding a connection plate to a tension flange introduces a fatigue-vulnerable detail that may allow for reinitiation of a fatigue crack and propagation into a flange. To avoid this type of damage, many State Departments of Transportations (DOTs) have implemented a repair that consists of adding connectivity by bolting double angles to the connection stiffener and the flange. In cases where the fatigue damage is at the top of the web, this procedure can require removal of a concrete deck, which is costly and requires traffic disruptions. An alternative similar retrofit involves welding the head of a bolt or piece of threaded rod to the inside face of

the flange, which allows bolting the flange to the connection stiffener without removal of the deck. The main drawback of this technique is that it may introduce a fatigue-vulnerable connection at the weld between the threaded rod and the flange. Given the challenges inherent to the repair of distortion-induced fatigue damage there is a clear and immediate need to develop retrofit measures that are cost-effective, easy to install, minimize the disruptions to ongoing traffic, and most importantly, can be effective without introducing new vulnerabilities to fatigue damage as a "side effect".

Objective

The objective of this study was to evaluate the performance of several retrofit measures for distortion-induced fatigue in steel bridge girders based on analyses of high-resolution 3D finite element models and tests of physical specimens. The scope of this study included examining distortion-induced fatigue in the web gap region of a steel bridge girder with non-skewed cross-frames. The retrofits were primarily examined with the goal of identifying their effectiveness in cracked girder geometry, with the exception of the transverse back-up stiffener and web-to-stiffener angles and backing plate retrofits, which were examined in both cracked and uncracked configurations.

Research Approach

A two-pronged approach was adopted in this research. A coordinated study was performed simultaneously using (1) detailed 3D FEA and (2) physical testing of steel girders under distortion-induced fatigue loads. The two research techniques were used in a complementary manner. For example, results from FEA aided in determining the locations of the physical specimens that were most susceptible to distortion-induced fatigue damage, and also provided a

basis for evaluating the relative performance of the various retrofit techniques. Measurements from the physical specimens were used to calibrate the FE model, so that model characteristics such as the boundary conditions and the mesh density could be refined to best represent the test environment. To adequately describe the coordinated effort, some information concerning the approach is necessary.

Experimental Test Set-up

The test specimens were proportioned such that they were each 2,845-mm (112-in.) long with web dimensions of 876×10 mm ($34.5 \times 3/8$ in.). The width of the top and bottom flanges was 279 mm (11 in.), with the top flange having a thickness of 25 mm (1.0 in.) and the bottom flange width being 16 mm (5/8 in.). In the physical model, the girder specimen was connected to the laboratory floor through a series of channels post-tensioned to the concrete floor, as shown in Figures 1 and 2. The girder was tested upside-down, with the laboratory floor simulating the restraint offered by a concrete bridge deck. The top flange in the laboratory model (*top flange$_{test}$*) reflected behavior for a discretely braced bottom flange in a bridge girder (*bottom flange$_{bridge}$*). The top flange$_{test}$ was restrained at both ends in the out-of-plane direction by angles connected back to a stiff anchorage (a channel member on the load frame), to simulate the restraint effects provided by intermediate cross-frames and lateral flange bending resistance of the bottom flange$_{(bridge)}$. Full-depth stiffeners were provided at the girder ends to ensure web stability in those regions.

Figure 2. View of fascia side of girder specimen

Figure 1. View of girder specimen

The specimen was tested cyclically using load control, with the actuator applying a tensile force with a maximum load of 205 kN (4.6 K) and a minimum of 356 kN (0.8 K). The load was applied to the specimen through an assemblage comprised of a WT section which was directly connected to the actuator at the top, and directly connected to the cross-frame members.

Finite Element Analysis Approach

The specimen and loading apparatus were modeled closely, as shown in Figures3 and 4, using the commercially-available FEA software ABAQUS v6.10. The concrete laboratory floor and the girder tie-down system were simulated in the models. Movement of the actuator in the lateral or longitudinal direction of the girder was prevented. In the simulation, the loading step was divided into five increments, with a static load of 5 kips.
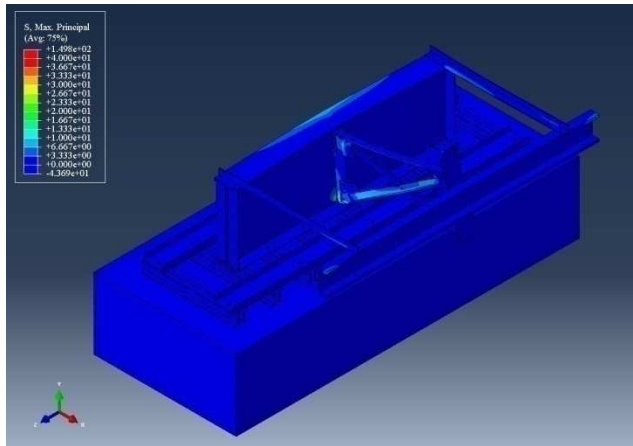
Figure 3. Overall view of girder FE model
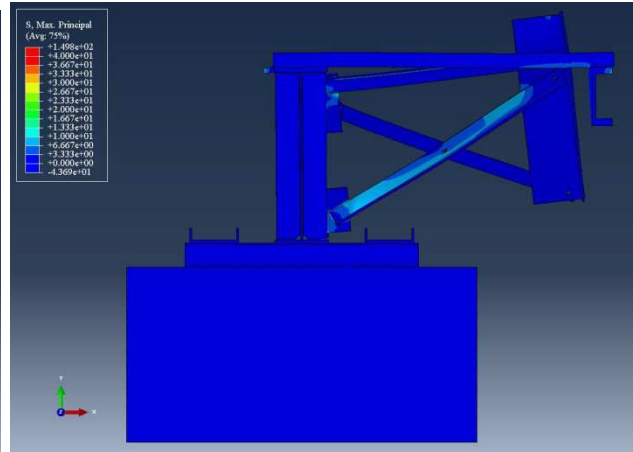
Figure 4. Cross-section view of girder FE model

Table 1. Material properties used in FE model

Material	Modulus of Elasticity, [*MPa (ksi)*]	Poisson's ratio
Steel	200,000 (29,000)	0.3
Concrete	27,800 (4,030)	0.2
Carbon fiber reinforced polymer (CFRP)	Varied between 34,500 – 69,000 (5,000 – 10,000)	0.1

The mesh in the web was determined based on the proximity to the web gap region. The mesh near this region was very dense, with eight-node brick elements sized at 2.54 mm (0.1 in.). Further away from the web gap region the mesh size was 9.53 mm ($^3/_8$ in.). Tetrahedral elements were used to transition between these mesh sizes. Welds also contained hexagonal eight-node brick elements, and were modeled as right triangles. The mesh element size for welds was 2.54 mm (0.1 in.). Tie constraints were used to connect welds to the web and flanges and the cross-braces to the gusset plates. The number of degrees of freedom in each model varied depending

on crack placement and retrofit configuration, and varied from 1 million to 2.5 million degrees of freedom.

Bolts were modeled explicitly, and were composed of three merged parts: the shank, nut, and head. The middle of the shank was partitioned so that a bolt load could be applied to the interior face. The head and shank of the bolt were connected to structural elements using tie constraints. The bolt load was determined based on the recommendations in the AISC Steel Construction Manual (4) based on the specific diameter of the bolt that was used. Bolt tensioning forces were applied in the second loading step of the computer simulations. The actuator load was applied in the third loading step. Although the applied bolt load was removed in this step, the tension force was maintained by keeping the contracted bolt length at the end of the second loading step constant for all subsequent steps. This technique greatly simplified the model and decreased the numerical complexity of the solution, yet still accounted for the tension force in the bolts. In other areas, such as the channels connected to the bottom flange in the test set-up (bottom flange$_{test}$), bolts were not modeled. Instead, the channels were tied to the bottom flange$_{test}$. In areas of greater interest, such as the bottom web gap$_{test}$, actual bolts were modeled explicitly.

Three different techniques for modeling cracks were utilized: explicit modeling of the cracks, the Extended Finite Element Method (XFEM), and contour integrals. Differences in the characteristics of the models and the types of outputs that were needed dictated the selection of the crack modeling technique.

Cracks were modeled explicitly by removing elements from the web. Crack width was dependent upon the mesh density, so the mesh in the web gap region was set to 0.6 mm (0.02 in.)

initially. The run time was longer than average in these models because the mesh was required to be very dense.

Cracks were also simulated through the use of the Extended Finite Element Method (XFEM). A major benefit of this numerical method over explicitly modeling cracks is that the finite element mesh is independent of the crack geometry. This can be advantageous when a crack is allowed to propagate in the XFEM simulation, and also because the crack does not need to align with element boundaries. Enrichment functions are added to the approximation space near crack tips (5). In XFEM simulations, the part containing a crack was partitioned such that the area around the crack tip could be selected for enrichment. When a fixed area around the crack tip was enriched, as opposed to just the nodes around the crack tip, the rate of convergence was greatly increased (5).

In the retrofits examined, a crack with a predefined length and no propagation was used for retrofit comparison. In the XFEM simulations, cracks were modeled as 3D planar parts and the depth of the crack was set to the thickness of the web, 9.5 mm (0.375 in.). One of the limitations of the XFEM technique was that in many instances, when cracks intersected a boundary between model parts, the elements became distorted and the cracks did not open. This limitation was overcome by placing the cracks a very small distance, 0.25 mm (0.01 in.), away from the part boundary. Enrichment functions could not be added to a crack tip that is located where elements are not present. An example of this situation is a crack truncating into a crack-arrest hole. In this situation, explicit cracks were modeled in place of the XFEM technique. When using XFEM, J-Integral values could be obtained from each crack. *J*-integral results have been presented alongside HSS results for Retrofit 6, discussed in the Results section.

Finally, cracks were also simulated and analyzed using contour integrals. This technique was implemented to calculate contour integrals in the area surrounding the tip of the cracks, such as the *J*-integral, to be used as a measure of the potential for crack re-initiation in models with retrofit measures. When this method was used, the web was partitioned to have a small circle at each crack tip. The diameter of the circle was 5.1 mm (0.2 in.). The direction of crack growth was specified by the *q*-vector, defined in terms of the starting point of the crack and the crack tip. For cracks below the connection plate two *q*-vectors were specified, allowing both crack tips to grow. After the *q*-vector was defined, a seam was placed in the web which functioned as the crack. The *q*-vector was defined to act in the direction of the cracking paths noted in Figure 5a.

Evaluation of Crack Growth Propensity and Retrofit Effectiveness

When examining FE simulation results, it is important to use meaningful comparative measures of stress between models. Using maximum stresses as the measure for comparison is likely to provide an inaccurate comparison because it is sensitive to mesh size, particularly in areas of web gap regions with very large stress gradients.

Hot Spot Stress Technique

The Hot Spot Stress (HSS) technique was used to quantify the stress near welds and geometric discontinuities. The two welds of particular interest were the connection stiffener-to-web weld and the web-to-bottom flange$_{(test)}$ weld. Two hot spot stress paths were defined to capture maximum principal stresses in the regions directly surrounding those two welds. The paths were located half the thickness of the web away from each of the welds, and maximum principal stresses were extracted from each element on the path. The greatest maximum principal stress from each path was selected as the basis of comparison with HSS from other models. The

magnitudes of the stresses obtained using the HSS techniques are sensitive to mesh size and the distance between the point of extraction of the stress and the weld toe. A convergence study was performed to determine the appropriate mesh size in the web gap region. Based on this study, the mesh size of the web in the web gap region was set to 2.54 mm (0.1 in.).

Two different hot spot stress paths were considered in this study: HSS1 and HSS2. When a crack along the stiffener-to-web weld toe was modeled (referred to as a *horseshoe-shaped crack*), the HSS path used was labeled HSS1. The HSS1 path was defined at a distance of half the thickness of the web away from the weld toe, but the path was always parallel to the crack geometry. If a crack was present along the toe of the weld connecting the web to the flange (referred to herein as a *horizontal crack*), a HSS path was taken 5 mm (0.2 in.) away from the weld toe (in the web), parallel to the crack. Paths taken parallel to a crack in the web-to-flange weld were labeled HSS2.

Figure 5. (a) presents the location of the cracks modeled, and Figure 5b shows the two HSS paths considered in the bottom web gap$_{(test)}$. In scenarios where crack length was varied, cracks were symmetric about mid-thickness of the stiffener. When comparing retrofits with varying crack lengths, the HSS path lengths were always kept constant. Therefore, the length of HSS2 was maintained at 203 mm (8 in.) and the height of HSS1 maintained at 102 mm (4 in.), regardless of the crack length examined. This approach allowed for the maximum principal stresses to be extracted for every element along the two paths in the various models; the reported HSS value for each path always corresponded to the greatest value of maximum principal stress along that path for the model being examined.

(a)   **(b)**
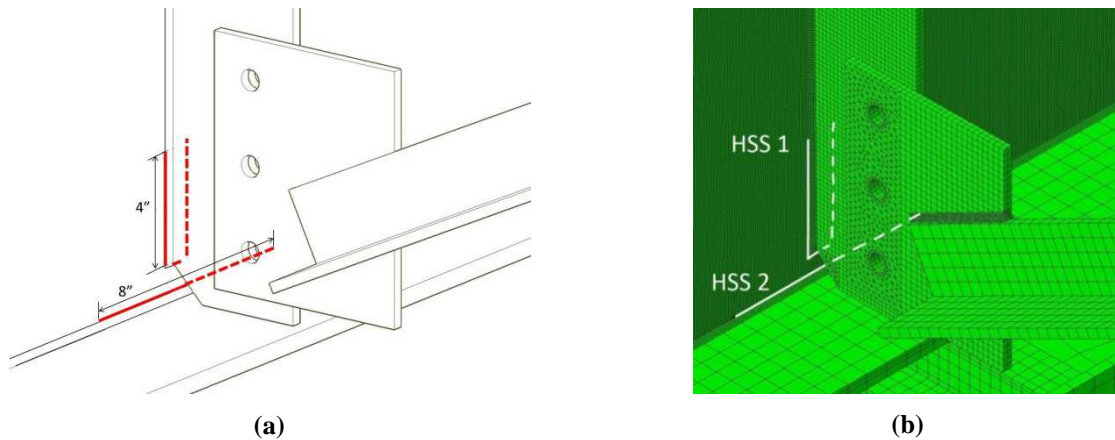
Figure 5. (a) Diagram of modeled 4-in. long horseshoe-shaped crack and 8-in. long horizontal crack geometry at weld toes; redlines represent modeled cracks.; (b) Location of HSS extraction paths, HSS1 and HSS2, in the bottom web gap(test)

J-Integral

The *J*-Integral is a path-independent contour integral that captures the energy released from a crack when it grows (7). It estimates the energy released at the crack tip by selecting a path a certain distance away from the assumed inelastic region present around the crack tip. In some models, it was found that the *J*-Integral was better suited than the Hot Spot Stress (HSS) technique for comparing the effectiveness of different retrofit measures because in some models the mesh had to be redefined to accommodate the retrofit measure. For example, the web mesh had to be redefined for angle-retrofit measures that required bolt holes. When *J*-Integral values were calculated, the contour integrals were defined at the tip of the crack. Five contour integrals were defined at planes that intersected the crack at different points through the thickness of the web, and *J*-Integral values were extracted from the plane located on the tension face of the web. *J*-Integrals from the fifth contour were used for comparison because the energy tends to converge with increasing number of contours.

ABAQUS calculates the *J*-integral in two ways. The first is by direct computation using well-established equations (1). The second is by calculating the *J*-Integral on the basis of the stress-

13

intensity factors. In the web gap region where multiple crack surface displacements are possible (Modes I, II, and III), Equation 2 was used:

$$J = \frac{1}{E}\left(K_I^2 + K_{II}^2\right) + \frac{1}{2G}\left(K_{III}^2\right)$$
(Equation 2)

Where K_I, K_{II}, and K_{III} are stress intensity factors corresponding to Mode I, II, and III displacements, $E' = E/(1-v^2)$ for plane strain, E is Young's modulus, v is Poisson's ratio, and G is the shear modulus (7).

Experimental Results

Two specimens, designated Specimen 1 and Specimen 2, were tested in the structures laboratory at the University of Kansas. The results from these two tests are discussed in the following section.

Crack Initiation/Growth Sequence

In the first specimen (Specimen 1), a 38-mm (1.5-in.) long crack was fabricated 20 mm (0.8 in.) below the connection stiffener-to-web weld. The intent of fabricating a crack prior to loading was to control the location and length of cracks at the start of the tests. Contrary to what was expected, the crack tips grew down towards the web-to-flange weld at the bottom flange$_{(test)}$, and a second crack quickly initiated at the connection stiffener-to-web weld. Figures 6 and 7 present the simulation results for Specimen 1, with the experimentally-observed cracking superimposed. It can be readily observed that excellent agreement was observed between the maximum principal stresses calculated with the finite element model and the experimentally observed crack locations. It should be noted that the connection stiffener was removed from view in Figure7.

Based on the findings from the first physical test, no pre-existing cracks were fabricated in Specimen 2. The first crack that formed in Specimen 2 was found at the connection stiffener-to-web weld. After the formation of this crack, the bottom flange$_{(test)}$-to-web weld developed a horizontal crack that quickly propagated.

Figure 6. Overall view of specimen, with bottom web gap$_{(test)}$ shown by the circle.
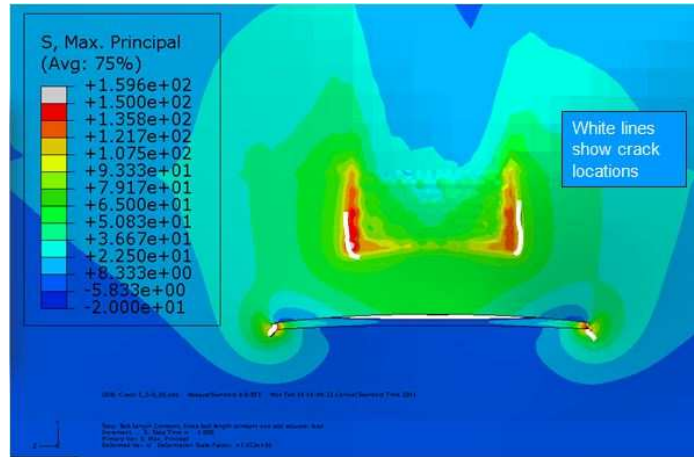
Figure 7. View of maximum principal stress contours in the cracked web gap region in the finite element model of Specimen 1. Superimposed white lines represent experimentally-observed cracks locations.

Finite Element Analysis Results

Unretrofitted Performance

In simulations of unretrofitted, uncracked models very high stresses were found at the toe of the weld between the web and the connection plate (Figures 8a and 8b). On the fascia side of the girder, in the bottom web gap of the specimen, an area of high stress was found at the web-to-bottom flange$_{(test)}$weld. Cracks formed in both of these areas in the bottom web gap during the experiment. In Specimen 2, horseshoe-shaped cracks first formed at the toe of the connection stiffener-to-web weld, followed by cracks at the web-to-bottom flange$_{(test)}$ weld. The

experimentally-observed crack pattern was in close agreement with locations of peak maximum principal stress calculated with the FE models. In Specimen 2, the horseshoe-shaped and horizontal cracks were allowed to grow to 102 mm (4 in.) and 203 mm (8 in.), respectively. This particular crack configuration was modeled, and increases of 4.5× and 25× were calculated for the magnitudes of HSS1 and HSS2, respectively, when compared with computed values from the uncracked configuration.

A small region of high stress was also noted in the top web gap on the fascia side of the web during simulations of unretrofitted specimens. During the test of Specimen 2, cracks were observed in the top web gap$_{(test)}$ after cracks had initiated and propagated in the bottom web gap$_{(test)}$.

Retrofit Measures

A series of retrofit measures were investigated analytically, some of which were also investigated experimentally. Retrofit measures discussed herein include (1) use of crack-arrest holes, (2) installation of tensioned bolts in crack-arrest holes, (3) use of transverse back-up stiffeners, (4) composite blocks, (5) bolted angles connecting the stiffener to the bottom flange$_{(test)}$, and (6) bolted angles connecting the stiffener to the web along with a steel backing plate. Of these techniques, retrofit measures (1) and (6) were also applied to test specimens. All techniques are addressed in the following discussion.

Retrofit Measure 1: Crack-Arrest Holes

Retrofit measure 1 was studied both analytically and experimentally. In the physical Specimen 2, two 19 mm ($^3/_4$in.) diameter crack-arrest holes were drilled at the tips of the 102-mm (4-in.)

horseshoe-shaped crack along the connection plate weld and also at the tips of the 203-mm (8-in.) horizontal crack along the bottom flange weld. The holes were drilled as close to the crack tips as possible to remove the sharp crack tip. In some cases, portions of the connection plate-to-web weld had to be removed to achieve this end result.

This retrofit measure was modeled in the simulations, and is shown in Figures 9a and 9b. Cracks were modeled explicitly with a thickness equal to one element width, which was set to 2.54 mm (0.1 in.). The stress distribution in Figure9b shows that there were very high stresses in the immediate vicinity of the crack stop holes, along the connection stiffener weld. The calculated value of HSS 1 decreased by 38% after the holes were drilled. Although the reduction in the stress was meaningful for HSS 1, the calculated stress in the model without the crack stop holes was so high that the reduction in stress was not expected to prevent cracks from re-initiating.

In Specimen 2, cracks indeed re-initiated a relatively small number of cycles after the holes were drilled, which was in agreement with results from the computer simulations. The length of the horseshoe-shaped crack before the crack-arrest holes were drilled was 102 mm (4 in.), and after the holes were drilled, the horseshoe-shaped crack grew to 70 mm (2.75 in.) in 39,700 cycles. A photograph depicting the crack pattern and crack-arrest hole placement is provided in Figure 9.(c).

Retrofit Measure 2: Tensioned Bolts and Square Washers

Retrofit measure 2 was studied analytically. In this case 19-mm (0.75 in.) diameter tensioned bolts were inserted into the crack-arrest holes with the intent of applying a compressive stress to the crack tip. A view of this retrofit on the fascia and interior of the web is shown in Figure10. In addition to tensioned bolts, 25 × 25-mm (1 × 1-in.) square washers were added to the fascia

side of the web to investigate if the compressive stress could be distributed over a larger area. It was found that neither method significantly reduced the stress at the connection stiffener-to-web weld. Also, it should be noted that this type of retrofit is not possible to construct for all crack configurations because a bolt cannot always fit in geometrically constrained areas. In these simulations, this retrofit was possible only when the crack was at least 38 mm (1.5 in.) below the weld toe.

| (a) | (b) |
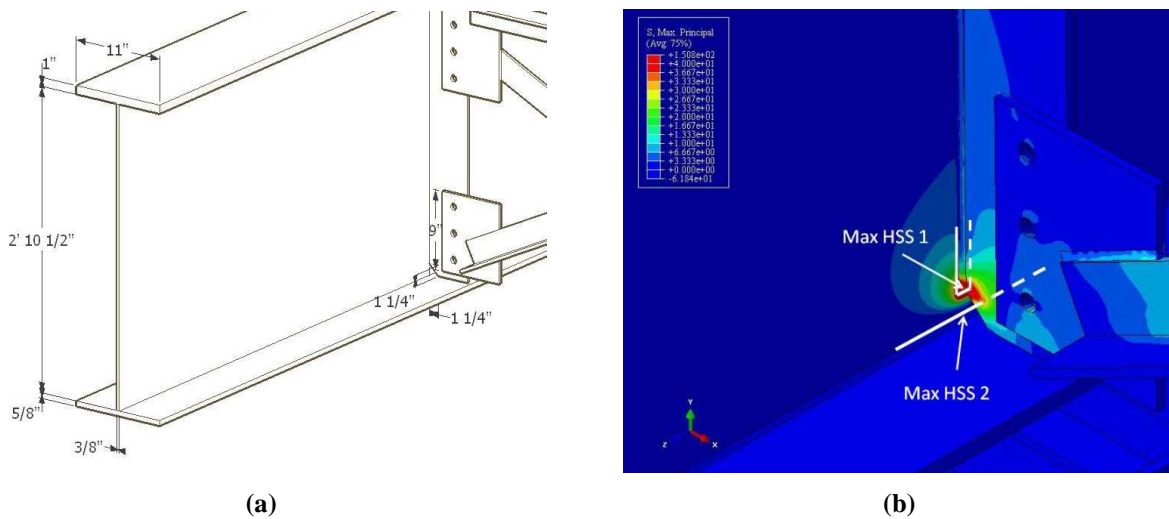
Figure 8. (a) Schematic of unretrofitted web gap region; (b) Maximum principal stress contour plot for unretrofitted web gap region (no cracks modeled); arrows point to point of highest maximum principal stress along HSS Paths 1 and 2.

| (a) | (b) |
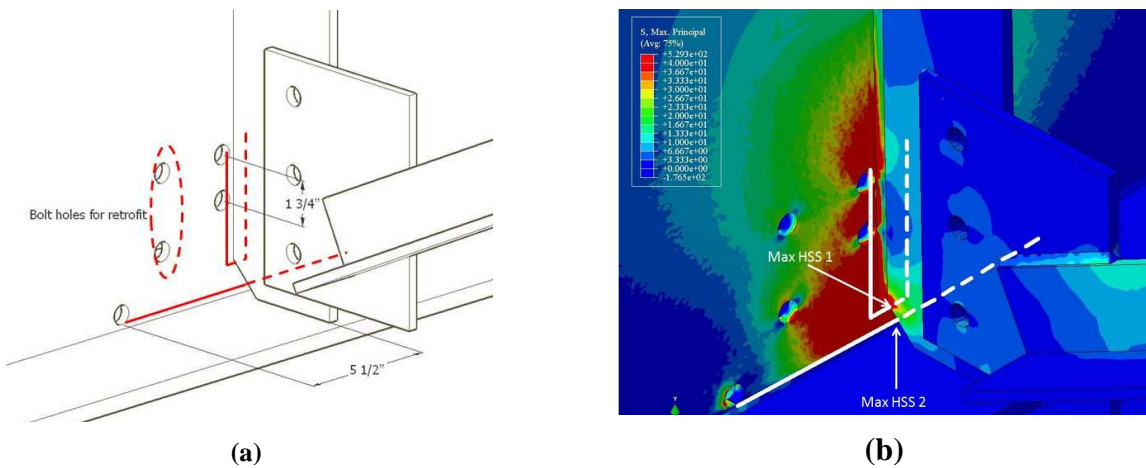
(c)

Figure 9: Retrofit measure 1: drilled crack-arrest holes (a) Schematic of drilled crack-arrest holes, where redlines represent hot spot paths; (b) Maximum principal stress contour plot (cracks modeled explicitly); arrows point to point of highest maximum principal stress along HSS Paths 1 and 2; (c) Photograph of cracking pattern on fascia side of girder. Horseshoe-shaped cracking is visible, horizontal crack has been highlighted in yellow.
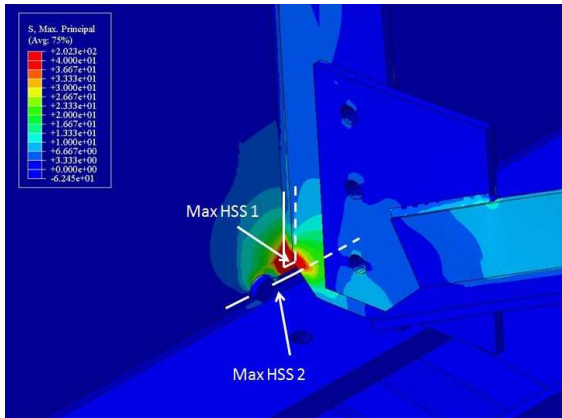
(a)
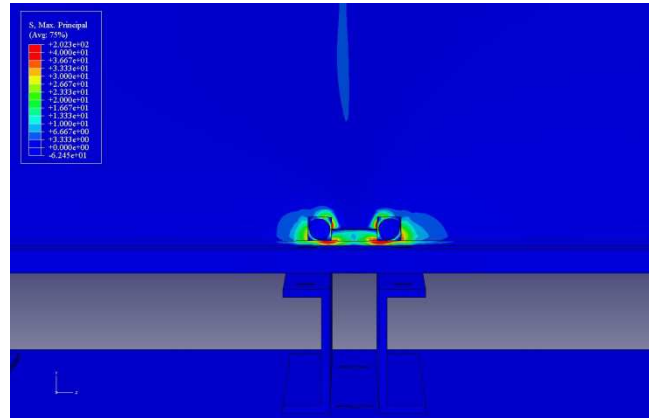
(b)

Figure 10. Retrofit measure 2: Tensioned bolts (a) view of stress contour plot for interior face of girder; (b) view of maximum principal stress contour plot for fascia side of girder; cracks modeled explicitly; arrows point to point of highest maximum principal stress along HSS Paths 1 and 2.
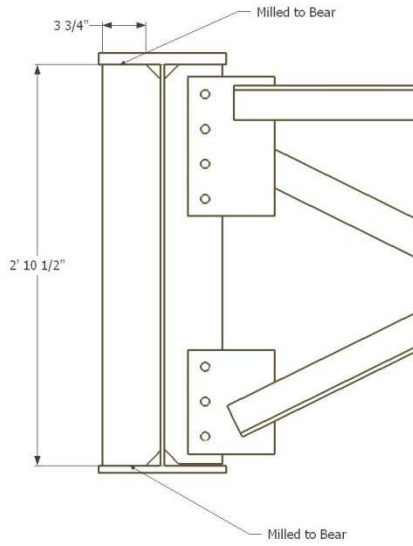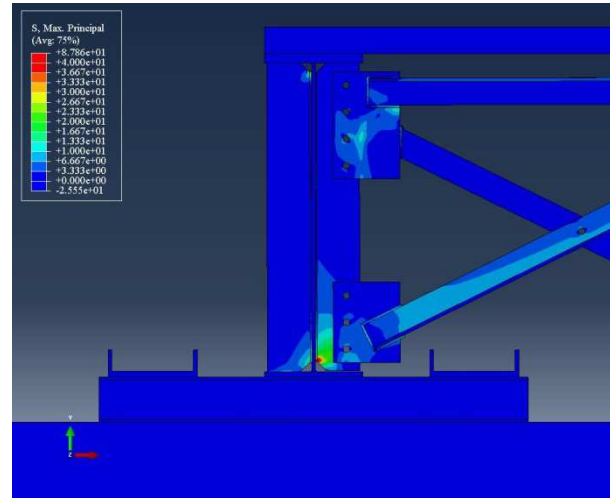
(a)   **(b)**

Figure 11. Retrofit measure 3a: (a) Schematic of full-depth transverse back-up stiffener; (b) Maximum principal stress contour plot for full-depth transverse back-up stiffener; cracks modeled using XFEM
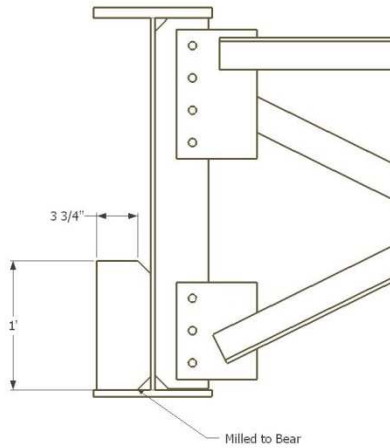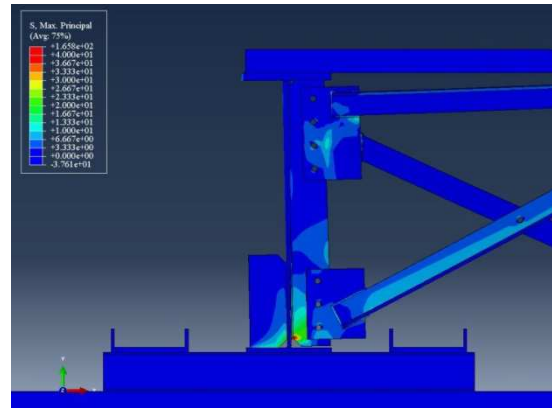
(a)   **(b)**

Figure 12. Retrofit measure 3b: (a) Schematic of partial-depth transverse back-up stiffener; (b) Maximum principal stress contour plot for305-mm (12-in.) partial-depth transverse back-up stiffener; cracks modeled using XFEM

(a)   **(b)**
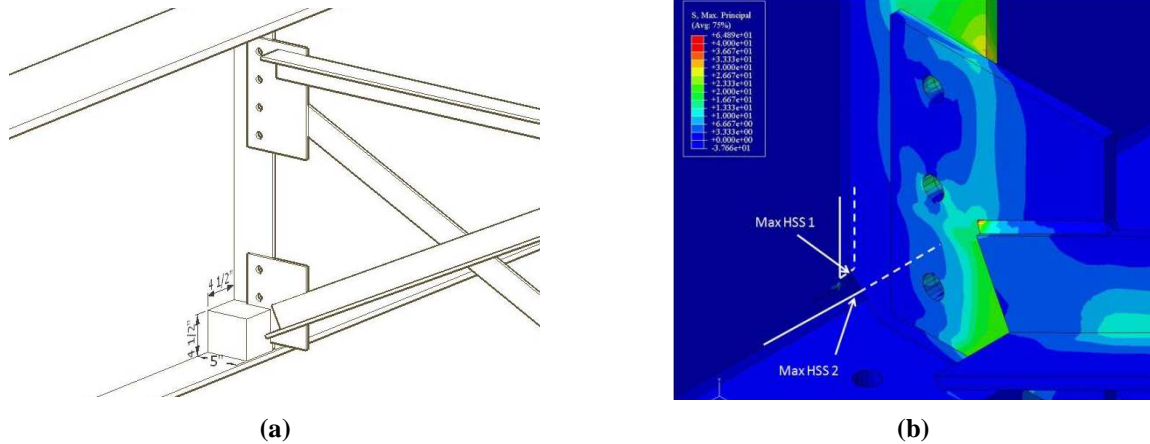
Figure 13. Retrofit measure 4: (a) Schematic of modeled geometry for the CFRP block (b) Maximum principal stress contour plot for steel beneath composite block; Cracks modeled explicitly. Arrows point to point of highest maximum principal stress along HSS Paths 1 and 2.

(a)   **(b)**
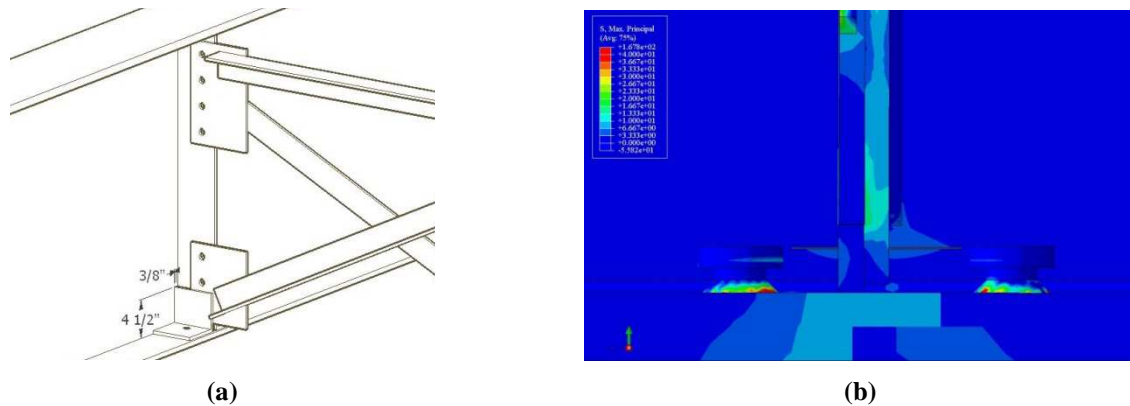
Figure 14. Retrofit measure 5: (a) Schematic of bolted stiffener-to-flange double angles modeled; (b) Maximum principal stress contour plot showing welded bolts at inside face of flange.

Retrofit Measure 3: Transverse Back-up Stiffeners

Retrofit 3 was studied analytically, and two different back-up stiffener geometries were considered. The first was a full-depth back-up stiffener welded to the web, with bearing interaction between the stiffener and the top and bottom flanges$_{(test)}$, which is shown in Figure 11. In the simulations, bearing was achieved by placing a hard contact interaction between the flanges$_{(test)}$ and the stiffener. When comparing models that are unretrofitted with a 102-mm (4-in.) horseshoe-shaped crack and an 203-mm (8-in.) horizontal crack versus models that have the

same crack configuration and are retrofitted with a full back-up stiffener, it was found that HSS1 decreased by 85% and HSS2 decreased by 60% after the retrofit. It is interesting, too, that if the stiffener was added before cracks formed (i.e., used as a preventative measure), HSS1 values decreased by 13%, but HSS2 increased by a factor of 11.

The second back-up stiffener considered was partial depth [305 mm (12 in.)] and was welded to the web with a hard contact placed between the bottom flange$_{(test)}$ and the transverse stiffener. This second configuration can be seen in Figure 12. Comparing a cracked, unretrofitted simulation to a cracked, retrofitted simulation with a partial depth stiffener, it was found that HSS1 and HSS2 decreased by 76% and 36%, respectively, after the retrofit.

The stress in the bottom web gap$_{(test)}$ was allowed to transfer to the backup stiffeners in both configurations. Although HSS1 and HSS2 saw a slightly greater stress reduction with the full depth stiffener as compared to the partial depth stiffener, it should be noted that a localized high area of stress occurred in the weld along the full depth stiffener near the top flange$_{(test)}$, which did not occur in the partial depth stiffener.

Retrofit measure 4: Composite Block

Retrofit 4 was studied analytically on a cracked model. The crack was modeled explicitly as having a length of 64-mm (2.5-in.), and was located 20-mm (0.8-in.) below the connection stiffener weld. A 127×114×114-mm (5×4.5×4.5-in.) composite block was designed to fill the entire web gap region, as shown in Figure 13. Tie constraints were used to attach the composite block to the surrounding steel members in the web gap region. The modulus of elasticity of the composite block was varied from 34,500 to 68,950 MPa (5,000 to 10,000 ksi) to evaluate which most effectively reduced the stress in the bottom web gap, and to test the sensitivity of the stress

in the web gap region to the stiffness of the CFRP material. It was found that varying the modulus of elasticity changed the HSS values in the steel substrate by less than 0.5%.

Parts made out of composite materials can be manufactured to have different sizes and shapes, and tailored to suit a given geometric configuration. The stress field in Figure 13(b) shows that significant stresses remained in the steel substrate at the weld between the cross brace and the connection plate after the composite block was in place. This deficiency could be addressed by manufacturing the composite block to extend over the cross-brace-to-gusset weld. Despite the high stresses at the cross-brace-to-gusset weld, the maximum HSS1 in the region directly covered by the CFRP material was reduced by 93%.

Retrofit measure 5: Bolted Stiffener-to-Flange Angles

Retrofit measure 5, studied analytically, consisted of two angles bolted to the bottom flange$_{(test)}$ and welded to the connection stiffener with geometry as shown in Figure 14(a). This retrofit in an actual bridge would often require drilling through the concrete deck to install the bolts, which is not a simple solution. To avoid drilling through the deck, bolts or studs may instead be welded to the inside face of the top flange$_{(bridge)}$. This retrofit was applied in a simulation with a 64-mm (2.5-in.) crack, modeled explicitly, which was placed 20-mm (0.8-in.) below the connection stiffener-to-web weld. It was found that HSS1 decreased by 95% in the web gap region after application of this retrofit, but a new fatigue prone detail was introduced at the stud weld. This phenomenon can be noted in Figure 14(b).

Retrofit measure 6: Bolted Web-to-Stiffener Angles and Backing Plate

Retrofit measure 6 was studied both analytically and experimentally. This retrofit measure consists of bolting two angles to the web and connection plate, one on each side of the connection plate (Figure 15a; Figure 15c). A backing plate was also bolted to the fascia side of the web to distribute stress away from the bottom web gap$_{(test)}$ (Figure 16(a); Figure 16(c)). As discussed in the following, thicknesses of the back-to-back steel angles and the back plate were varied to investigate the impact of the stiffness of the structural components on the stresses in the web gap area. In the simulations, all parts were connected through 19-mm (0.75-in.) diameter A325 bolts. Shims were used on both sides of the connection plate to avoid interferences with the welds.

L6×6×3/4 angles and a 457×203×19-mm (18×8×0.75-in.) backing plate were modeled to reflect the dimensions of the retrofit elements used in the physical simulations. In this model, there was a 102-mm (4-in.) horseshoe-shaped crack and a 203-mm (8-in.) horizontal crack in the bottom web gap$_{(test)}$, dimensions that were consistent with the crack lengths achieved in the physical simulation of the specimen before it was retrofitted. Stresses in the web gap region decreased by 98% for HSS1 and 91% for HSS2after application of retrofit method 6, compared with the unretrofitted case with a 102-mm (4-in.) horseshoe-shaped crack and a 203-mm (8-in.) horizontal crack. Maximum principal stress contours on the interior of the girder can be seen in Figure 15b, and maximum principal stresses in the web under the backing plate are presented in Figure 16b.

The angle thickness, backing plate thickness, and the backing plate length were varied to determine the effect of the retrofit dimensions. The thicknesses of the members were varied from 6 to 25 mm (0.25 to 1.0 in.), and the length of the backing plate was varied from 3045to 914 mm (12 to 36 in.). Models in which the angle and back plate thicknesses were 25 mm (1 in.)

were designated as a *stiff (s)* combination. When both thicknesses were 13 mm (0.5 in.) the combination was designated as *medium-stiff (m)*. The retrofit was designated *flexible (f)* when both thicknesses were 6-mm (0.25-in.) thick. Other combinations were also considered, in which the backing plate thickness was different from the angle thickness. Computed stresses at the bottom web gap$_{(test)}$are listed in Table 2 for various stiffness combinations of retrofit measure 6. When a flexible combination was used, the HSS values in the web gap were found to be more than twice as great as those calculated for a stiff combination, although in all models the stresses were significantly lower than for the model without the retrofit. The variation in HSS between the various stiffnesses of retrofit measure 6 only account for approximately 5% of the maximum unretrofitted HSS.

Table 2. Comparison of HSS values for different retrofit stiffnesses for models with a 102 mm (4 in.) horseshoe-shaped crack and a 203 mm (8 in.) horizontal crack; Back plate length held constant at 18 in.

Model Name	HSS 1 MPa (ksi)	HSS 2 MPa (ksi)
1" thick	23 (3.0)	58 (8.3)
0.5" thick	60 (8.6)	45 (6.5)
0.25" thick	68 (9.8)	55 (8.0)

(b)
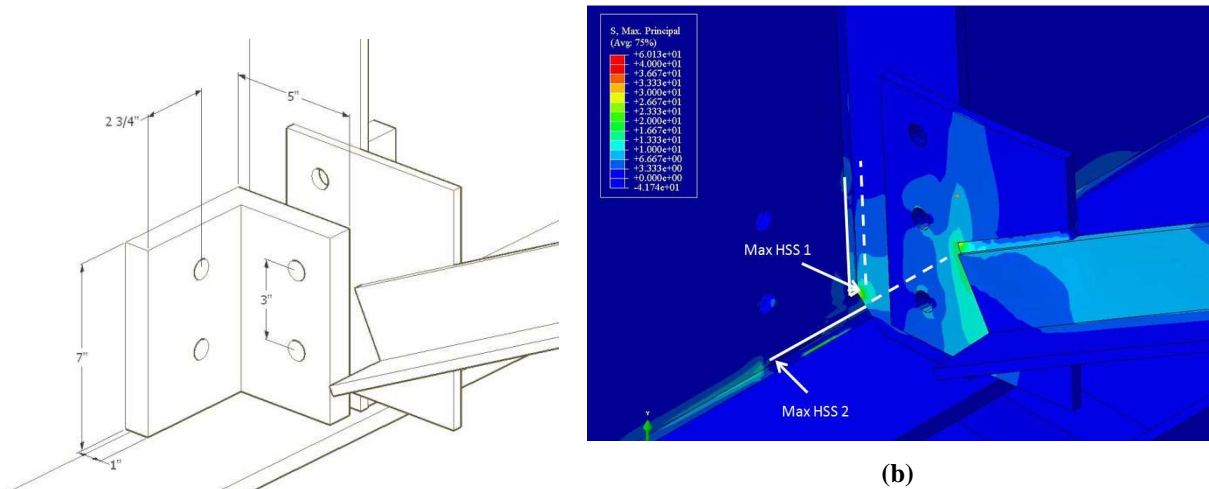
(c)

Figure 15. Retrofit measure 6: (a) Schematic of retrofit 6 (interior view); (b) Maximum principal stress contours in the web gap region with the angles removed from view; arrows point to point of highest maximum principal stress along HSS Paths 1 and 2. Cracks were modeled with XFEM and contour integrals. (c) Photograph of interior side of girder with stiffener-to-web angle and backing plate retrofit.
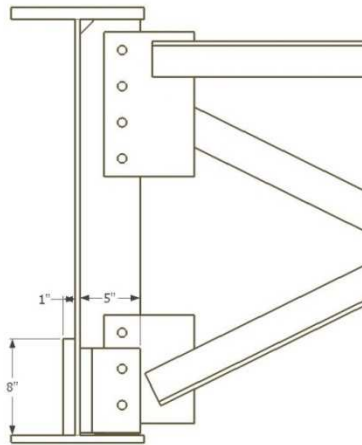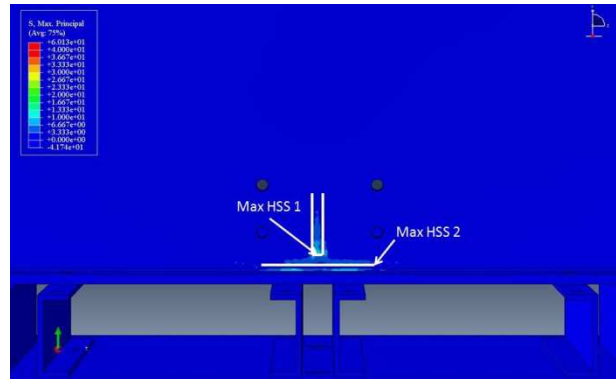
(a)   **(b)**

(c)

Figure 16. Retrofit measure 6: (a) 457-mm (18-in. long) backing plate on exterior side of web; (b) Maximum principal stress contours on the exterior side of web with the back plate removed from view; arrows point to point of highest maximum principal stress along HSS Paths 1 and 2. Cracks modeled using XFEM and

When comparing the HSS values for each model, it was found that if the backing plate thickness was kept constant at 25 mm (1.0 in.) (the greatest thickness within the range analyzed), the thickness of the angles had a negligible effect on stress. The opposite also held true; when the angle thickness was kept constant at 25 mm (1.0 in.), the calculated HSS was insensitive to the thickness of the backing plate. Therefore, it was found that choosing the stiffest option for the angle, the backing plate, or both would provide the greatest reduction in the computed stress.

The effect of crack length on the effectiveness of retrofit measure 6 was also analyzed by comparing the computed HSS values. In addition to an uncracked configuration, crack lengths studied were 13 mm, 25 mm, and 102 mm ($^1/_2$ in., 1.0 in., and 4.0 in.) for the horseshoe-shaped crack, and 13 mm, 25 mm, and 203 mm ($^1/_2$ in., 1 in., and 8 in.) for the horizontal crack. The longest crack in both series, 102 mm and 203 mm (4 in. and 8 in.), for the horseshoe-shaped and horizontal cracks respectively, were not equal because they were chosen to represent actual crack lengths measured in the physical model at the end of the experiment.

The effect of crack length on HSS was as follows. When stiff angles or a stiff back plate was used, the maximum HSS1 occurred when there were no cracks present. If both a stiff angle and plate were used, HSS1 values decreased slightly as the crack length increased, and eventually stabilized.

Figure 18 and 19 show that HSS 2 and the J-Integral exhibited common trends as the horizontal crack lengthened. In both figures, a 25.4-mm (1-in.) thick back plate was applied, while the thickness of the angles was varied. HSS2 increased slightly as the crack lengthened, up to a crack length of 13 mm – 25 mm ($^1/_2$ in. – 1 in.), at which point stress in the horizontal crack

decreased with further increase in crack length. These findings are important because they shed light on the effect of crack growth on stress when the retrofit is implemented. For the crack lengths studied, it was found that configurations with intermediate crack lengths of 25 mm (1.0 in.) at the web-to-bottom flange$_{(test)}$ weld produced the greatest demands on the retrofit.
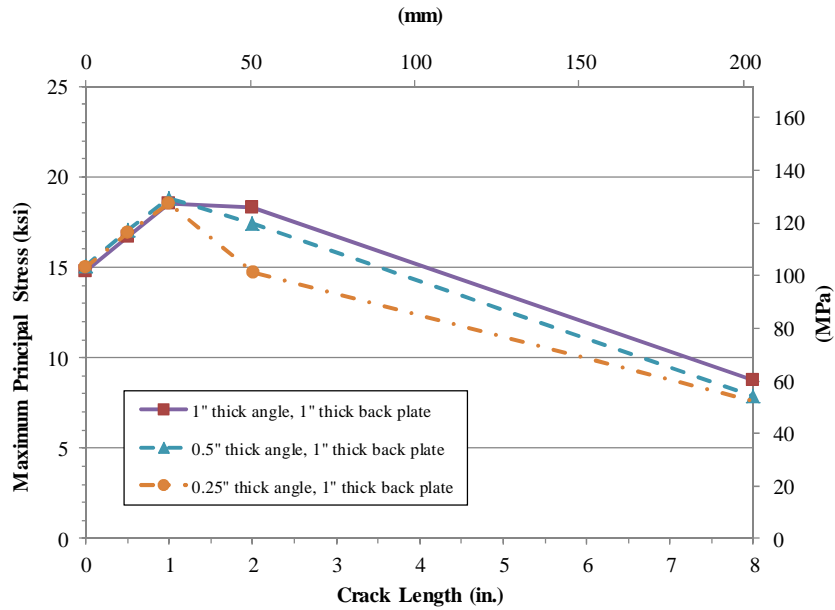
Figure 17. Change in maximum principal stress along HSS path 2 (horizontal web-to-flange weld) as crack length increased.
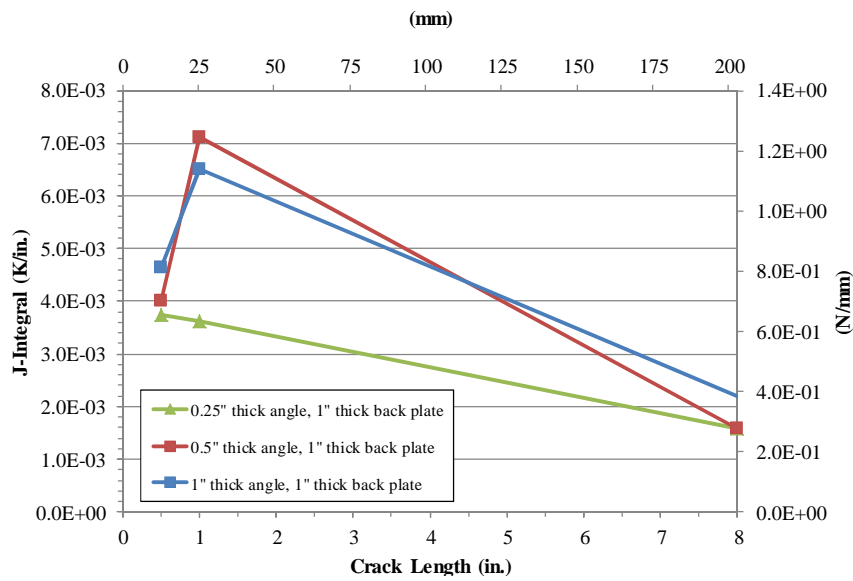
Figure 18. Change in J-Integral for horizontal web-to-flange weld crack as crack length increased.

As mentioned, the bolted web-to-stiffener angles with backing plate retrofit was modeled on cracked and uncracked specimen geometries to examine the effectiveness of the retrofit if used as a preventative measure. It was seen that HSS 1 and 2 values were similar in magnitude when comparing retrofitted models with various crack lengths to a retrofitted, uncracked model. When 25 mm (1 in.) thick angles and backing plate were used, the uncracked configuration saw an HSS1 value of 60 MPa (8.7 ksi), while the model with a 102-mm (4-in.) crack had an HSS1 value of 38 MPa (5.5 ksi). Similar results were found for HSS2. The web-to-stiffener angles and backing plate retrofit exhibited a high level of stress reduction for both HSS1 and HSS2 in the web gap region for both the uncracked, retrofitted and the cracked, retrofitted scenarios. Therefore, this retrofit shows merit as a preemptive retrofit technique as well as a post-cracking retrofit technique.
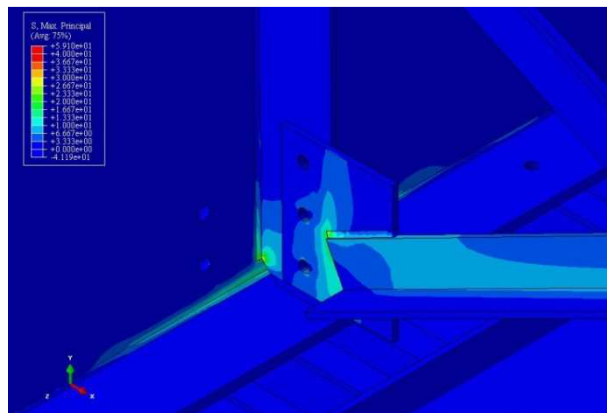
Figure 19. Maximum principal stress contours in an uncracked model with stiff web-to-stiffener angles and backing plate (Retrofit 6) applied.

Conclusions

A study was carried out to evaluate the effectiveness of various retrofit measures for repairing distortion-induced fatigue damage in steel bridge girders. Results from computer and physical simulations have led to the following conclusions:

1. When comparing an uncracked, unretrofitted configuration with an unretrofitted simulation containing a 102 mm (4 in.) horseshoe-shaped crack and a 203 mm (8 in.) long horizontal crack, HSS1 (path parallel to the web-to-stiffener weld) and HSS2 (path parallel to the flange-to-web weld) demands increased by 4.5× and 25×, respectively, after cracks developed. The areas of high stress moved from the weld toe (uncracked, unretrofitted model) to the tips of the cracks (cracked, unretrofitted model).

2. Computer simulations showed that the web-to-stiffener angle retrofit (retrofit 6) and the composite block (retrofit 4) were the most successful at reducing the calculated stress in the bottom web gap region. Computer simulations of models with retrofit measure 4 (composite block) reduced the HSS1 by 93%. The calculated stress in the bottom web gap for retrofit 6 with a stiff angle and backing plate reduced HSS1 by 98% and HSS2 by 91%, for a configuration with a 102-mm (4-in.) horseshoe-shaped and 203-mm (8-in.) horizontal crack.

3. The web-to-stiffener angles and backing plate retrofit (retrofit 6) exhibited a high level of stress reduction for both HSS1 and HSS2 in the web gap region for both the uncracked, retrofitted and the cracked, retrofitted scenarios. Therefore, this retrofit shows merit as a preemptive retrofit technique as well as a post-cracking retrofit technique.

4. For retrofit measure 6 (stiffener-to-web angles and backing plate), configurations with either the angles or the backing plate as stiff elements (or both as stiff elements) produced the greatest reduction in stress at the web gap region.

5. Drilling of crack-arrest holes (retrofit measure 1) at the ends of cracks resulted in negligible reductions in hot spot stress in the web gap region, and the general state of stress in the web gap region remained very significant. The poor performance of this

retrofit measure in the computer simulations was corroborated by reinitiation of cracking in the physical specimen after only 39,700 cycles.

6. Installation of a tensioned bolt and plate washer in crack-arrest holes (retrofit measure 2) had a negligible effect on stress in the web gap region, and was concluded to be ineffective.

7. The full depth back-up stiffener reduced the stress in the web gap region more than the partial depth back-up stiffener, but corresponded with a very localized stress increase on the fascia side of the web near the top flange$_{(test)}$.

The primary goal of this study was to evaluate the relative performance of retrofit techniques for distortion-induced fatigue in steel bridge girders. The study showed that the use of angles to attach the connection stiffener to the web with the addition of a backing plate significantly reduced stresses in the web gap region. This is an important finding, because this technique is expected to be inexpensive and easy to install in the field, without significant disruptions to traffic or removal of a concrete deck. Findings regarding the effectiveness of the retrofit technique with various levels of stiffness showed that as long as one of the two element types used in the retrofit (angles and backing plate) were chosen to be stiff, the retrofit was insensitive to variations in stiffness in the other element. This implies that this type of retrofit measure may be effective for many bridge configurations with minimal tailoring for the specific bridge in which it is implemented. It should be noted that additional study in this area is warranted and ongoing before implementation is recommended.

References

1. Barsom, J.M & Rolfe, S.T. (2006). Fracture and Fatigue Control in Structures: Application of Fracture Mechanics Third Edition. ASTM, West Conshohocken, PA.

2. Fisher, J. W., Jian, J., Wagner, D. C., and Yen, B. T. (1990). "Distortion-induced fatigue cracking in steel bridges." *National Cooperative Highway Research Program Report #336,* Transportation Research Board, National Research Council, Washington, D. C.

3. Zhao, Y. & Kim Roddis, W.M. (2007). "Fatigue behavior and retrofit investigation of distortion-induced web gap cracking." *Journal of Bridge Engineering*, 12(6), 737-745.

4. AISC (2005). *Steel Construction Manual*, 13th Edition, American Institute of Steel Construction, Inc., Chicago, IL.

5. Belytschko, T., Gracie, R., Ventura, G. (2009). "A review of extended/generalized finite element methods for material modelling." *Modelling and Simulation in Materials Science and Engineering*, 17(4), 1-24.

6. Bellec, J., Dolbow, J.E. (2003). "A note on enrichment functions for modelling crack nucleation." *Communications in Numerical Methods in Engineering*, 19,921-932.

7. Simulia. (2010). "Classical Fracture and Failure with ABAQUS," Web-based course notes.

PART II: FINITE ELEMENT MODELING TECHNIQUES FOR CRACK PREDICTION AND CONTROL IN STEEL BRIDGE GIRDERS

T.I. RICHARDSON[1], F. ALEMDAR[2], J.C. PRZYWARA[3], C.R. BENNETT[4], A.B. MATAMOROS[5], S.T. ROLFE[6]

Abstract

This paper focuses on methods for accurately predicting locations of cracking in steel bridge girders subjected to distortion-induced fatigue using finite element (FE) analysis techniques. Additionally, techniques discussed are appropriate for quantitatively evaluating the effectiveness of various fatigue retrofits. In this study, different FE modeling techniques are discussed, including the Hot Spot Stress (HSS) technique and use of Extended Finite Element Modeling (XFEM) algorithms for identification of crack initiation locations and crack propagation paths. The subject of this study includes a 2.7-m (9-ft) length of steel bridge girder, before and after various fatigue retrofits. The girder was modeled using ABAQUS 6.10, and modeling results were compared to laboratory tests of identical 2.7-m (9-ft) steel girders tested in distortion-induced fatigue. Retrofits studied computationally and experimentally included bolted steel angles with a backing plate and crack-arrest holes. All retrofits were studied analytically. The simulation and the experimental results were in good agreement as to locations of crack formation. The *J*-Integral, Stress Intensity Factors (SIF), and the HSS technique were used to measure the likelihood of crack growth before and after retrofits were applied.

University of Kansas, 1530 W. 15th St., Lawrence, KS 66045
[1] Temple I. Richardson, Graduate Research Assistant, University of Kansas, temple10@ku.edu
[2] Fatih Alemdar, Graduate Research Assistant, University of Kansas, alemdar@ku.edu
[3] John C. Przywara, Graduate Research Assistant, University of Kansas, j345p627@ku.edu
[4] Caroline R. Bennett, PhD, Assistant Professor, University of Kansas, crb@ku.edu
[5] Adolfo B. Matamoros, PhD, Associate Professor, University of Kansas, abm@ku.edu
[6] Stanley T. Rolfe, PhD, A.P. Learned Distinguished Professor, University of Kansas, srolfe@ku.edu

Introduction

Welded steel bridges built prior to the mid-1980s commonly experience cracking due to distortion-induced fatigue. One particularly susceptible detail where fatigue cracks often form is the web gap region, which is located at the interface between the connection plate, web, and flange. This fatigue detail was developed to avoid welding transverse stiffeners to the tension flange. The result of this practice is the creation of a slender segment of web, bounded by a flange on one boundary and a connection stiffener on the other. Secondary forces transmitted through cross-frames or diaphragm members must be transferred through this delicate web gap region, which also includes a series of geometric discontinuities due to the presence of welds. Out-of-plane movement in the web gap region over many load cycles is referred to as distortion-induced fatigue (Fisher 1984).

Repair of cracks occurring in web gap regions may be approached in a variety of manners (Fisher 1984; Zhao et al. 2007), and the effectiveness of retrofit selection has shown to be sensitive to the local and global geometry and layout of the bridge (Hassel et al. 2012; Hartman et al. 2010). Studies focused on examining retrofit techniques for details subjected to distortion-induced fatigue have generally concluded that individual bridges should be analyzed on a case-by-case basis to determine the most appropriate retrofit application. Cracking usually does not occur in an isolated location in a bridge, but will tend to occur at many similar details repeated throughout the structure. Because of this, the repair of a bridge experiencing distortion-induced fatigue is usually an expensive undertaking. Therefore, bridge owners are justified in seeking advanced analysis of a bridge that is planned for fatigue rehabilitation. Bridge owners may also seek an advanced analysis of a bridge to determine fatigue susceptibility or remaining fatigue

life; nominal stress approaches that are meaningful for planar loading are not applicable to complex fatigue details subjected to both in-plane and out-of-plane stresses.

Advanced analysis of a bridge aimed at developing an effective fatigue retrofit scheme or assessing remaining fatigue life usually relies on the use of 3D finite element analysis and physical measurements. Little advice exists in the literature to ensure that meaningful output is obtained from a finite element analysis to determine fatigue susceptibility. Capabilities of finite element analysis software have increased greatly in recent years with respect to direct simulation of fatigue crack initiation and growth (e.g. the Extended Finite Element Method (XFEM)), and little discussion of applications of this technique have been found in the steel bridge literature.

Background

The overarching goal of research described in this paper was to evaluate various retrofits for effectiveness in reducing fatigue crack propensity in steel bridges susceptible to distortion-induced fatigue. To aid in addressing this larger goal, the ability to accurately model fatigue cracks, capture realistic stress distributions, and identify appropriate measures for fatigue crack propensity in steel bridge girders was deemed a necessity.

The specific objective of this study was to evaluate various modeling techniques and quantitative measures for appropriateness as a means to assess fatigue susceptibility within a series of finite element models. The scope of this study involved quantifying fatigue susceptibility utilizing detailed three-dimensional computational simulations correlated with the behavior of experimental specimens.

Crack Prediction Using Finite Element Modeling

Four retrofits were studied to determine which decreased the likelihood of crack growth the most. Retrofits included: (1) crack-arrest holes (2) web-to-stiffener angles with a backing plate (3) stiffener-to-flange angles and (4) composite blocks. All retrofits contained a 102-mm (4-in.) long crack along web-to-stiffener weld and a 204-mm (8-in.) horizontal crack along the web-to-bottom flange weld. The third and fourth retrofits modeled a 64-mm (2.5-in.) long horizontal crack 15-mm (0.6-in.) below the web-to-stiffener weld. This crack was first placed in experimental specimen one to assure where a crack would form, and to have direct comparisons between specimens. It was found that cracks formed quickly in the experimental model, and cracks were no longer drilled in other specimens. The crack-arrest holes required the cracks to be modeled explicitly since the crack tip would terminate within the drilled hole. The web-to-stiffener angles with backing plate retrofit modeled these two cracks using XFEM techniques.

The HSS technique has often been used in the evaluation of off-shore platforms and other engineering fields, but it has not been applied to determine fatigue life of steel bridges. This method is effective at determining stress near geometric discontinuities found near welds and is more accurate than the nominal stress approach. One downside of this method is its sensitivity to mesh size (Roddis, 2010).

The *J*-Integral and SIFs are measures often used in finite element models to determine if a crack will grow (Zhu, 2010). SIFs can be accurately determined by using the boundary finite element method (BFEM). These values for different modes of crack surface displacements are then converted to the *J*-Integral. Mode I crack displacement occurs when crack surfaces open perpendicular to each other in opposite directions. Mode II crack displacement is when the two crack surfaces slide over each other perpendicular to the length of the crack. Finally, a mode III

crack displacement is the tearing mode. In this mode the crack surfaces slide over each other in a direction parallel to the length of the crack (Barsom and Rolfe, 1999).

Cook et al. (2002) explained that the finite element analysis software ABAQUS calculates the *J*-Integral as positive, but then the value is labeled positive or negative to describe crack opening behavior. Examining nodal displacements at the corners of the cracks will tell if a crack is opening or closing in a given direction. If the displacement is positive, then the crack is opening and the *J*-Integral is positive. If the *J*-Integral is negative, then the crack is closing.

Modeling Methodology

Detailed three-dimensional FE models were created using ABAQUS 6.10. The elements used for modeling the web were eight-node solid brick elements, each having 24 degrees of freedom. The mesh in the web was denser in the bottom and top web gaps where cracks were expected to form. A dense mesh increased the accuracy of the model; however, this caused the run-time to increase significantly. The mesh size in the bottom web gap was 0.6-mm (0.023-in.), and the mesh size was 9.5-mm (3/8-in.) outside of this area. Tetrahedral elements were used to transition between these two mesh sizes.

All materials were modeled as isotropic and linear elastic. The modulus of elasticity for the steel was set to 200,000 MPa (29,000 ksi) and Poisson's ratio was 0.3. The modulus of elasticity for the concrete was 27,780 MPa (4,030 ksi) and Poisson's ratio was set to 0.2. When composite material was included in retrofit simulations, it was assigned a modulus of elasticity of approximately 34,500 MPa (5,000 ksi) with a Poisson's ratio of 0.1.

In the simulations, both the concrete floor and the series of channels were modeled to mimic the physical test set-up used in the laboratory. Two channels running parallel to the girder

on both sides were used to connect the channels running perpendicular to the girder which were connected to the concrete strong floor. Both the analytical and physical specimens can be seen in Figure 1.

<div align="center">

(a)   (b)
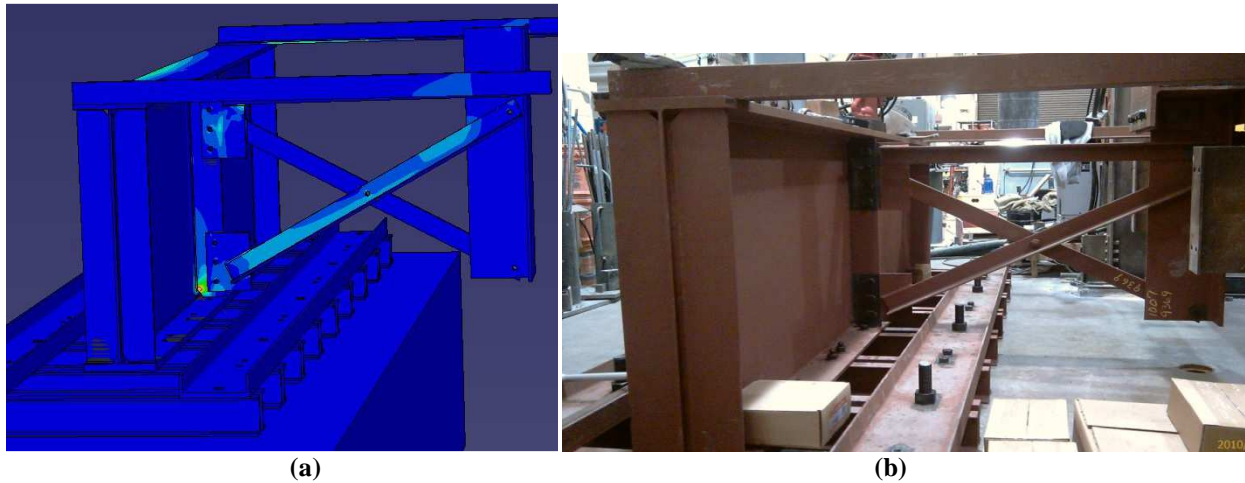
Figure 1(a.) Detailed finite element model of the 2.7-m (9-ft) girder and (b.) the physical specimen tied to the laboratory floor.

</div>

Angles were included in the model at both ends of the top flange to apply restraint to the girder and to mimic the middle section of a bridge girder. The opposite ends of the angles were bolted to a 3500-mm (138-in.) long MC 12×50 section which was attached to the loading frame. These elements were included in the simulations, and tie constraints were used to attach the angles to both the top flange and the MC channel. 4.8-mm (3/16-in.) fillet welds were used to attach the flanges to the web and cross-frame members to gusset plates that were in turn bolted to the connection plate. Tie constraints were used to connect the fillet welds to these parts. Welds were modeled as right triangles and each consisted of hexagonal 8-node brick elements with a mesh size of 2.54-mm (0.1-in.).

Initially, bolts and threaded rods were used to connect the channels to the concrete laboratory floor and the steel girder. Later, simulations used tie constraints instead of bolts to attach these parts. Similar results were found when using bolts or tie constraints, and the run-

time greatly improved when applying tie constraints. In the majority of the models examined, tie constraints were utilized for this connection.

The actuator was modeled as an 86×86-mm (3.4×3.4-in.) square with a length of 584 mm (23-in.), with the ability to move vertically. Cross-frame elements were attached to the actuator through a WT267×700-mm (WT10.5×27.5-in.) by utilizing tie constraints. The cross-frame elements were connected to the girder specimen using fully-tightened bolts. The load applied to the actuator part was specified as a 22.2 kN (5 kips) tension load.

Tensioned bolts were modeled by merging the head and nut to the shank, and threads were not modeled. The middle of the shank was partitioned so that an interior surface was present. A bolt tensioning step was created after the Initial Step, in which a bolt load was applied to the interior face of the shank. In the Load Step, the bolt length was kept constant. Greater detail in regards to bolt modeling can be found in Appendix B.

Tie constraints were used to connect various parts within the models; these constraints ensured deformations were equal between a master surface and a slave surface. Sliding and intersection of one part into another was prevented by applying tie constraints which provided full connection between nodes. Load transfer from the actuator to connecting elements was kept in mind when selecting master and slave surfaces. The first member near the actuator load was the WT, and the cross braces were framed into the WT. Therefore the WT was selected as the master surface and the cross braces as the slave. Model run-time was optimized when both the slave and master surfaces were partitioned to be the same size and also when the master surface was defined to have a coarser mesh than the slave.

When greater levels of accuracy were required, interactions were used to allow parts to slide against each other. An interaction property was created which specified a surface-to-

surface penalty hard contact and friction coefficient of 0.35 in the tangential and normal properties. Interactions were defined between the angle, web, and shims for the model containing the angle retrofit to prevent the parts from intersecting each other and to allow for friction. Another interaction was created in the top web gap to allow for bearing interaction between the connection plate and the top flange.

Crack Modeling Techniques

Three modeling methods were used to simulate cracks in the analytical specimen. The first and most simplistic method was to model cracks explicitly by removing elements. The second technique involved seams. Finally, cracks were modeled using XFEM. More information regarding crack growth propensity was obtained when modeling cracks through seams and XFEM than when modeling cracks explicitly.

Explicit Cracks

Cracks were first simulated in the finite element models by removing a thin section of elements in the web. The mesh density in the bottom web gap area contained 0.6 mm (0.023-in.) hexagonal elements so that the crack width would be equal to this small element size. The accuracy of modeling cracks in this manner was dependent upon the mesh size. When using this crack modeling technique, cracks were not able to grow or initiate. Other useful information pertaining to the crack such as the J-Integral and SIFs could not be obtained because these values can only be determined when modeling cracks through contour integrals or XFEM. In the first experimental specimen a 64-mm (2.5-in.) horizontal crack was explicitly placed 15-mm (0.6-in.) below the stiffener-to-web weld to assure where the crack would be between specimens. It was

found that with the load applied, cracks would form quickly without the need for a pre-existing crack.

Seams

The second crack modeling method inserted seams. The first step was to partition the web because crack locations, lengths, and tips were chosen based on these partitions. Next, the crack extension direction was chosen by utilizing q vectors. The starting coordinate was chosen as one end of the crack, and the end coordinate was the crack tip. If both tips of a crack were allowed to grow, then two q vectors were specified for each tip. The seam was created in the same Special section of the Interaction Property Module, which is circled in red in Figure 2.
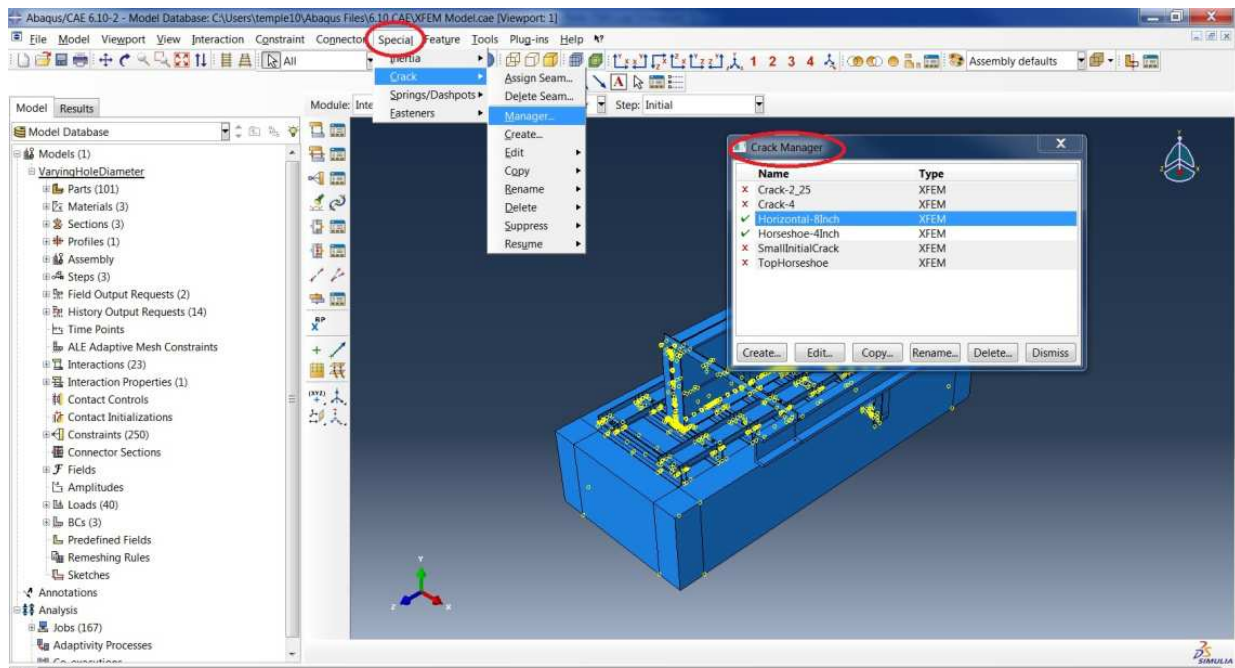
Figure 2. Special section of interaction module.

Different areas around a cracked part are shown in Figure 3. The crack tip is a set of nodes in a three-dimensional model that are at the end of a crack, while the crack front is the nodes around the crack tip. The number of contours is specified by the user. The first few

contours can yield inaccurate results because the crack tip was specified (Simulia, 2010). Five contours were specified and all data was extracted from the fifth contour. It should be noted that modeling different crack geometries in this method can be restrictive since the location of cracks is dependent on partitions.
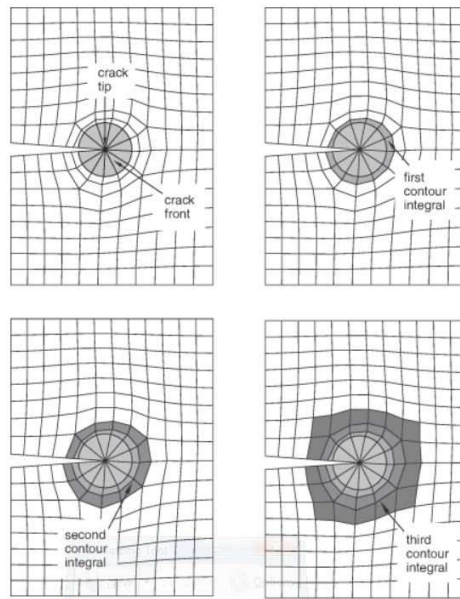
Figure 3. Successive contour integrals surrounding the crack tip (Simulia, 2010).

Extended Finite Element Method

The third method for modeling cracks utilized XFEM techniques. Cracks were modeled as three-dimensional planar shells. Because the crack had no thickness, the accuracy was slightly greater than when elements were removed. Cracks were modeled as through the thickness of the web with a width of 9.5-mm (3/8-in.). Crack lengths and locations were chosen based on cracks in the experimental specimen.

The concept of XFEM was first published in 1999 (Moes, et al. 1999). This theory was implemented within ABAQUS in recent updates to the finite element modeling program. XFEM enhances the finite element approximation by adding discontinuous functions to the solution at

nodes immediately affected by a crack. Three distinct sets of nodes are used in XFEM to approximate a cracked model (Yazid et al., 2009). These node sets are as follows:

(1) All nodes in the model domain

(2) Nodes whose shape function support is intersected by a crack

(3) Nodes whose shape function support contains the crack front.

Subsequently, there are three different approximations for the displacement, U, for the three sets of nodes in the model. The first of these approximations is applicable to all nodes in the model and is represented by the expression presented in Eqn. 1:

$$U = U_I = \sum_{i \epsilon I} u_i N_i \qquad \text{(Eqn. 1)}$$

where:

I = set of all nodes in the domain

u_i = classical degrees of freedom for node i

N_i = shape function for node i

When there is an existing crack in a region of a model where crack initiation and propagation is allowed, additional approximations are utilized in addition to U_I to obtain a more refined solution. One of these approximations represents a solution refinement to calculate the effect of the discontinuity across a fully-developed crack. Eqn. 2 represents this refinement:

$$U = U_I + U_J = U_I + \sum_{j \epsilon J} b_j N_j H(x) \qquad \text{(Eqn. 2)}$$

where:

J = set of nodes whose shape function support is cut by a crack

b_j = jump in displacement field across the crack at node j

N_j = shape function for node j

$H(x)$ = Heaviside jump function (+1 on one side of crack, -1 on other side)

The final approximation characterizes a solution refinement for the calculation of nodal displacements around both crack tips. This is represented by the expression in Eqn. 3:

$$U = U_I + U_{K1} + U_{K2}$$
$$= U_I + \sum_{k \in K1} N_k \left(\sum_{l=1}^{4} c_k^{l1} F_l^1(x) \right) + \sum_{k \in K2} N_k \left(\sum_{l=1}^{4} c_k^{l2} F_l^2(x) \right) \qquad \text{(Eqn. 3)}$$

where:

$K1$ = set of nodes whose shape function support contains one crack front

$K2$ = set of nodes whose shape function support contains the other crack front

N_k = shape function for node k

c_k^{l} = additional degrees of freedom associated with crack-tip enrichment functions

F_l = crack tip enrichment functions

Any number of crack tip enrichment functions may be used to refine the approximation at the crack tip. However, ABAQUS only uses four enrichment functions, where these functions are given in polar coordinates, as presented in Eqn. 4:

$$F_l(r,\theta) = \left\{ \sqrt{r} \cos\left(\frac{\theta}{2}\right), \sqrt{r} \sin\left(\frac{\theta}{2}\right), \sqrt{r} \sin\left(\frac{\theta}{2}\right) \sin\theta, \sqrt{r} \cos\left(\frac{\theta}{2}\right) \sin\theta \right\} \qquad \text{(Eqn. 4)}$$

For the implementation of linear elastic fracture mechanics (LEFM) using XFEM in ABAQUS, parameters for crack initiation and propagation have to be specified as material properties. For crack initiation, various damage initiation variables can be utilized, and for this simulation maximum principal stress was selected as that damage initiation variable (Simulia,

2010). This can be represented as σ_{max}. This creates a fracture criterion variable, f, which is defined as the ratio of actual maximum principal stress across an element to the allowed maximum principal stress and is thus represented as $f = \sigma_{actual} / \sigma_{max}$. A crack will initiate in an element when the fracture criterion is between the two boundaries in Eqn. 5.

$$1.0 \leq f \leq [1.0 + f_{tol}]$$ (Eqn. 5)

The variable f_{tol} is the tolerated error of the fracture criterion variable and was predefined as 0.05. If $f > [1.0 + f_{tol}]$, the time increment for the calculation is continually reduced until the fracture criterion inequality is satisfied. Once this happens, a new crack will initiate or an existing crack will extend tangent to the direction of maximum principal stress.

The next important consideration for LEFM in ABAQUS is the determination of damage evolution. In ABAQUS, damage evolution is a function of the maximum width of the crack opening, δ_{max}, and has a default linear degradation of stiffness for an element intersected by a XFEM crack. While other rules of degradation may be specified, linear degradation was deemed adequate when analyzing the effect of varying values for δ_{max} for these simulations. Figure 4 shows the relationship between crack opening and time while Figure 5 shows the relationship between stiffness and crack opening as modeled in ABAQUS.
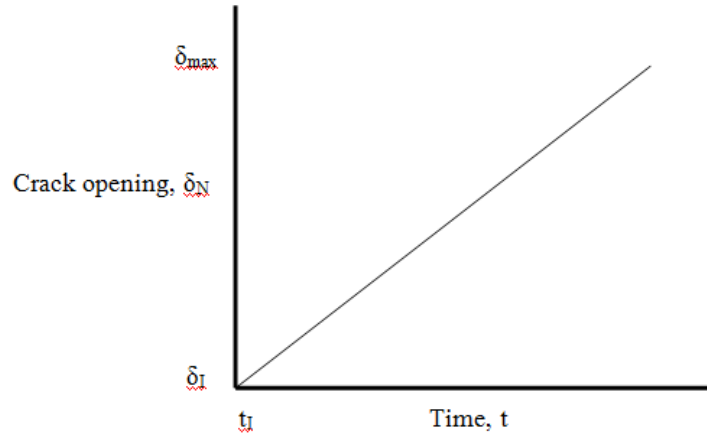
Figure 4. Linear progression of crack opening after initiation occurs (Simulia, 2010).
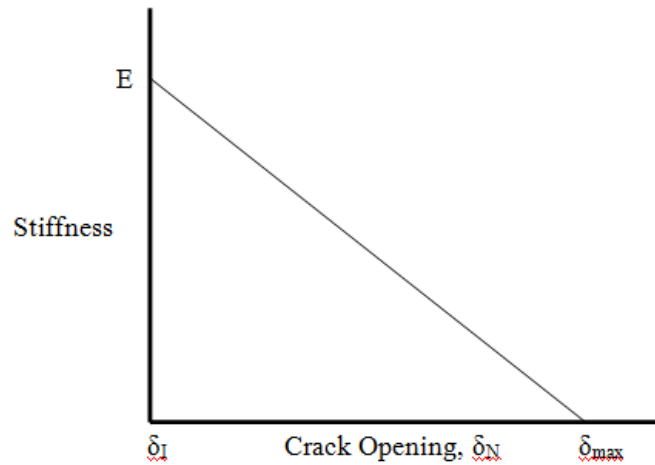
Figure 5. Linear degradation of stiffness across a crack as the crack opening widens (Simulia, 2010).

To better demonstrate how crack initiation and propagation parameters fall within the framework of the XFEM approximation, Figures 6 – 12 show how a crack initiates and propagates in a simple two-dimensional 9×5 node mesh. Figure 6 shows the mesh before any crack has occurred, while Figure 7 presents the mesh after the first elements in the model have initiated and f is between the boundaries in Eqn. 5. These elements are shaded in Figure 7. Figure 8 then shows the mesh before the second increment calculation, with the mesh now containing a crack. The crack is shown by the dotted line and has a crack width value of 0 since the crack has just initiated. The lightly shaded nodes in Figure 8 represent where ABAQUS

applies additional refinement to the approximation due to the presence of a new crack near these nodes. Figure 9 presents the result of the computation of the second increment, wherein two new elements have now met the inequality in Eqn. 5. This leads to Figure 10, which presents the scenario considered for calculation at the start of the third increment. The original crack has now widened and is represented by the solid line cutting across the elements. Crack growth is based off of the relationship between stiffness and time, as shown in Figures 4 and 5. The blackened nodes in Figure 10 represent where ABAQUS will apply solution refinements to represent the discontinuity created by the crack. Just as in Figure 8, the dotted lines in Figure 10 represent the part of the crack that has just initiated and has a zero width, and the lightly shaded nodes represent where a solution refinement due to the crack tip will be applied. This process repeats in ABAQUS until the full solution is computed or until the approximation cannot reach a convergence for a particular time step. Figure 12 shows the resulting crack propagation after three completed increments for this example.
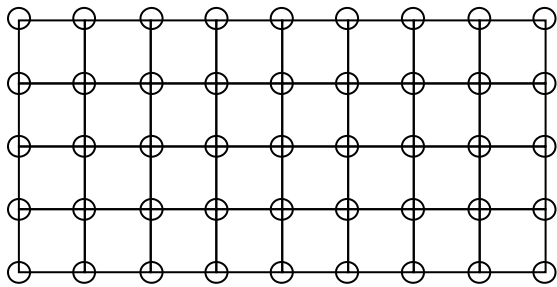
Figure 6. A 9 x 5 node two-dimensional mesh before increment 1.
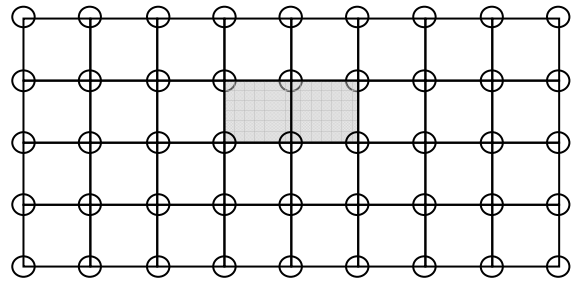
Figure 7. Two-dimensional mesh after calculation of increment 1.
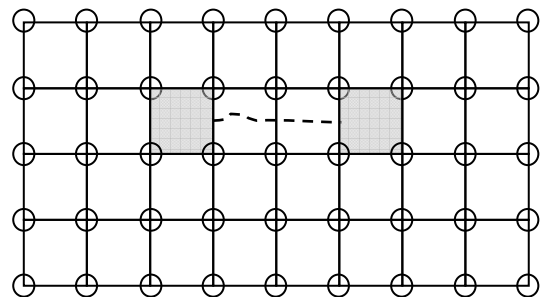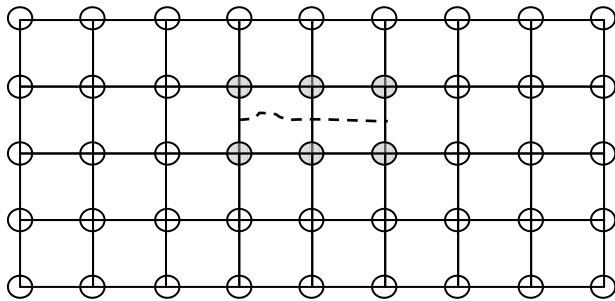
Figure 8. Two-dimensional mesh before calculation of increment 2.
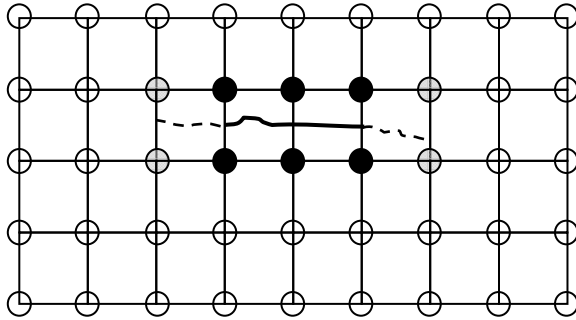
Figure 9. Two-dimensional mesh after calculation of increment 2.
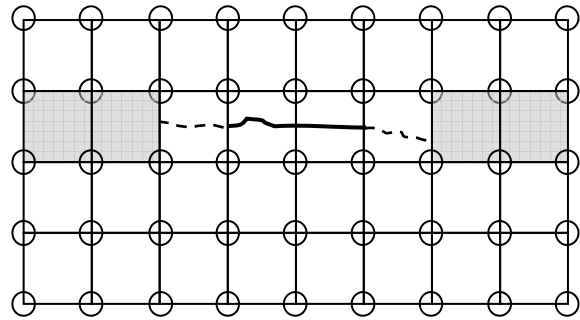
Figure 10. Two-dimensional mesh before calculation of increment 3.
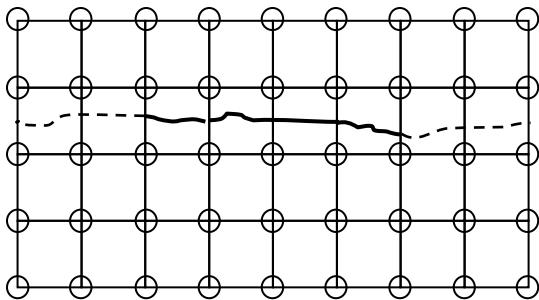
Figure 11. Two-dimensional mesh after calculation of increment 3.

Figure 12. Crack propagation in a two-dimensional. mesh after 3 increments.

Comparison between the Cohesive Method and LEFM

There are two techniques for capturing crack propagation when using XFEM: (1) traction-separation cohesive behavior and (2) LEFM. If a crack is not initially present, crack initiation can only be captured by using the traction-separation cohesive method. Once initiation has occurred, LEFM can be used to model propagation. The two methods cannot both be used to model identical crack behavior.   For example, properties for the cohesive method and LEFM cannot both be specified to model crack propagation. The cohesive method is an energy and strength criterion, while LEFM is not (Chen et al., 2010).

Modeling of Retrofits

Various retrofits were modeled to evaluate their fatigue mitigation potential, measured by examining the *J*-Integral, SIFs, and change in stress from unretrofitted scenarios to retrofitted scenarios. Mitigation techniques studied included: (1) crack-arrest holes, (2) bolted angles connected to the web and flange, (3) angles bolted to the connection plate and flange with a backing plate, and (4) composite blocks.

Results and Discussion

Finite element models with retrofits and without retrofits were examined, and results were quantified using the following measures: Hot Spot Stress Technique, *J*-Integral, and SIF. Not all retrofits could be quantified using the *J*-Integral and SIF values due to varying crack modeling techniques, but HSS values were obtained for all retrofits. Analytical results were then compared to physical test results.

Measuring Fatigue Damage Potential

The peak stress throughout the model changed with different crack and retrofit configurations. When there were no cracks or retrofits, the maximum stress overall was in the stiffener-to-web weld in the bottom web gap. Stress fields in the web-to-stiffener weld in the bottom web gap exceeded the yielding point.

After looking at different stress types, including directional, maximum principal, Von Mises, and Tresca to compare the simulation to the experimental specimen, it was found that maximum principal stresses provided the best correlation. As shown in Figure 13, the crack

growth in the experimental specimen closely followed the direction of highest maximum principal stress in the FE model.
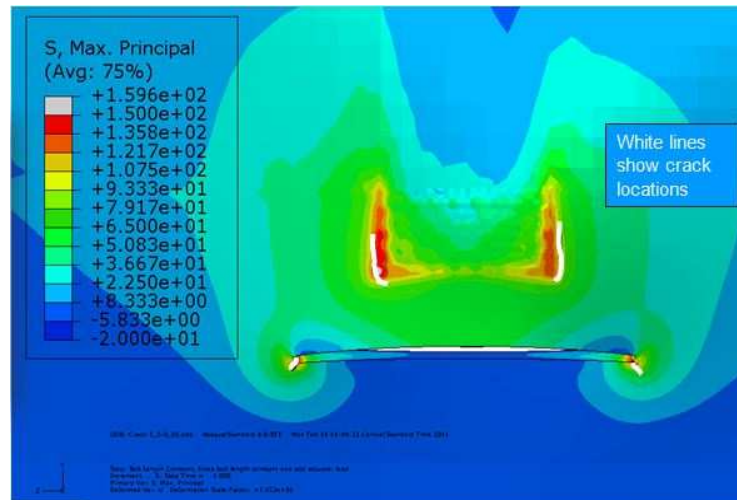
Figure 13. Good agreement between the experimental crack locations shown in white and areas of high maximum principal stress in the analytical model.

The HSS technique was applied to quantify stresses in the web near welds. A path was taken a distance away from the welds that is equal to half the thickness of the web, or 5-mm (0.2-in.) HSS 1 was a horseshoe-shaped path taken around the stiffener-to-web crack in the bottom web gap. The length of this path followed the length of the crack, which was modeled as 102-mm (4-in.) long. HSS 2 was a horizontal path in the bottom web gap that was along the web-to-flange weld. The length of this path followed the length of the horizontal crack, which was modeled as 203-mm (8-in.) long. Similar HSS paths were pulled from the fascia side of the web in the top web gap of the test specimen. In models that were uncracked, the path shapes and lengths were kept the same to provide a direct comparison between models.

In addition to the HSS technique, crack growth propensity was determined by looking at *J*-Integrals and SIFs. To study the *J*-Integral and SIFs in greater detail, a smaller model was created. The model consisted of a 1270×1270-mm (50×50-in.) plate with a crack half the

length of the plate, as seen in Figure 14. This model was studied in two and three dimensions. First, a 6.9-MPa (1-ksi) compressive force was applied to the left and right sides of the plate to force the crack to close. Next, a tensile force replaced the compressive force to simulate opening of the crack. In the model, a surface-to-surface interaction was placed between both sides of the crack to prevent them from intersecting each other. From this smaller model, it was found that when loading caused a crack to close, SIFs become negative, and when the crack opened, SIFs remained the same magnitude but opposite in sign. The loading applied was used to force a Mode I crack opening.
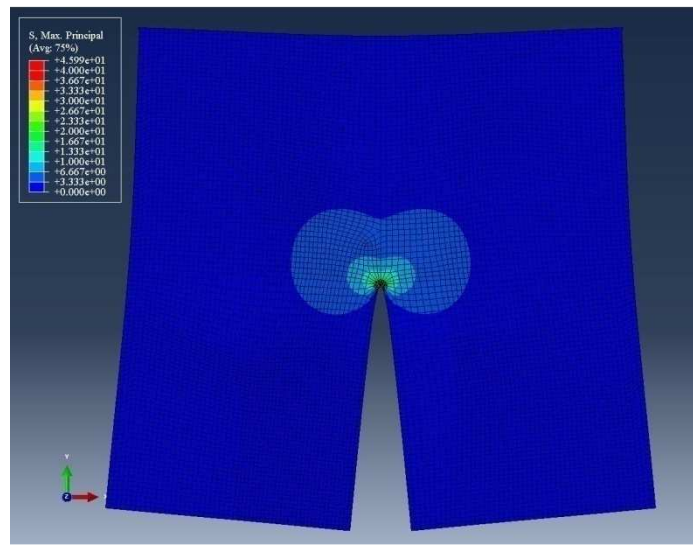
Figure 14. Focused mesh surrounding crack tip.

The analytical results of this model were compared to equations for a single-edge notch in a finite plate. The following equation was used to determine K_I (Barsom and Rolfe, 1999).

$$K_I = 1.12\sigma\sqrt{\pi a}\left(\frac{a}{b}\right) \qquad \text{(Eqn. 6)}$$

The correction factor, (a/b), was applied to take into account bending stresses due to the plate being asymmetric, and was equal to 2.55 since the crack was equal to half the length of the plate.

With this equation, K_I was calculated as $25\,\text{ksi}\sqrt{\text{in.}}$, and the calculated K_I value from ABAQUS was $26\ \text{ksi}\sqrt{\text{in.}}$. These values showed great agreement between the equation and the analytical model. K_{II} values in the two-dimensional model were approximately 0, which is expected in a pure Mode I crack opening.

Parts that contained cracks had circles partitioned at the tips of cracks to create contours. The *J*-Integral and SIFs were specified as separate History Outputs generated at the end of the Loading Step. In the History Output, the number of contour integrals was specified as five. The accuracy of the *J*-Integral and SIFs increase as the contours move away from the crack tip. Therefore, data was read only from the fifth contour.

Retrofit Measures

Crack-arrest holes 19-mm (¾-in.) in diameter were drilled at the tips of the 102-mm (4-in.) horseshoe-shaped and 204-mm (8-in.) horizontal cracks in both the analytical and experimental specimens. Cracks were modeled explicitly because the crack tip was within the diameter of the crack-arrest hole if modeled using XFEM. By modeling these cracks explicitly, *J*-Integral and SIF values could not be obtained. In the simulation there were still large areas of high stress in the bottom web gap after the retrofit, which can be seen in Figure 15. When comparing a cracked, unretrofitted model to a cracked model retrofitted with crack-arrest holes, it was found that HSS 1 decreased by 38%. The stress decrease seems to indicate that the crack-arrest holes might have some positive effect, but the stress magnitudes were still well above the yield stress of the material. While HSS 1 decreased slightly, HSS 2 was found to increase by 56%. The maximum principal stress range in Figure 15(b) was 0 – 276 MPa (0 – 40 ksi). In the experimental specimen, the web-to-stiffener weld crack reinitiated on the other side of the crack-

arrest hole and grew 70-mm (2 ¾-in.) after 39,700 cycles. The results between the analytical and experimental models closely matched when comparing the high stresses in the analytical model to the rate of reinitiation of the web-to-stiffener weld crack in the experimental specimen. The two bolts holes circled in Figure 15(a) were drilled for the stiffener-to-web angles with backing plate.
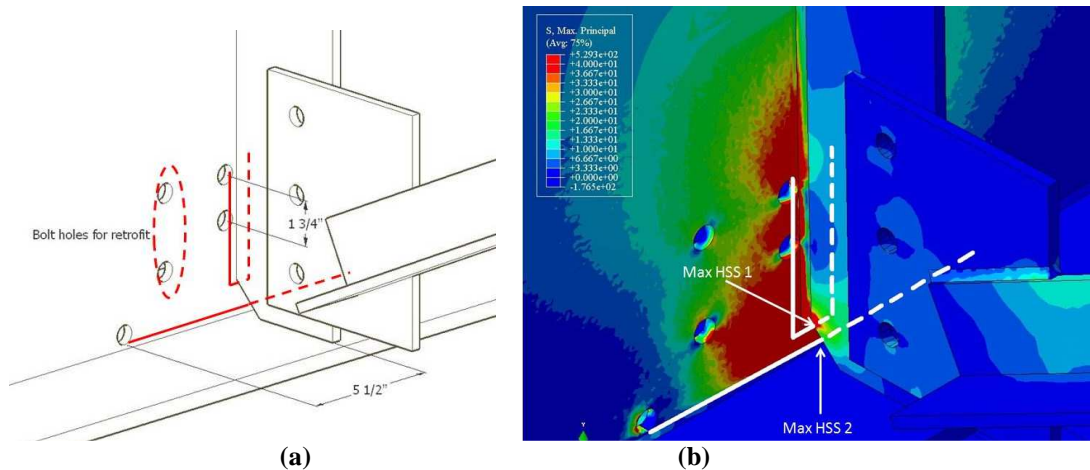
Figure 15. (a) Setup of crack-arrest holes in bottom web gap (b) Stress distribution in web gap region after crack-arrest holes have been drilled.

The next retrofit studied was the stiffener-to-web angles with a backing plate. A 102-mm (4-in.) web-to-stiffener weld crack and 204-mm (8-in.) web-to-flange weld crack were modeled using XFEM techniques. Two 152×152×19-mm (6×6×¾-in.) angles were bolted to the web and on both sides of the connection plate. On the fascia side of the girder, a 457×203×19-mm (18×8×¾-in.) backing plate was bolted to the web directly above the web-to-flange weld. An elevation view with stress paths and dimensions of the retrofit is shown in Figure 16.
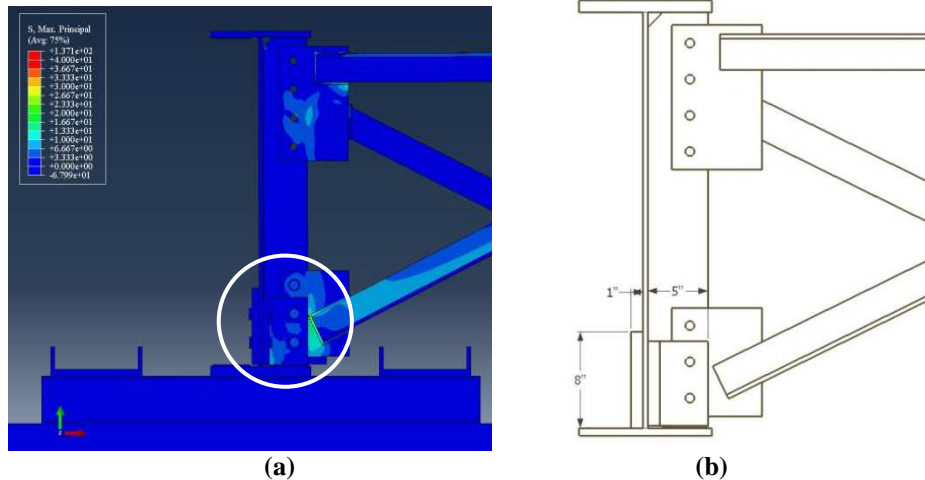
Figure 16. (a) Retrofit location applied in the bottom web gap of the experimental specimen (b) Elevation drawing of retrofit.

The dimensions of the angles and backing plate were varied to determine the optimal size. *J*-Integral, SIFs, and HSS values for varying angle and back plate thicknesses are shown in Table 1, Table 2, and Table 3. A disparity was found when comparing *J*-Integral and SIFs to HSS values. In Table 1, *J*-Integral values increased as the thickness of the angles and backing plate were increased to 25-mm (1-in.). This trend is opposite of what was found when looking at HSS values. When looking at HSS values in Table 3, the greatest stress reduction occurred when both the angles and backing plate were 25-mm (1-in.) thick. There was not a clear pattern when examining SIFs, which are shown in Table 2. For some crack opening modes, SIF values increased as the thickness of the retrofit parts increased, and in other crack opening modes SIF values decreased as the thickness increased. Distortion of the web gap region is a mixture of all three crack-opening modes and therefore the use of SIFs to determine fatigue damage is not recommended.

Table 1. Comparison of *J*-Integrals for web-to-stiffener angles and a backing plate retrofit with a 102-mm (4-in.) web-to-stiffener weld crack and a 204-mm (8-in.) web-to-flange weld crack.

Angles and Back Plate Thickness	*J*-Integral for stiffener-to-web weld crack	*J*-Integral for web-to-flange weld crack
mm (in.)	*N/mm (K/in.)*	*N/mm (K/in.)*
No Retrofit	(0.41)	(0.58)
6	1.7 E^{-5}	3.4 E^{-5}
(1/4)	(1.2 E^{-5})	(2.4 E^{-5})
13	1.8 E^{-4}	7.1 E^{-4}
(1/2)	(1.3 E^{-4})	(5.1 E^{-4})
25	2.0 E^{-2}	3.1 E^{-3}
(1)	(1.4 E^{-2})	(2.2 E^{-3})

Table 2. Comparison of stress intensity factors for three crack surface displacements with the web-to-stiffener angles and a backing plate retrofit. The thickness of the angles and backing plate were varied and compared to a model with no retrofit. All simulations contain a 102-mm (4-in.) web-to-stiffener weld crack and a 204-mm (8-in.) web-to-flange weld crack. SIF units are *MPa/√m (ksi√in.).*

Angles and Back Plate Thickness *mm (in.)*	K_I for stiffener-to-web weld crack	K_I for flange-to-web weld crack	K_{II} for stiffener-to-web weld crack	K_{II} for flange-to-web weld crack	K_{III} for stiffener-to-web weld crack	K_{III} for flange-to-web weld crack
No Retrofit	-6500 (-150)	-4000 (-92)	1700 (40)	480 (11)	- 1100 (-25)	-1300 (-30)
6 (1/4)	-51 (-1.2)	-72 (-1.66)	-74 (-1.7)	-8.6 (-0.20)	-113 (-2.6)	-22 (-0.5)
13 (1/2)	-18 (-0.41)	-307 (-7)	-210 (-4.8)	-8.2 (-0.19)	-380 (-8.9)	-184 (-4.3)
25 (1)	7.8 (0.18)	-540 (-12)	-120 (-2.8)	-14 (-0.33)	-152 (-3.5)	-350 (-8.2)

Table 3. Comparison of HSS 1 and HSS 2 values for the web-to-stiffener angles with a backing plate retrofit. The thickness of the angles and backing plate were varied, and all simulations contained a 102-mm (4-in.) web-to-stiffener weld crack and a 204-mm (8-in.) web-to-flange weld crack.

Angles and Back Plate Thickness *mm (in.)*	HSS 1 *MPa (ksi)*	HSS 2 *MPa (ksi)*
6 (1/4)	120 (17)	110 (16)
13 (1/2)	76 (11)	64 (9.3)
25 (1)	38 (5.5)	61 (8.8)

J-Integral and HSS values obtained from the web-to-flange weld crack showed similar behavior as crack lengths increased. In Figures 17 and 18, the back plate was kept at a constant thickness of 25-mm (1-in.), and the angle thickness was varied from 25-mm (1-in.) to 13-mm (½-in.) to 6-mm (¼-in.). The largest value for both of these fatigue damage parameters occurred when the crack was 25-mm (1-in.) long. *J*-Integral and HSS 2 values decreased as the web-to-flange weld crack grew to 204-mm (8-in.), as seen in Figures 17 and 18. This implies that the web-to-flange weld crack may self-arrest once the crack extends beyond 25-mm (1-in.). The lowest *J*-Integral and HSS 2 values were found when 6-mm (¼-in.) thick angles were used.
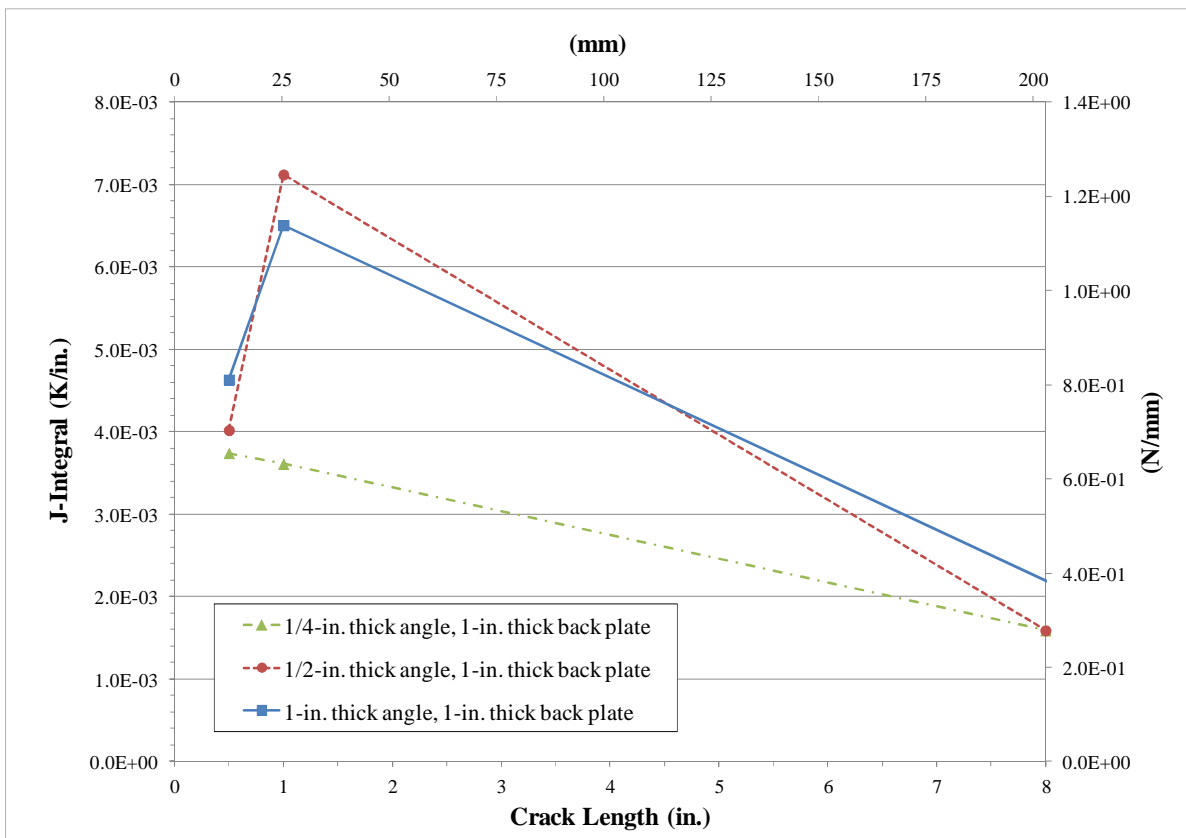
Figure 17. *J*-Integral values for the web-to-flange crack lengths and angle thicknesses.
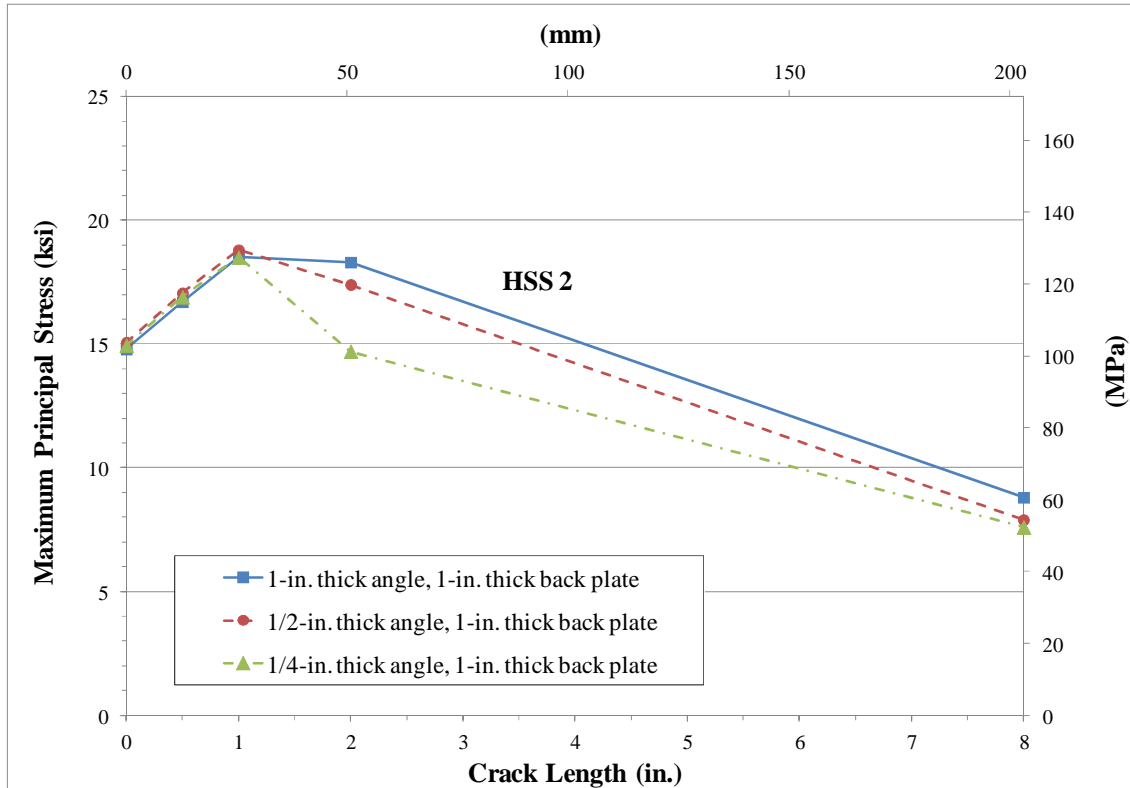
Figure 18. HSS 2 values for varying web-to-flange crack lengths and angle thicknesses.

In a corresponding experimental specimen (referred to as Specimen 2 in Alemdar (2011)), fatigue cracks began to grow in the top web gap after 1.2 million cycles. In another experimental specimen (referred to as Specimen 3 in Alemdar (2011)), this retrofit was applied when crack lengths were short, approximately 25-mm (1-in.) long, unlike Specimen 2. Whenever the stiffener-to-web angles with backing plate retrofit was applied in the bottom web gap, the web-to-stiffener and flange-to-stiffener weld cracks did not propagate. As soon as the retrofit was removed, cracks began to grow again. This result leads to the conclusion that the stiffener-to-web angles and backing plate retrofit can work on cracks that are short and long.

The next retrofit studied is one that has commonly been used to mitigate distortion-induced fatigue damage. Angles were modeled as bolted to the connection plate and bottom

flange; this retrofit was examined solely in an analytical sense. Two crack configurations were modeled. The first included a 64-mm (2.5-in.) web-to-stiffener weld crack that was explicitly modeled 15-mm (0.6-in.) below the web-to-stiffener weld. The second crack configuration modeled a 102-mm (4-in.) web-to-stiffener weld crack and a 204-mm (8-in.) web-to-flange weld crack using XFEM techniques. This retrofit proved to be very effective in the simulations, but is known to be expensive and disruptive to construct in the top web gap of a bridge, as conflicts with a concrete deck must be dealt with before a bolted connection to the top flange can be made. When comparing an unretrofitted specimen with a 64-mm (2.5-in.) crack along the web-to-stiffener weld to a cracked model with this retrofit, it was found that HSS 1 decreased by 95%. When cracks were modeled using XFEM techniques, HSS 1 decreased by 99% and HSS 2 decreased by 92%. *J*-Integral values were also compared for this retrofit, and this data can be found in Table 4. The *J*-Integral reduced to nearly zero after this retrofit was applied when compared to an unretrofitted model with the same crack configuration.

Table 4. *J*-Integral comparison before a retrofit was applied and after the flange-to-stiffener angles retrofit was attached. All simulations contain a 102-mm (4-in.) web-to-stiffener weld crack and a 204-mm (8-in.) flange-to-stiffener weld crack, and each crack was modeled using XFEM techniques.

Retrofit	*J*-Integral for 102-mm (4-in.) web-to-stiffener weld crack	*J*-Integral for 204-mm (8-in.) flange-to-stiffener weld crack
No Retrofit	0.41	0.58
Flange-to-Stiffener Angles	$1.1\ E^{-3}$	$4.8\ E^{-3}$

The final retrofit modeled was a set of 114×114×127-mm (4.5×4.5×5-in.) composite blocks in the bottom web gap, attached to both sides of the connection plate, as shown in Figure 19. Tie constraints were used to attach the composite block to the bottom flange, web, gusset

plate, and connection plate in order to simulate bond between the composite and steel materials. Two crack configurations were modeled. The first was an explicitly modeled, 64-mm (2.5-in.) long crack, 15-mm (0.6-in.) below the web-to-stiffener weld. The second configuration included a 102-mm (4-in.) web-to-stiffener weld crack and a 204-mm (8-in.) flange-to-stiffener weld crack, and these cracks were modeled using XFEM. For the 64-mm (2.5-in.) long crack, it was found that HSS 1 decreased by 93% when compared to an unretrofitted model with the crack explicitly modeled. Once this area was stiffened, stresses of high magnitude occurred at the weld connecting the bottom cross brace to the gusset plate. A larger composite block that covers this weld could stop the stress from moving to this region. When the cracks were modeled using XFEM, two paths were taken. HSS 1 was around the web-to-stiffener weld crack and HSS 2 was around the flange-to-stiffener weld crack. After the composite block was applied, HSS 1 decreased by 99% and HSS 2 decreased by 96%. Table 5 lists comparisons of *J*-Integral values before and after the composite blocks were attached. Similar to the flange-to-stiffener angles retrofit, the *J*-Integral values after the composite blocks were attached were nearly zero.

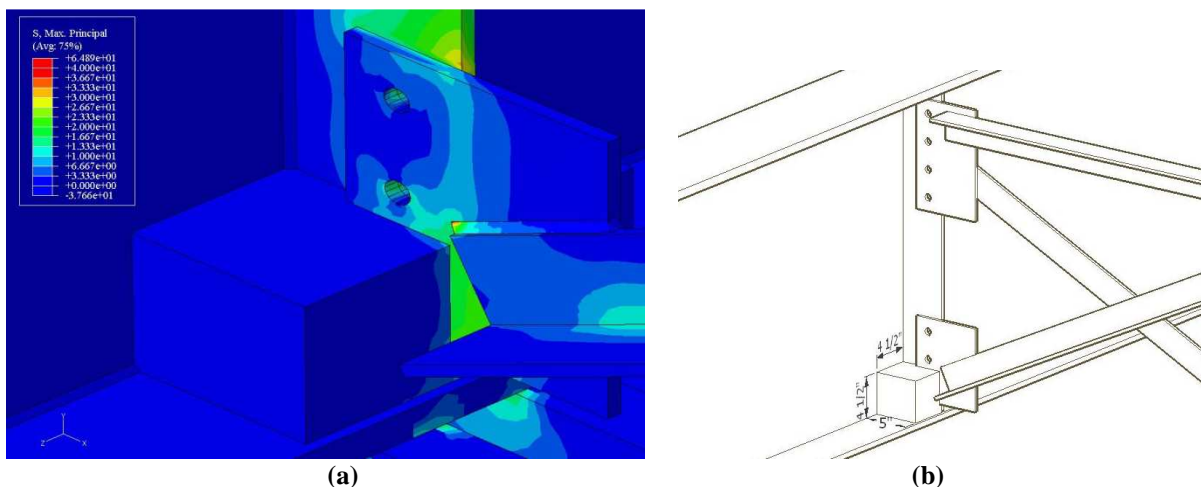**(a)**   **(b)**

Figure 19. (a) Stress distribution with composite block (b) Schematic of 127×114×114-mm (5×4.5×4.5-in.) composite block on both sides of the connection plate.

Table 5. *J*-Integral comparison before a retrofit was applied and after composite blocks were attached to both sides of the stiffener. All simulations contain a 102-mm (4-in.) web-to-stiffener weld crack and a 204-mm (8-in.) flange-to-stiffener weld crack, and each crack was modeled using XFEM techniques.

Retrofit	*J*-Integral for 102-mm (4-in.) web-to-stiffener weld crack	*J*-Integral for 204-mm (8-in.) flange-to-stiffener weld crack
No Retrofit	0.41	0.58
Composite Block	$1.6\,E^{-3}$	$1.2\,E^{-4}$

Conclusions

Advances in FE modeling have allowed cracks to be modeled in ABAQUS. Retrofit effectiveness should be determined by comparing multiple crack growth propensity measures. Several crack modeling techniques have been presented with pros and cons of each method. The following conclusions can be made from the research presented:

1. Of the three crack modeling techniques discussed, removing elements (explicit crack modeling), contour integrals, and XFEM, modeling cracks using XFEM was found to be the most simplistic and effective technique because the cracked domains did not need to be remeshed, and also because cracks were not dependent on partitions.

2. Three retrofits were found to significantly reduce stress in the web gap, and they are the following: web-to-stiffener angles with backing plate, angles bolted to the connection plate and flange, and composite blocks. The web-to-stiffener angles with backing plate retrofit is easier to install in the field than the commonly used stiffener-to-flange angles retrofit because the concrete deck does not need to be removed. Drilling of crack-arrest holes was found to not stop cracks from reinitiating.

3. The use of SIF values calculated from ABAQUS is not recommended when the crack opening mode is a combination of all three crack tip displacement modes. This

fatigue damage measure is ideally suited when the crack tip displacement is purely in one mode, rather than in a combination of modes.

4. HSS and *J*-Integral values were compared when using the following retrofits: angles connected to the web and stiffener along with a backing plate, flange-to-stiffener angles, and composite blocks. When the angles and backing plate retrofit was applied, *J*-Integral and HSS 2 values were both the highest when the flange-to-stiffener weld crack was 25-mm (1-in.) long and then decreased as the crack lengthened to 203-mm (8-in.). HSS values reduced the most when the angles and back plate were 25-mm (1-in.) thick.

When modeling cracks using XFEM techniques, the cracked domain does not need to be altered and the crack geometry can closely match cracks found experimentally. The time to generate cracks can be decreased greatly when compared to explicitly modeling cracks. The best method to determine fatigue damage in the specimen studied is the Hot Spot Stress Technique. This method can be used for any crack modeling technique, and the results closely match with the experimental models.

References

1. Alemdar, F. (2011). "Repair of **"**Repair of bridge steel girders damaged by distortion-induced fatigue," thesis, presented to University of Kansas, at Lawrence, KS, in partial fulfillment of the requirements for the degree of Doctor of Philosophy in Civil Engineering.

2. Barsom, J.M., and Rolfe, S.T. (1999). "Fatigue and fracture behavior of welded components." Fracture and Fatigue Control in Structures, 3rd ed., (10), American Society for Testing and Materials, West Conshohocken, PA, 30-32.

3. Chen, C.R. and Y.W. Mai. (2010). "Comparison of cohesive zone model and linear elastic fracture mechanics for a mode I crack near a compliant/stiff interface." *Engineering Fracture Mechanics* 77, 3408-3417.

4. Connor, R.J. and Fisher, J.W. (2006). "Identifying effective and ineffective retrofits for fatigue cracking in steel bridges using field instrumentation." *Journal of Bridge Engineering*, 11(6), 745-752.

5. Cook, G., Timbrell, C.M., and Wiehahn, M. (2002). "Using ABAQUS to analyse fatigue crack growth under the combined influence of residual stress and cyclic external load." *ABAQUS UK Users Group Conference.*

6. Fisher, J.W. (1984). "Fatigue and fracture in steel bridges – case studies" *John Wiley & Sons, Inc.,* p. 315.

7. Moes, N., Dolbow, J., and Belytschko, T. (1999). "A finite element method for crack growth without remeshing." *International Journal for Numerical Methods in Engineering*, 46, 131-150.

8. Roddis, K.W.M., "Fatigue analysis of steel bridge details: hot spot stress approach." *Presentation at John Hopkins University*, (2010).

9. Simulia. (2010). "Classical Fracture and Failure with ABAQUS," Web-based course notes.

10. Yazid, A., Abdelkader, N. and Abdelmadjid, H. (2009). "A state-of-the-art review of the X-FEM for computational fracture mechanics." *Applied Mathematical Modelling*, 33, 4269-4282.

11. Zhao, Y. and Roddis, W.M.K. (2007). "Fatigue behavior and retrofit investigation of distortion-induced web gap cracking." *Journal of Bridge Engineering*, 12(6), 737-745.

12. Zhu, C.L., Li, J.B., Lin, G., and Zhong, H. (2010). "Study on the relationship between stress intensity factor and J integral for mixed mode crack with arbitrary inclination based on SFEM." *Materials Science and Engineering*, 10.

PART III: REPAIR OF DISTORTION-INDUCED FATIGUE CRACKS ON I35-87-43/44 BRIDGES OVER CHISHOLM CREEK

T.I. RICHARDSON[1], A.B. MATAMOROS[2], C.R. BENNETT[3], S.T. ROLFE[4]

Abstract

Two highway bridges near Park City, Kansas have widespread distortion-induced fatigue cracks in the built-up steel plate girders. Detailed finite element models of the bridge were developed to test the effectiveness of various retrofits when applied to a cracked interior girder. All retrofits considered involved the application of various bolted angles to stiffen the flexible web gap region. A new retrofit technique using angles to connect the stiffener to the web with a backing plate that was previously tested at the University of Kansas on a 2.7-m (9-ft) steel girder in the laboratory was investigated in the full bridge model. Plate thicknesses and lengths were varied to determine optimal retrofit dimensions. A traditional retrofit using angles bolted to the connection plate and flange was also investigated. Retrofit recommendations were made based on reduction of stress in the web gap and the retrofit requiring the least amount of labor and material.

University of Kansas, 1530 W. 15th St., Lawrence, KS 66045
[1] Temple I. Richardson, Graduate Research Assistant, University of Kansas, temple10@ku.edu
[2] Adolfo B. Matamoros, PhD, Associate Professor, University of Kansas, abm@ku.edu
[3] Caroline R. Bennett, PhD, Assistant Professor, University of Kansas, crb@ku.edu
[4] Stanley T. Rolfe, PhD, A.P. Learned Distinguished Professor, University of Kansas, srolfe@ku.edu

Introduction

Distortion-induced fatigue is an ongoing problem experienced by many steel bridges designed before the 1983 American Association of State Highway and Transportation Officials (AASHTO) Bridge Design Specification (1). Fatigue cracking often occurs at a detail referred to as a "web gap;" a region that comprises the interface between the web, flange, and transverse connection plate. Before changes were implemented in the 1983 AASHTO Bridge Design Specifications (2), no connection was required to be provided between connection stiffeners and adjacent flanges. This detailing practice resulted in a short length of web near the top and/or bottom flange and served as a load path to carry forces transmitted by cross-frames or diaphragms.

Fatigue cracks primarily occur in the web gap region near the tension flange, and live load is the driving force that causes these cracks to propagate. Distortion-induced fatigue is known to occur in many types of steel bridges, including floor beam, suspension, and tied arch bridges (3). Distortion-induced fatigue cracks can occur in the bottom or top web gaps, and this is dependent on the bridge geometry. The majority of literary articles have found the top web gap to be the location where most cracks initiate. The top flange is highly restrained by the presence of a concrete deck in a composite bridge, while a bottom flange has more freedom to deform laterally and rotationally. Therefore, significant distortions can be concentrated into the top web gap region. However, the locations of cracks are also heavily driven by bridge geometry and layout. For example, it has been shown (4; 5) that cracking may be more prevalent in bottom web gaps in skewed bridges with staggered cross-frame layouts.

Cracking arising from distortion-induced fatigue can be repaired using a variety of existing techniques. One of the most popular methods involves bolting angles to the connection stiffener and the adjacent flange to provide a stiff load path between those two elements. This repair is often problematic when implemented in top web gaps, however, as making the connection between the top flange and connection stiffener is frustrated by the presence of a concrete deck. This can be overcome by removing portions of the deck or tapping the inside face of the flange, but these approaches are expensive, laborious, and often require partial or full bridge closures.

A new retrofit technique has recently been developed and tested (6; 7; 8), wherein bolted angles are used to connect the web and connection stiffener with a backing plate on the fascia side of the web. This particular repair geometry is intended for exterior girders or interior girders in skewed-staggered bridge layouts; variations of this retrofit could also be used for interior girders in straight bridge systems. The repair has shown excellent performance in physical testing for halting propagation of cracks of multiple lengths. Finite element analyses have corroborated the physical test results by showing stress reductions in the web gap region on the order of 90 - 95% when compared to stresses in a cracked girder without any retrofit (8). The primary advantage to implementing this type of repair is that a connection with an adjacent flange is avoided, eliminating expenses and inconveniences associated with a concrete deck attached to a top flange.

The investigators have undertaken a study with the Kansas Department of Transportation (KDOT) to determine whether the stiffener-to-web bolted angles with backing plate retrofit is an appropriate retrofit for Kansas Bridge 135-87-43/44, a twin bridge structure carrying I-135 traffic over Chisholm Creek near Park City in Sedgwick County, Kansas. Each composite,

welded steel plate girder bridge carries two lanes of I-135 traffic, as seen in Figure 1, with Bridge 43 carrying southbound traffic and Bridge 44 carrying northbound traffic. The average daily traffic is 14,400 with 16% trucks. In the twin bridges studied, cracks are present in the bottom and top web gap regions in the positive moment regions, with the majority of cracks in the bottom web gap.

The twin bridges were designed in 1964 and constructed in 1970. The two end spans are 23-m (76-ft) long and the middle span is 29-m (95-ft). The bridges are skewed at an angle of 21°. Cross-frames at supports are back-to-back and parallel to the skew, and elsewhere are staggered and perpendicular to the girder line. Bearings consist of rockers at the abutments and bolsters at two interior supports.

The composite reinforced concrete deck has a uniform 191-mm (7.5-in.) thickness and was resurfaced in 2004. The width of the roadway is 12-m (40-ft) wide. The girder web is 1220×8-mm (48×5/16-in.), and the top and bottom flanges are 305×29-mm (12×1.125-in.) at the end and middle spans. The flanges taper to a width of 457-mm (18-in.) near the two center supports. Girders are spaced at 2.7-m (9-ft), and are labeled A through E, with A being the left girder when looking northbound. A simple schematic of an interior section of the bridge is presented in Figure 2. Additional details can be found in the original plans located in Appendix A.

The newly-developed angles with backing plate retrofit were examined in a detailed three-dimensional finite element model of Kansas Bridge 135-87-43/44. The well-established retrofit consisting of angles connecting the flange and transverse stiffener was also studied as a basis for comparison. Variations of these retrofits were studied, including replacing the back plate with a back angle, and changing the length and thickness of the angles.
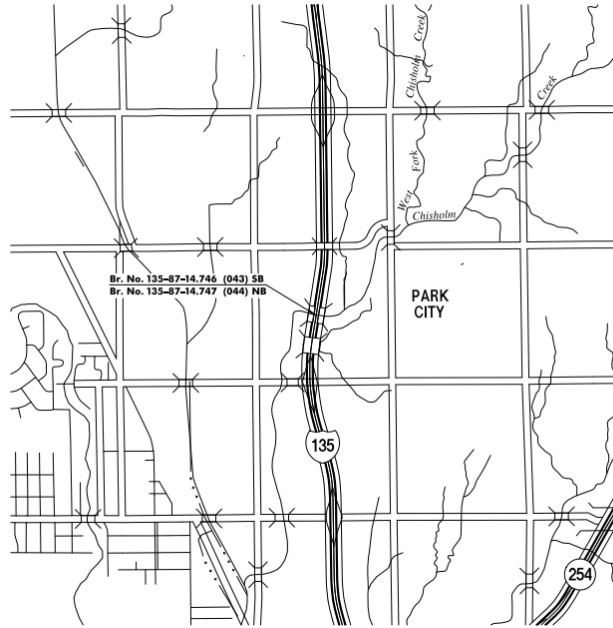
(a)
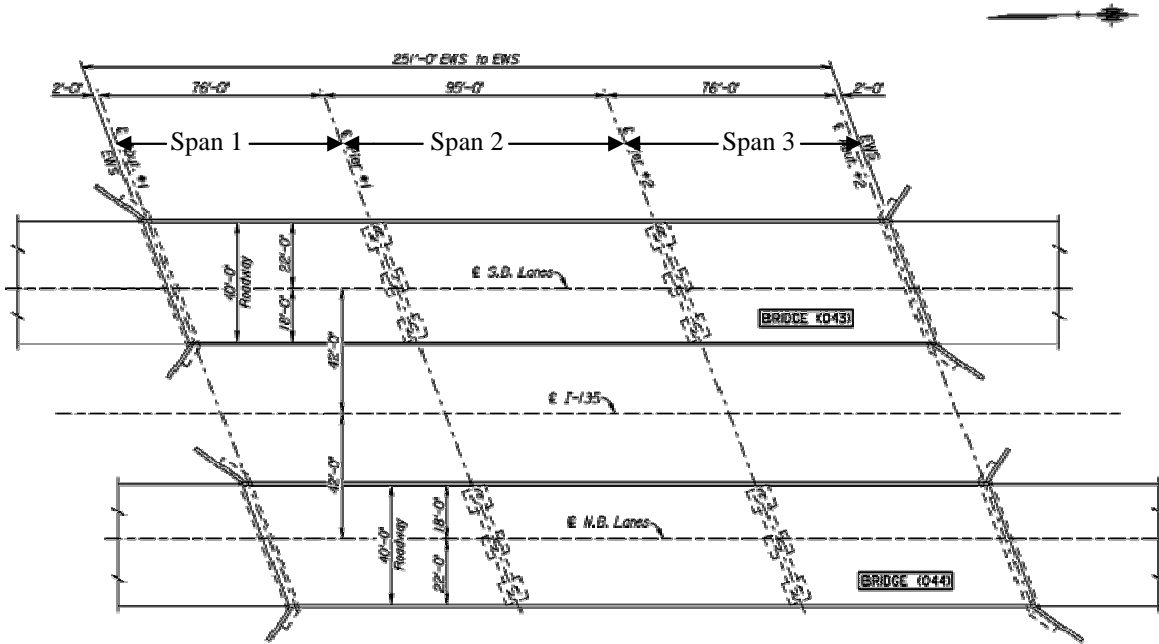
PLAN
(Twin) 76'-95'-76' Cont. Steel Girder Spans
Pedestal Type Piers, File Bent Abutments,
40'-0' Roadway, 21°-00' Skew Lt.

(b)

Figure 1. (a) Twin bridges near Park City, Kansas carrying I-135 north and southbound traffic. (b) Plan view showing roadway width and span length.
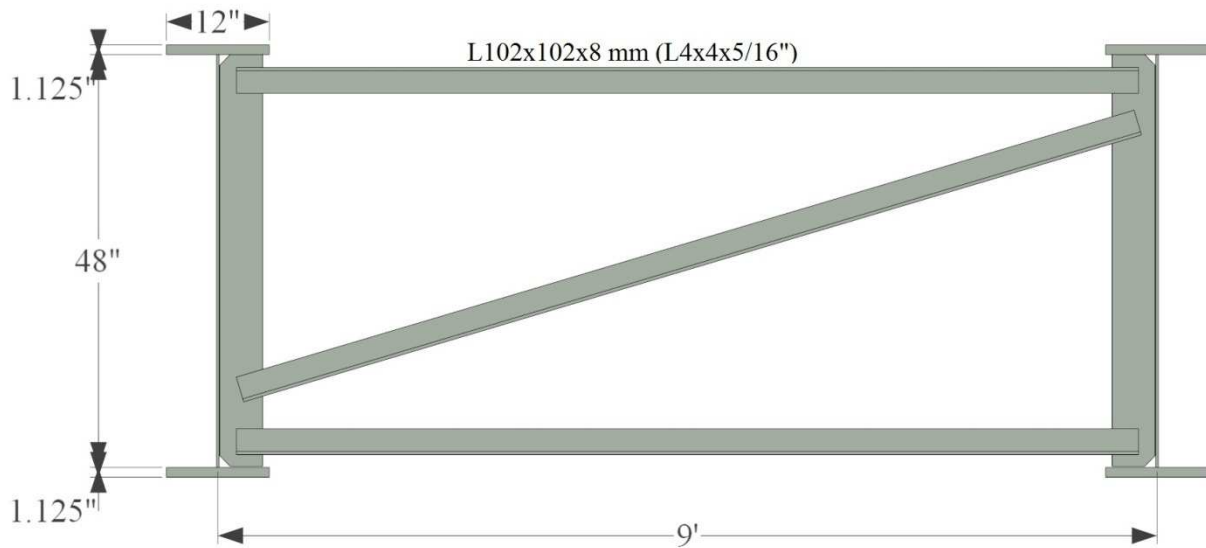
Figure 2. Schematic of interior section of bridge over the middle span.

Factors Affecting Development of Fatigue Cracks in Kansas Bridge 135-87-43/44

Cracks in web gap regions can form in skewed, curved, or straight bridges, but cracks tend to be more extensive and initiate earlier in skewed and curved bridges. This is thought to be in part because larger differential vertical deflections tend to occur in skewed and curved bridges than in straight bridges (10). Kansas Bridge 135-87-43/44 has a skew angle of 21°, which is a relatively modest skew angle.

In Kansas Bridge 135-87-43/44, cross-frames are staggered perpendicular to the girders between bearing points, which is a common configuration in bridges skewed more than 20°. It has been shown that cracking is likely to occur in a bottom web gap region in a staggered cross-frame layout (11, 3) due to the discontinuous load path between cross-frames or diaphragms. Crack locations listed in a 2010 routine snooper report for Bridge 135-87-43/44 showed that the majority of cracks occurred near the bottom flange. Cracks also occurred in the top web gap region near bearings in the negative moment region.

The highest concentration of cracking in Bridge 135-87-43/44 occurred towards the center of the middle span, which is 29-m (95-ft.) long. It has been shown that differential deflections between adjacent girders are greatest for short spans with large skew angles, with the greatest differential deflections occurring when the span length is 30.5 m (100 ft.) (2). The span length of Bridge 135-87-43/44 is very similar to this latter value, helping to provide context to the development of significant levels of fatigue cracks in this bridge structure.

Fatigue Crack Types and Retrofit Measures

Fatigue cracks have been found throughout the superstructure of Kansas Bridge 135-87-43/44. Crack locations in Bridge 43 carrying southbound traffic can be seen in Figure 3. The majority of cracks are located in the interior girders between supports, and cracking is concentrated near the center line of the bridge.

Four types of fatigue cracks are classified on the structure, and are designated as A-, B-, C-, and D-type cracks. Type A cracks are located at the connection stiffener-to-girder web weld. Type B cracks occur along the connection stiffener-to-girder web weld. Type C cracks have propagated away from a weld into the base metal of the girder web, and Type D cracks occur between the web and top flange. In the southbound Bridge 43, Type A cracks were the most prevalent throughout the bridge. The most severe crack geometry, Type C, was found in all spans, but only in a few locations.
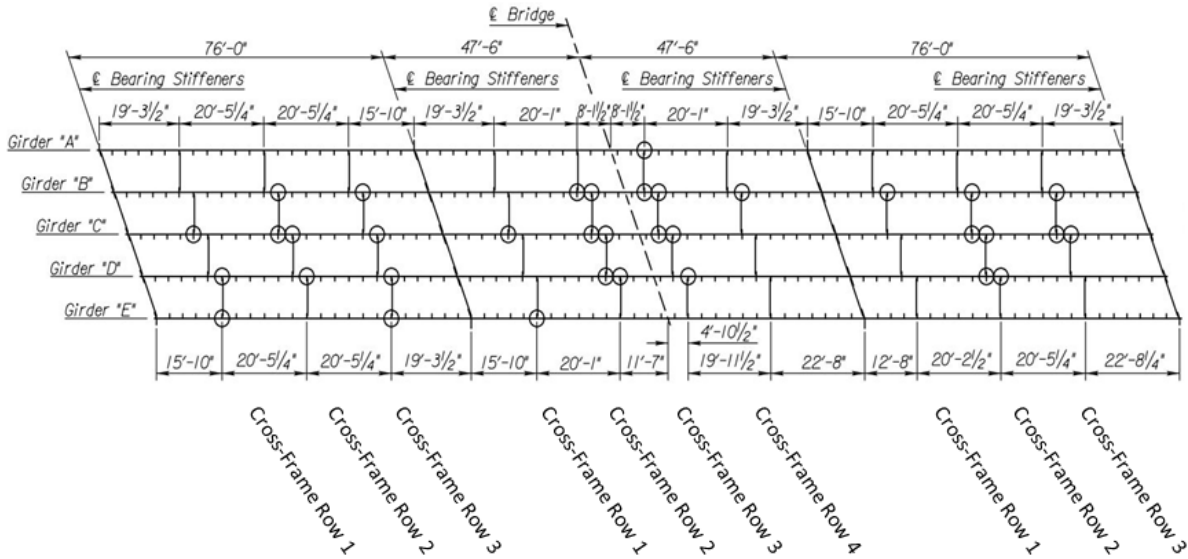
Figure 3. Crack locations in Bridge 43 carrying I-135 traffic.

In past repairs of Bridge 135-87-43/44, cracks have been arrested by drilling crack-arrest holes. Figure 4 shows a photograph of crack-arrest holes drilled at the tips of Type B, C, and D cracks in Girder C near the second cross-frame in Span 1. The 2010 inspection recorded no new growth at these cracks. No other retrofits have been previously applied to the twin bridges.
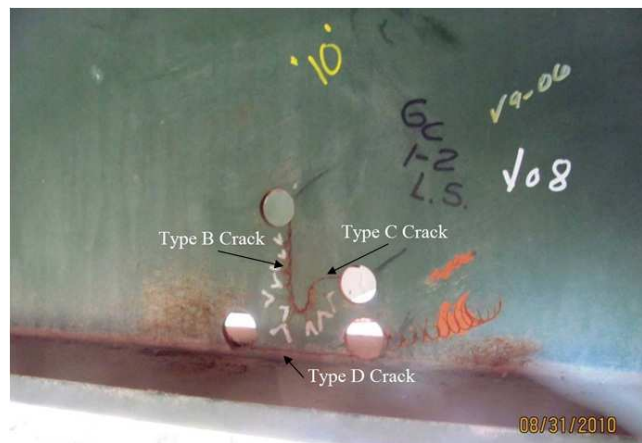

Figure 4. Drilled crack-stop holes at tips of type B, C, and D cracks.

In other bridges, KDOT has implemented different retrofits depending on crack type. The retrofit for a Type A crack involves installing a full depth web splice plate on both sides of

the connection plate. Type B retrofits install angles to the connection plate and the bottom flange. Angles are attached between the connection stiffener and adjacent flange when retrofitting a Type C crack. A back-up stiffener is attached to repair a Type D crack, and one angle is installed between the new back-up stiffener and bottom flange.

Objective

The objective of this study was to determine the most effective retrofit to stop further initiation and propagation of fatigue cracks in a skewed, staggered bridge configuration present in the I-135 bridges over Chisholm Creek. The retrofit chosen by the Kansas Department of Transportation will then be implemented throughout the length of the twin bridges.

Finite Element Modeling Methodology

Full scale finite element models of Bridge 135-87-43/44 were created using ABAQUS version 6.10-2. A screenshot of the model is presented in Figure 5. All materials were modeled as linear elastic.
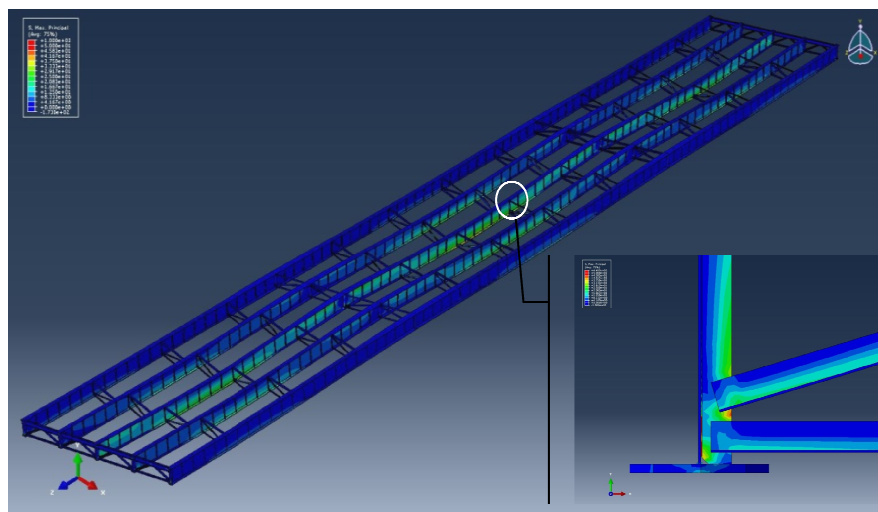

Figure 5. Full scale model of bridge with concrete deck removed for clarity. Close-up of cross frame three at Girder C is shown in the insert.

The modulus of elasticity of the steel was specified as 200,000 MPa (29,000 ksi) and Poisson's ratio was 0.3. The steel girders had varying mesh sizes, with the densest mesh near the web gap regions. The mesh in the web at the retrofit location was a mixture of 2.54-mm (0.1-in.) swept and structured hexagonal elements due to some retrofits requiring bolts through the web. Tetrahedral elements were used to transition to coarser elements. This highly dense mesh was specified over a 660-mm (26-in.) width to separate stress risers that were present between the tetrahedral and hexagonal elements and the web gap regions.

All five steel girders were modeled, and 8-mm (5/16-in.) fillet welds connecting the flanges to the web were modeled as right triangles. Intermediate stiffeners were modeled in addition to transverse connection stiffeners. 4.8-mm (3/16-in.) welds were modeled on both sides to attach the connection plates to the webs, but for simplicity, the intermediate stiffeners were attached to the webs using tie constraints only.

The concrete deck, haunches, and barriers were also modeled. The sloped deck and two side barriers were modeled as one part, while the haunches were five individual parts. Tie constraints were used to connect the concrete haunches to the steel top flanges. The concrete deck was comprised of hexagonal elements approximately 508×508-mm (20×20-in.). The modulus of elasticity of the concrete was taken as 25,000 MPa (3,605 ksi) and Poisson's ratio was 0.2.

Hard contacts were used between the angles used in retrofits and the bottom web gap of Girder C. A friction coefficient was used when specifying a hard contact for steel to steel contact and was set to 0.35. Tie constraints were initially used to connect angles to the girder, but stress risers occurred at the end of the angles. This was deemed an artifact of the model since these areas of high stress were no longer present once hard contacts were applied.

The bridge is symmetric about the diagonal that runs from the southeast corner to the northwest corner. Cross-frames were modeled in the same fashion as the steel girders, using hexagonal, solid elements. The end supports of the bridge are rockers, and the two interior supports are bolsters. These bearings were modeled as rollers and pins, respectively.

The mass density of the bridge was specified to include dead loads for the superstructure, calculated by dividing the material density by gravitational acceleration. A 112 kN/m (0.64-K/ft) lane load was applied to Girder C over a 457-mm (18-in.) flange width throughout the length of the bridge.

Two cracks were explicitly modeled in the top and bottom web gaps of the third cross-frame of span two in Girder C. A row of elements was removed to model cracks explicitly. The cracks modeled included a 25-mm (1-in.) horseshoe-shaped crack at the stiffener-to-web weld and a 51-mm (2-in.) web-to-flange weld crack. This same crack configuration was placed in the top and bottom web gaps. Cracks were placed in the bottom web gap because a large number of cracks were found in this location when compared to other locations during routine inspections. Cracks were placed in the top web gap to determine if retrofits that effectively worked in the bottom, could also work in the top. Stress fields surrounding these two cracks are shown in Figure 6.
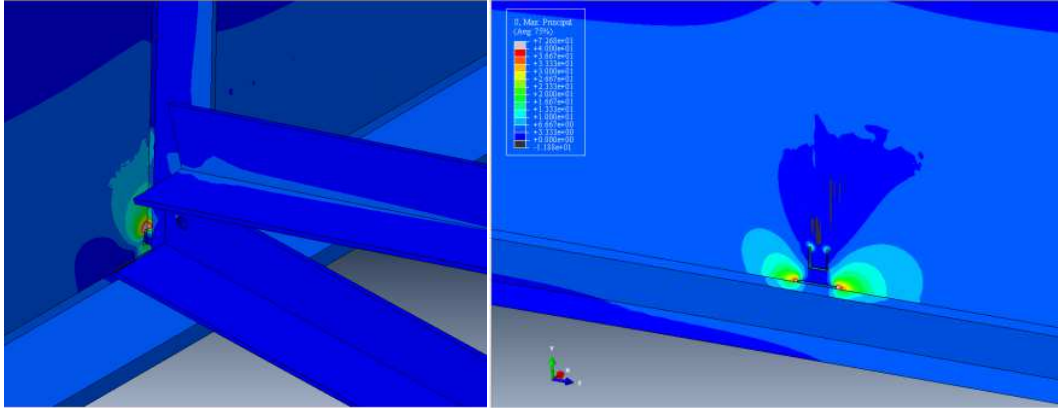
(a)   **(b)**

Figure 6. Two crack locations in cross frame number three of Girder C. (a) 25-mm (1-in.) long web-to-stiffener weld crack (b) 51-mm (2-in.) long flange-to-stiffener weld crack.

Retrofit Measures

The Hot Spot Stress (HSS) technique was used to compare various retrofits. This technique is used to determine the stress near a weld where stress magnitudes can be very high. Maximum principal stress values were obtained from nodes taken half the thickness of the web away from the weld in an uncracked web. In models that included cracks, paths followed the length of the cracks and around the crack tips to capture the high stress present near the crack tips. HSS 1 was used to determine stresses around the web-to-stiffener weld on the cross-frame side of Girder C. HSS 2 was taken around the web-to-flange weld on the fascia side of Girder C. HSS 1 and 2 paths can be seen in Figure 7 on a bridge with no retrofit.
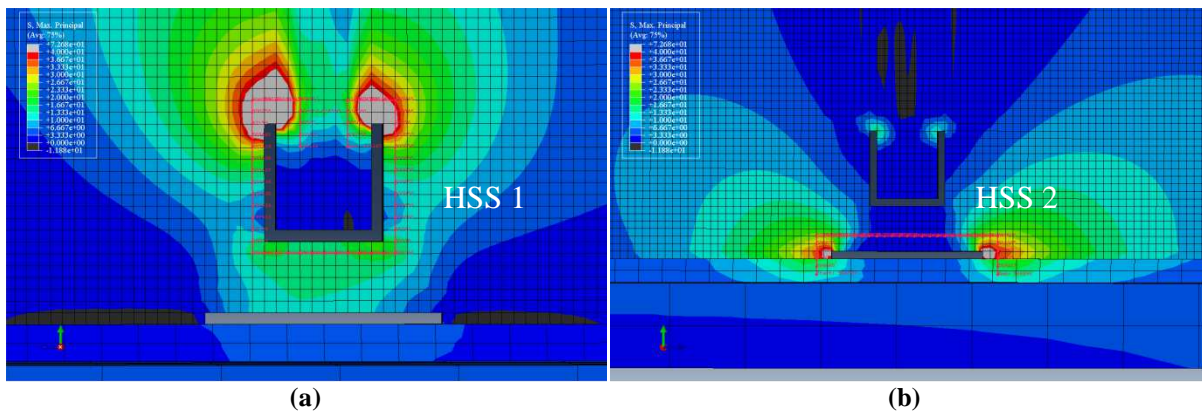

(a)   **(b)**

Figure 7. Hot spot stress paths near cracks along the (a) web-to-connection plate weld and (b) web-to-bottom flange weld.

All bolts and bolt holes were 19-mm (3/4-in.) in diameter. Bolts were modeled by merging the head, shank, and nut together into one part. A pre-tensioned bolt load was applied to the middle of the shank, according to the magnitude provided in the AISC Specification (12). Bolt loads were applied in the model step prior to the lane load being added. The back face of the bolt and nut were tied to the surfaces of the steel members that were connected. Hard contacts were used between holes in the steel members and shanks of bolts to model the interaction between these parts that might take place when plates bend or shear against each other.

Four retrofits were modeled, and all stiffened the web gap region through the use of angles. Retrofit 1 involved two angles bolted to the connection plate and web along with a backing plate on the fascia side of the web. A parametric analysis of this retrofit was performed to determine the optimal size of the angles and backing plate. Retrofit 2 also bolted angles to the connection plate and web, but a backing angle bolted to the bottom flange and web replaced the backing plate. The third retrofit studied angles bolted to the bottom flange and connection plate. Finally, Retrofit 4 investigated a proposed retrofit made by KDOT. In this retrofit angles are placed at each end of the cross-frames as a means to stiffen all web gap regions.

The first retrofit investigated was the angles with backing plate, which is shown in Figure 8. Two 94-mm (3.7-in.) long 152×152×25-mm (L6×6×1-in.) angles were bolted to the web, connection plate, and a 457×144×25-mm (18×5.6875×1-in.) backing plate was connected to the fascia side of the web. A small shim plate was used to allow the angle to fit tightly against the cross-frames without needing to first remove them. Retrofit 1 was studied in both the bottom and top web gaps. There is no connectivity to the tension flange in this retrofit, which is ideal in top web gaps because the concrete deck does not need to be removed. It was possible to attach
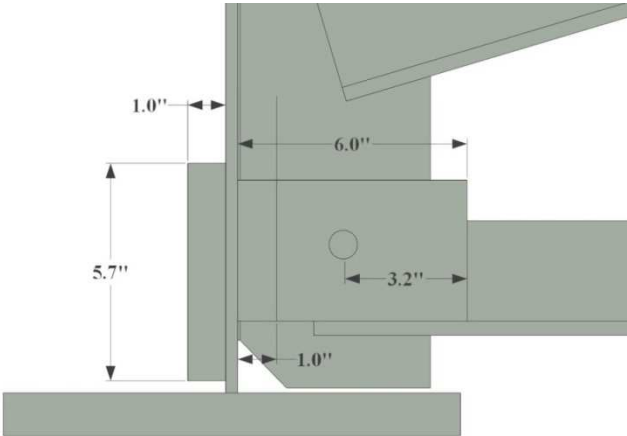
the backing plate to the web because the cross-frames were staggered. At the supports where cross-frames are back-to-back, angles could be attached to the connection plates and web on both sides of the web; however, this was not included in this investigation.
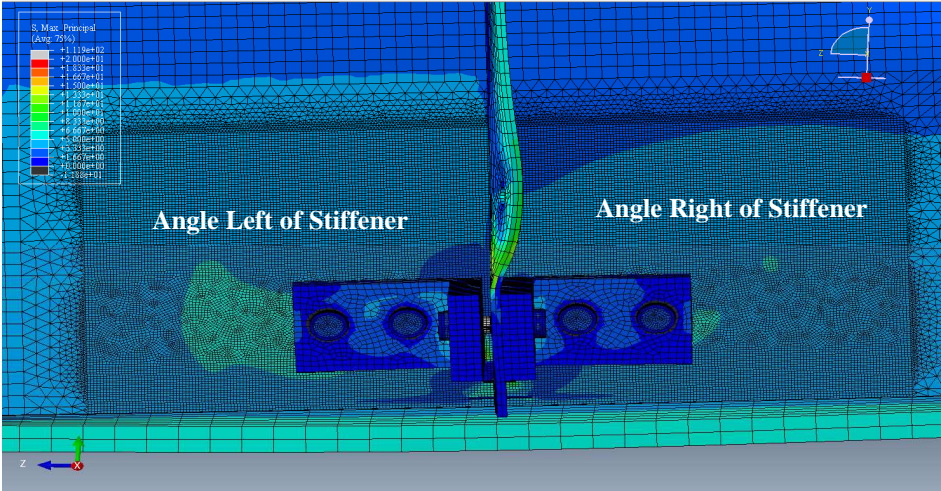
(a)
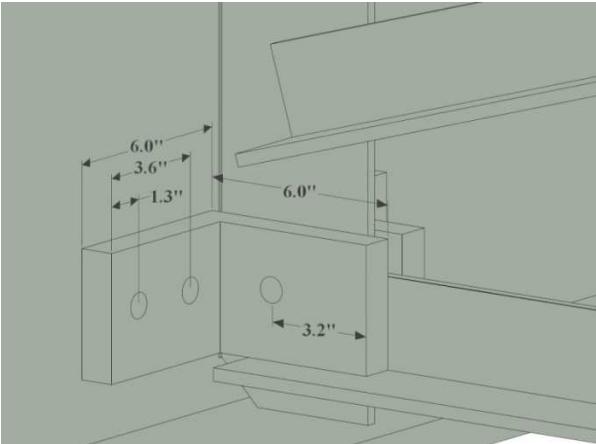
(b)

(c)

Figure 8. (a) Two 152×152×25 (6×6×1) angles bolted to both sides of the connection plate with a backing plate on the fascia side of the girder. (b) cross-frame side of Girder C (c) cross-section of bottom web gap with retrofit.

In the bottom web gap when compared to a cracked, unretrofitted configuration, Retrofit 1 reduced HSS 1 by 80% and HSS 2 by 82%. This is significant stress reduction in the web gap,

but the transverse connection plate was found to distort about its weak axis, which is shown in Figure 8(a).

Free body cuts were taken at the middle of each cross-frame framing into Girder C where stress values were pulled. The top and bottom cross-frames had compressive forces with minimal load, while the middle cross-frame was carrying the only tensile force. Figure 9 displays the middle cross-frame with an 18-kN (4-kip) tensile force at the center of the cross-frame's length.
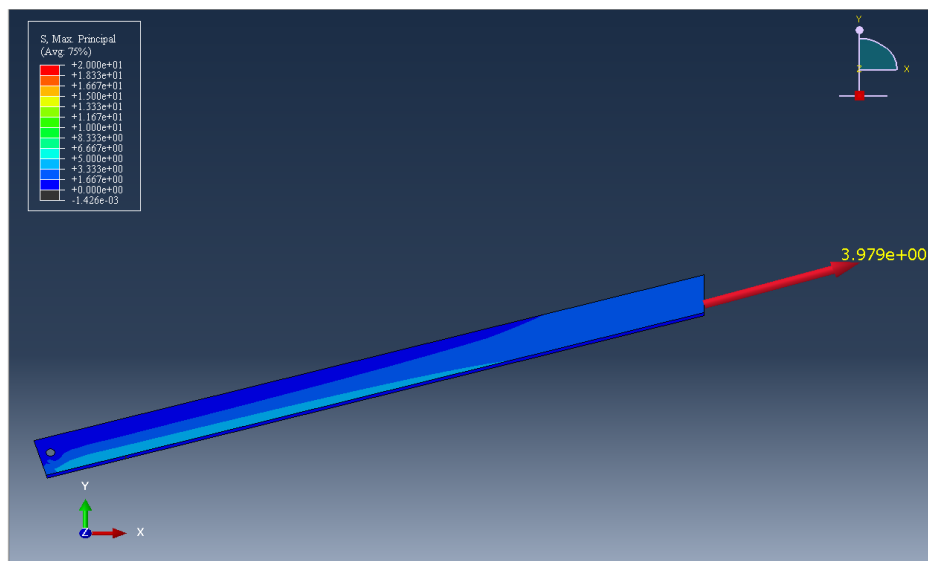

Figure 9. Force in middle cross-frame framing into the bottom web gap of Girder C.

A variation of Retrofit 1involved lengthening the angle on the right side of the connection plate to attempt to counteract the tensile force from the middle cross-frame that caused the connection to bend out-of-plane. The angle was lengthened to 305-mm (12-in.), as seen in Figure 10. The height of the back plate was also increased to bolt the 305-mm (12-in.) long angle to the web. The time required to drill holes in the field was kept to a minimum by only adding two more bolts to the 305-mm (12-in.) long angle. The side of the back plate above the 152-mm (6-in.) long angle was not bolted to the web. HSS 1 was found to reduce by 82% and

HSS 2 reduced stress by 83% when compared to a cracked, unretrofitted bridge. The deformed shape of the connection plate, shown in Figure 10, was much less than the deformations of the connection plate shown in Figure 8(a), so although stress values did not greatly decrease, a potential new problem area at the connection plate was avoided by using a 305-mm (12-in.) long angle on the right side.
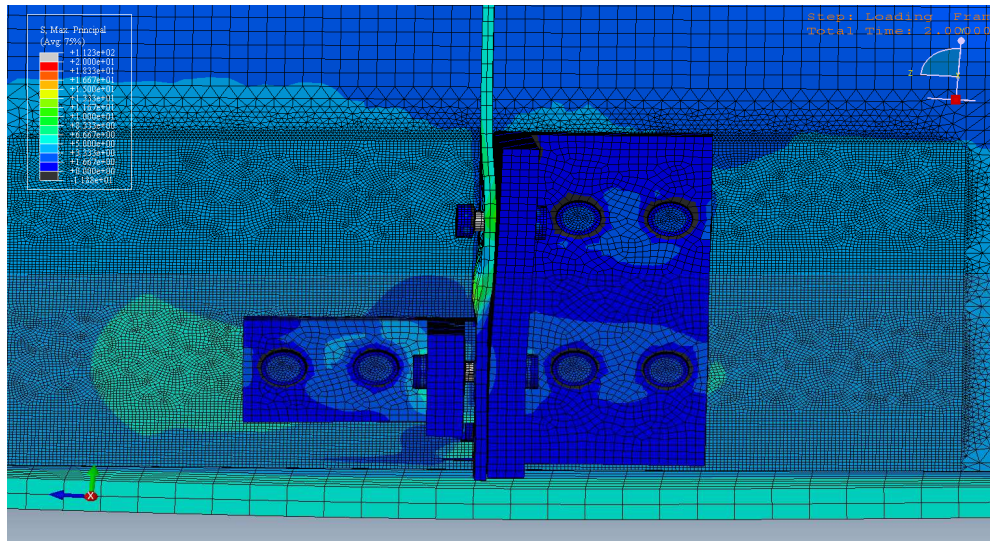

Figure 10. Angles with backing plate retrofit. Angle on the right is 305-mm (12-in.) long; angle on left is 152-mm (6-in.) long. Cross-frames have been removed for clarity. (Stress scale is from 0 – 140 MPa (0 – 20 ksi); deformation scale is 100).

A vertical stress path was taken along the left and right side of the transverse stiffener to determine the stresses that caused the stiffener to deform out-of-plane. Paths were taken from the angles with backing plate retrofit when both angles were 94-mm (3.7-in.) long and when the right angle was 305-mm (12-in.) long. In these two simulations, the thickness of the angles and back plate was 25-mm (1-in.). Stress paths on the left and right side of the stiffener for these two retrofits are shown in Figure 11. A larger amount of stress was present in the stiffener when the right angle was 305-mm (12-in.) long. The location of high stress is visibly different in Figure 11(b) versus Figure 11(d), and this difference is due to the different angle lengths.
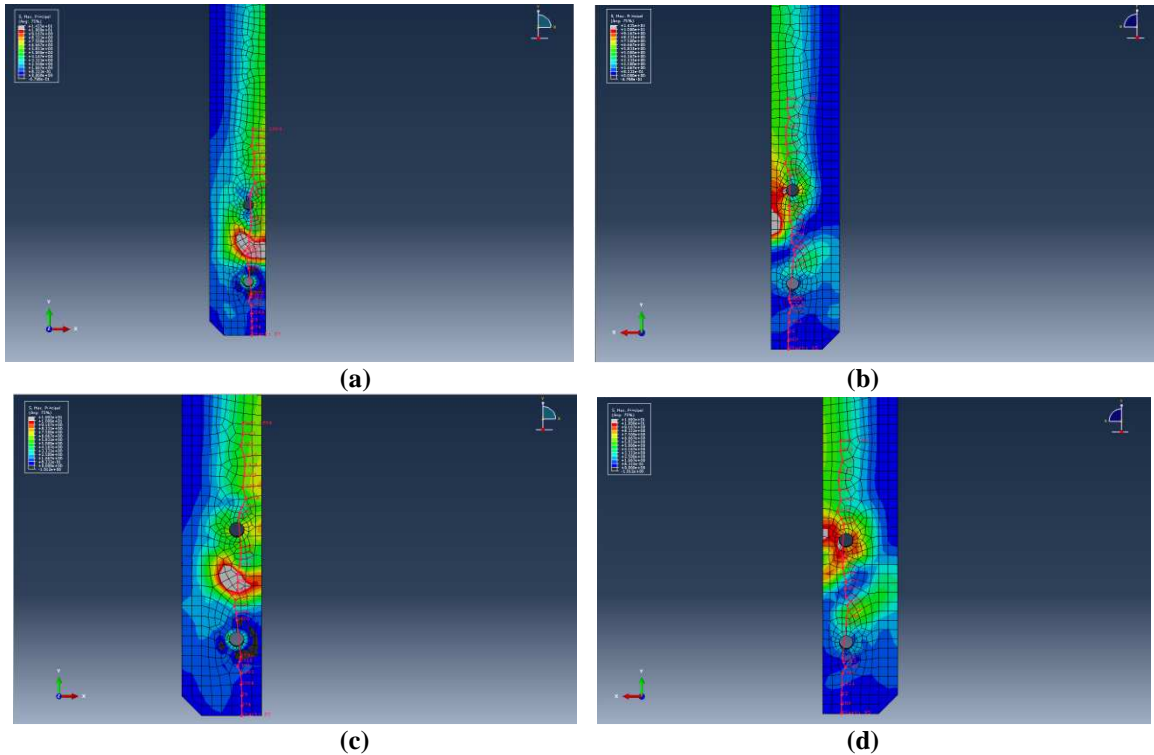
Figure 11. Angles with a backing plate retrofit. The paths are shown in red. (a, b) Left and right side of the stiffener when both angles are 94-mm (3.7-in.) long and (c, d) left and right side of the stiffener when the right angle is 305-mm (12-in.) long.

A parametric analysis of Retrofit 1 was performed in which the dimensions of the angles and backing plate were varied to determine which reduced the stress in the web gap region the greatest. In Figure 8(a), the angle to the left and right of the stiffener are denoted because the dimensions of each angle were sometimes varied separately. The first range of models varied the thickness of the angles and backing plate from 13-mm to 19-mm to 25-mm (0.5-in. to 0.75-in. to 1-in.). The same 152×152×25 mm (6×6×1-in.) angles were used throughout. The angle to the left of the stiffener was 94-mm (3.7-in.) long and the angle to the right of the stiffener was 305-mm (12-in.). The backing plate was 457-mm (18-in.) long, and 305-mm (12-in.) high. Results from this studied are shown in Table 1. When 25-mm (1-in.) thick angles and backing plate were used, the percentage of original HSS values was the lowest, with HSS 1 and 2 equal to 18%

and 17%, respectively. As the thickness decreased to 13-mm (0.5-in.), HSS 1 and 2 were greater than 2.5× the stress found when the 25-mm (1-in.) thick angles were applied.

Table 1. Retrofit 1: Angles and backing plate retrofit with varying thicknesses.

Dimensions			% of Original HSS 1	% of Original HSS 2
Angle Left of Stiffener – Bottom Web Gap mm (in.)	Angle Right of Stiffener- Bottom Web Gap mm (in.)	Back Plate – Bottom Web Gap mm (in.)		
L152×152×**25** 94 long (L6×6×**1** 3.7 long)	L152×152×**25** 305 mm (L6×6×**1** 12 long)	457 long, 305 high, **25** thick (18 long,12 high, **1** thick)	18%	17%
L152×152×**19** 94 long (L6×6×**¾** 3.7 long)	L152×152×**19** 305 mm (L6×6×**¾** 12 long)	457 long, 305 high, **19** thick (18 long,12 high, **¾** thick)	27%	25%
L152×152×**13** 94 long (L6×6×**½** 3.7 long)	L152×152×**13** 305 mm (L6×6×**½** 12 long)	457 long, 305 high, **13** thick (18 long,12 high, **½** thick)	45%	48%

Next, the angles thickness was set to 13-mm (½-in.) thick while the backing plate was 25-mm (1-in.). This analysis was performed to determine which member, the angles or the backing plate, affected HSS 1 and 2. It was also important to investigate if one member could be thick, while the other was thin to decrease the amount of material needed. In Table 2, it can be seen that by using thinner angles, stresses along the web-to-connection plate weld crack have decreased the same as if a 19-mm (¾-in.) thick angle were used. Stresses along the web-to-bottom flange weld crack have decreased almost as much as when both the angles and backing plate had a 25-mm (1-in.) thickness.

Table 2. 13-mm (½-in.) thick angles with a 25-mm (1-in.) thick back plate.

Dimensions			*% of Original* *HSS 1*	*% of Original* *HSS 2*
Angle Left of Stiffener – Bottom Web Gap *mm (in.)*	*Angle Right of Stiffener- Bottom Web Gap* *mm (in.)*	*Back Plate – Bottom Web Gap* *mm (in.)*		
L152×152×13 94 long (L6×6×½ 3.7 long)	L152×152×13 305 mm (L6×6×½ 12 long)	457 long, 305 high, 25 thick (18 long, 12 high, 1 thick)	27%	19%

Placement of the angle to the left of the stiffener in this bridge configuration is difficult because of the small cross-frames used. The dimensions of the angle on the right of the stiffener are easily altered because there are no obstructions. Another parametric study was performed on the angle to the left of the stiffener to determine what the shortest angle could be used. The height of the angle was varied from 94-mm to 76-mm to 51-mm (3.7-in. to 3-in. to 2-in.), and the results are shown in Table 3.

A 203×152×25-mm (8×6×1-in.) angle was used throughout this study. It was found that varying the height of the angle on the left did not have a significant impact on HSS 1 or 2 stresses. The difference in stresses between a 51-mm (2-in.) and 94-mm (3.7-in.) long angle was only 3% for HSS 1 and 4% for HSS 2. Therefore, shorter angles can be used in other bridge configurations where there are limitations due to geometry.

Table 3. L203×152×25 (L8x6x1) used on the left and right side of the stiffener. Length of the angles was varied.

Dimensions			% of Original HSS 1	% of Original HSS 2
Angle Left of Stiffener – Bottom Web Gap *mm (in.)*	*Angle Right of Stiffener- Bottom Web Gap* *mm (in.)*	*Back Plate – Bottom Web Gap* *mm (in.)*		
L203×152×25 **94 long** (L8×6×1 **3.7 long**)	L203×152×25 **94 long** (L8×6×1 **3.7 long**)	508 long, 144 high, 25 thick (20 long, 5.7 high, 1 thick)	20%	18%
L203×152×25 **76 long** (L8×6×1 **3 long**)	L203×152×25 **76 long** (L8×6×1 **3 long**)	508 long, 144 high, 25 thick (20 long, 5.7 high, 1 thick)	21%	19%
L203×152×25 **51 long** (L8×6×1 **2 long**)	L203×152×25 **51 long** (L8×6×1 **2 long**)	508 long, 144 high, 25 thick (20 long, 5.7 high, 1 thick)	23%	22%

An additional comparison can be made between angles with a leg connected to the web that is 203-mm (8-in.) and 152-mm (6-in.). The other leg of the angle bolted to the stiffener was kept constant at 152-mm (6-in.). This change in length was found to not have any effect on HSS 1 or 2 stresses.

A 51-mm (2-in.) long web-to-flange weld crack and a 25-mm (1-in.) web-to-stiffener weld crack was added to the top web gap of Girder C in addition to the cracks that were in the bottom web gap of Girder C. This location was chosen because of cracks reported in top web gaps between supports in the 2010 Routine Snooper Inspection. Cracks were not placed in top web gaps located in negative moment regions because no cracks were circled in these locations, as seen in Figure 3. In the bottom web gap, HSS 1 and 2 paths were taken on the cross-frame side of Girder C. In the top web gap, HSS 1 had greater stress values on the cross-frame side,

while HSS 2 had higher stresses on the fascia side of the girder. HSS 2 in the top web gap, on the fascia side was 6.8 ksi, and HSS 1 in the top web gap, on the cross-frame side was 7.1 ksi. 152×152×25-mm (6×6×1-in.) angles were bolted on both sides of the connection plate and web in the top and bottom web gaps. On the fascia side of the web, a 457×145×25-mm (18×5.7×1-in.) back plate was applied in the top and bottom web gaps. The percentage of original HSS 1 stress once this retrofit was applied was 66%, and for HSS 2 it was 72%. Stresses overall in this top web gap were small when compared to stresses in the bottom web gap.

Retrofit 2 replaced the backing plate with a 457-mm (18-in.) long, 152×152× 25-mm (6×6×1-in.) angle bolted to the fascia side of the web and bottom flange. The backing angle was used to provide additional connectivity between the flange and web. Figure 12 shows a schematic of this retrofit. HSS 1 values for both the backing plate and backing angle showed that stress was reduced by the same amount for the two retrofits. HSS 2 stress values were slightly lower for Retrofit 2 than when the backing plate was used (Retrofit 1), with a stress reduction of 83%, as compared to 82% with the backing plate. It is believed that the extra labor and material required to install the backing angle is not merited since the stress was not found to significantly decrease when compared to the backing plate.
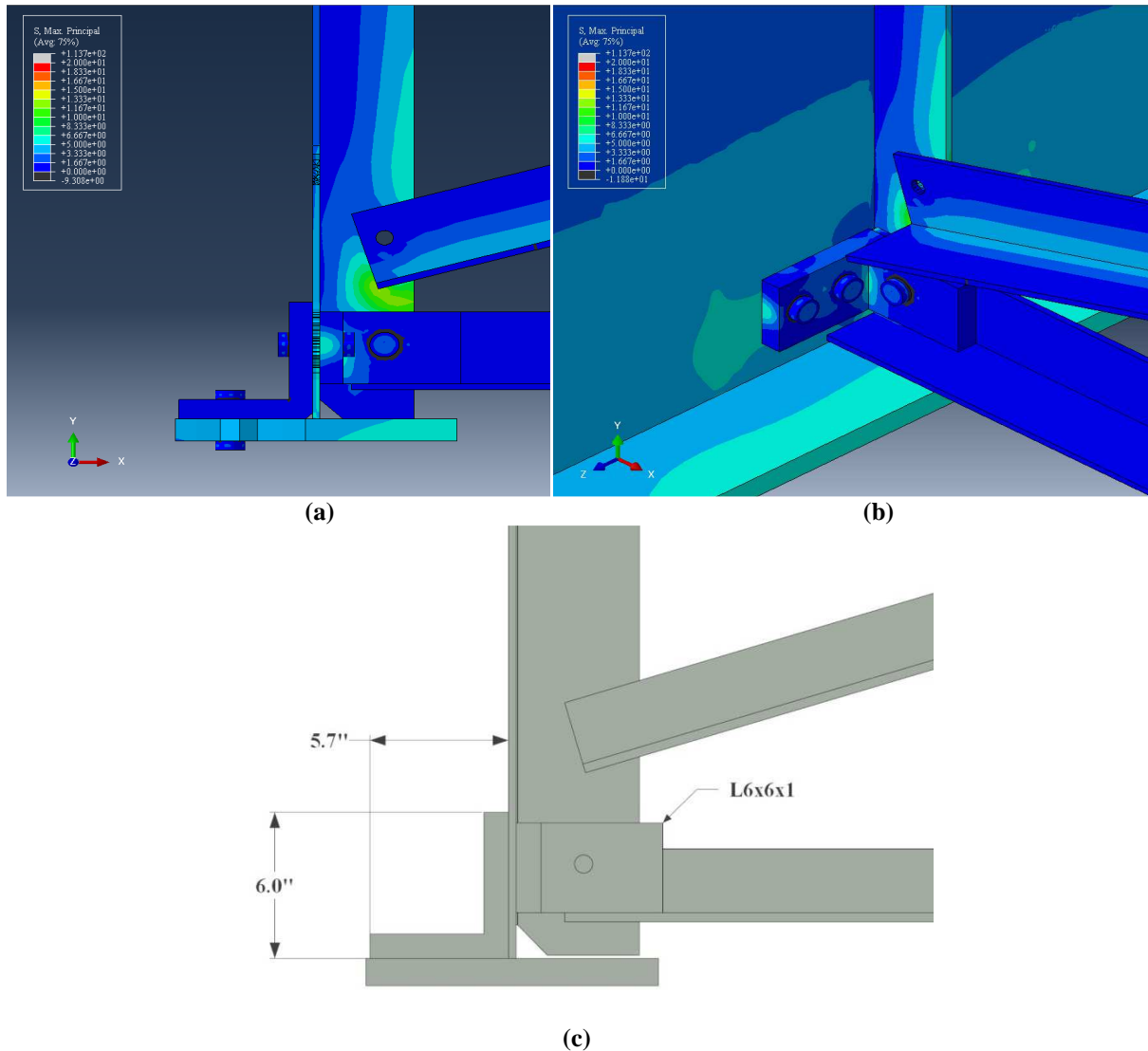
(a)

(b)

(c)

Figure 12. (a) Cross section view of angles connected to the stiffener and web with a backing angle bolted to the bottom flange and web. (b) view of stiffener-to-web angles. (c) schematic of retrofit.

In the third retrofit investigated, two 140-mm (5.5-in.) long, 152×152×16-mm (6×6×5/8-in.) angles were bolted to both sides of the connection plate and the bottom flange. A thinner angle than what was used in Retrofits 1 and 2 had to be used because a bolt head would not fit between the top of the angle leg connected to the bottom flange and the bottom of the horizontal cross-frame. This retrofit is often used in the field to fasten the connection plate to the flange. As previously discussed, construction of this retrofit could be expensive and intrusive when

applied in a top web gap due to interferences with a concrete deck. In the bottom web gap where this retrofit was applied, the welded bottom cross-frame had to first be removed. If the angles were used in the top web gap, the top cross-frame member would need to be removed in addition to the concrete deck. A total of four angles were used, two in the bottom web gap of Girder C, and two in Girder D. When this retrofit is compared to the cracked, unretrofitted specimen, HSS 1 decreased by 72% and HSS 2 by 77%. The connection plate bent out of plane above the 152-mm (6-in.) long angle leg, which can be seen in Figure 13(a.)

To improve this retrofit, the vertical leg of the angle on the right side of the connection plate was extended to 305-mm (12-in.), as shown in Figure 13(b). The angle leg length was only increased on the right side so that the diagonal cross-frame member did not need to be removed also. Originally the diagonal cross-frame member was welded to the connection plate, so a bolt hole could easily be drilled in the field without removing the brace. By lengthening the vertical leg of the angle on the right, it was found that HSS 1 decreased by 79% and HSS 2 decreased by 81% when compared to a cracked, unretrofitted bridge. The 305-mm (12-in.) long angle leg provided greater stress reduction for both HSS 1 and 2 than the 152-mm (6-in.) long angle leg with little additional material or labor needed. Therefore, it is believed that using a longer angle segment on one side of the connection plate is warranted for this particular retrofit geometry.
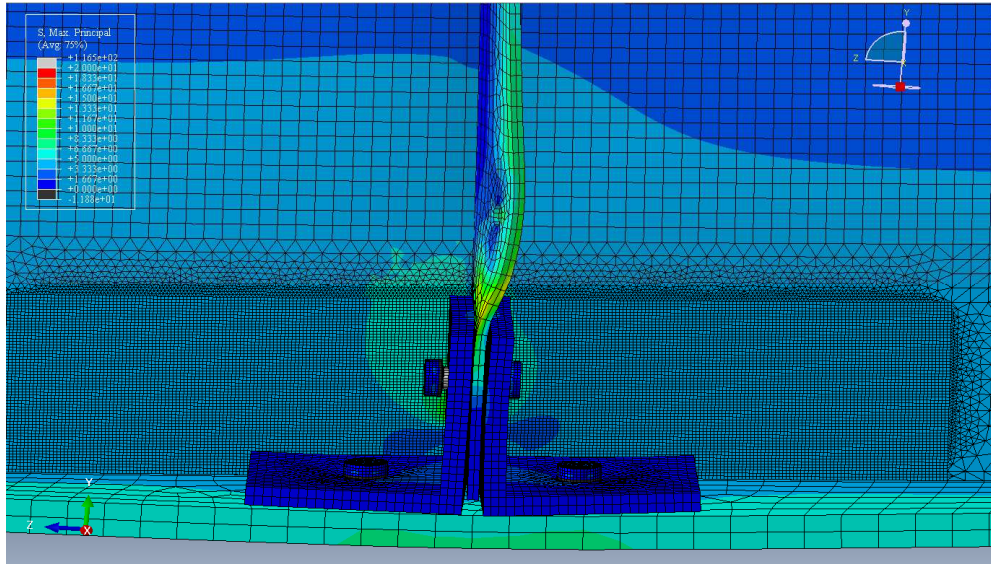
(a)
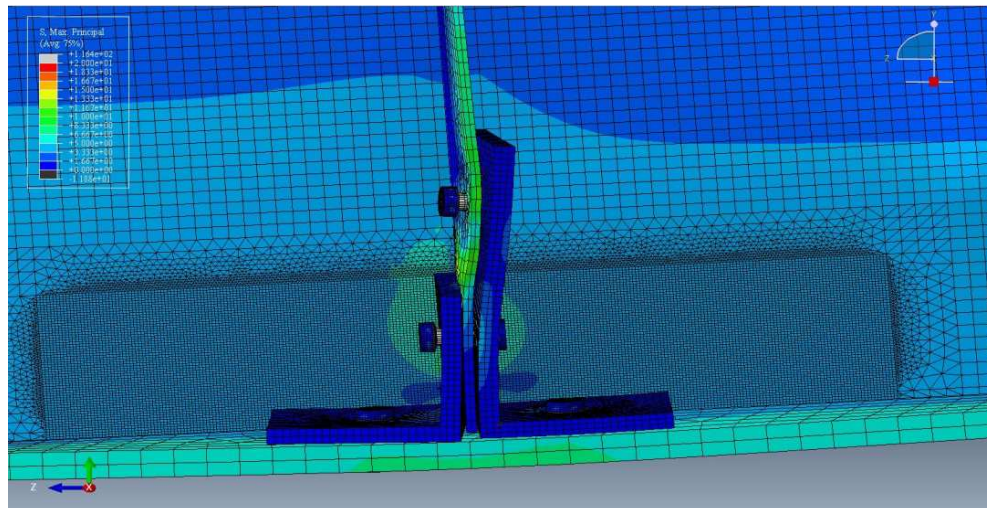
(b)

Figure 13. Connection plate-to-bottom flange angle retrofit (a) 152×152×16-mm (6×6×0.625-in.) angles and (b) 152×152×16-mm (6×6×0.625-in.) on the left side of the connection plate and a 305×152×16 mm (12×6×0.625-in.) angle on the right side of the connection plate. (Stress scale is from 0 – 140 MPa (0 – 20 ksi); deformation scale is 100).

The fourth retrofit investigated utilized a 203×203×16-mm (8×6×5/8-in.) angle with a length of

305-mm (12-in.) was bolted to the connection plate and web. Because the angles were long, all

cross-frame members had to be first removed to attach angles to each corner of the cross-frames.

Placement of all angles is shown in Figure 14.
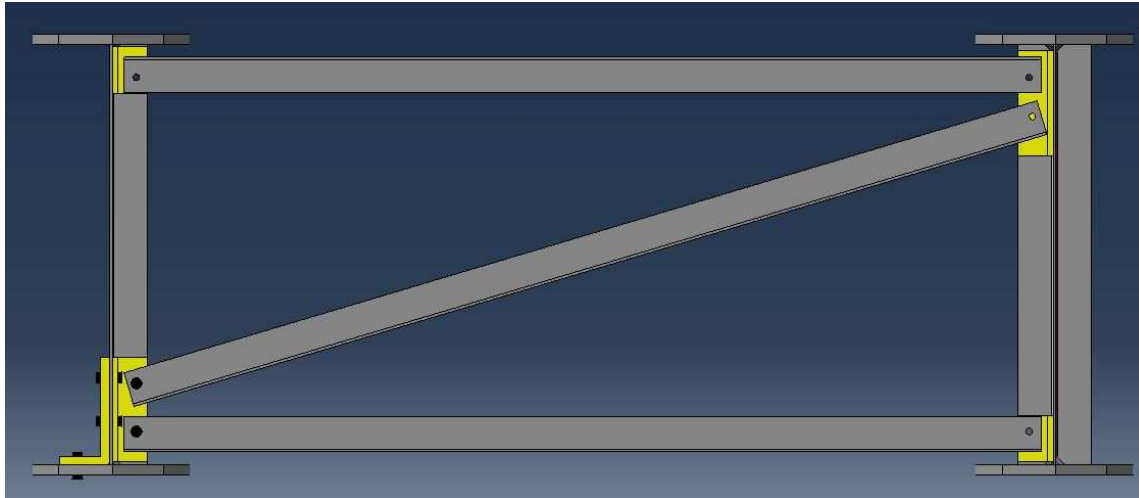
Figure 14. Placement of angles in four corners of the K-brace configuration. Girders C is on the left and Girder D is on the right. Angles are shown in yellow.

A pair of 305-mm (12-in.) long angles was used in the bottom web gap of Girder C and in the top web gap of Girder D, and a pair of 153-mm (6-in.) long angles was used in the top web gap of Girder C and in the bottom web gap of Girder D. A 145×312×25-mm (5.7×12.3×1-in.) bent plate was bolted to the bottom flange and web on the fascia side of Girder C. Figure 15 shows a basic plan of this retrofit. During construction of the bridge, a bolt was placed in the bottom cross-frame member, such that a longer bolt only needs to be inserted to attach the angles. With the diagonal and top cross-frame members, holes must be drilled on both ends of each cross-frame, for a total of four holes.
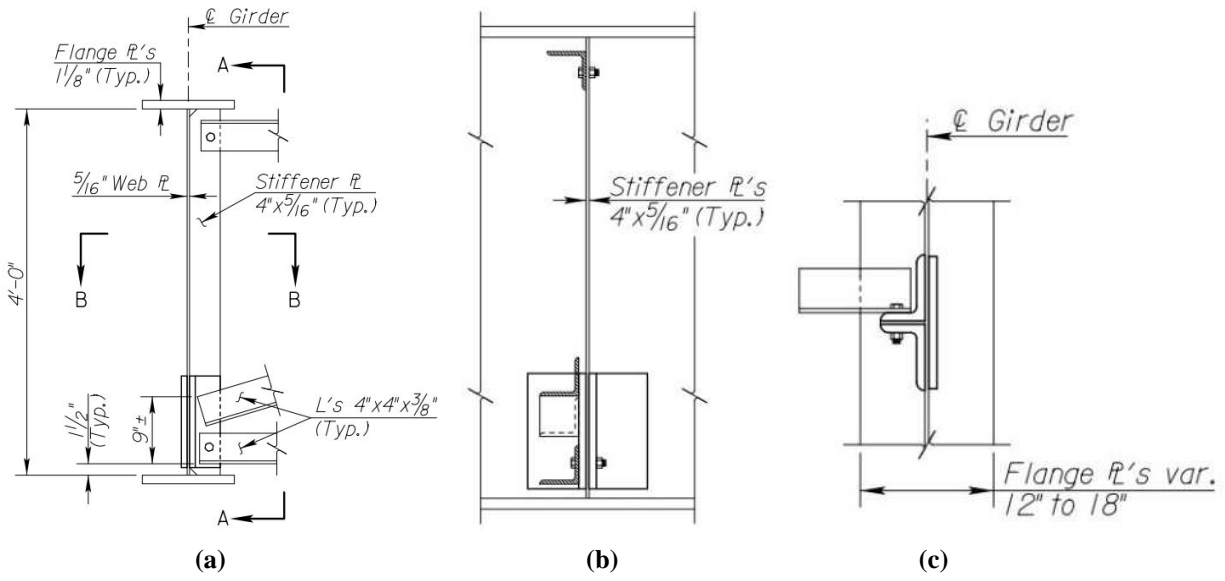
Figure 15. Proposed retrofit elevation from KDOT (a) Side view (b) Section A-A (c) Section B-B.

Retrofit 4 is expected to require more labor and material than the other three retrofits examined, and the retrofit may need to be applied in all web gaps if cracks are present. HSS 1 and HSS 2 were reduced by 71% and 75% respectively, after the retrofit was applied when compared to cracked, unretrofitted bridge. The stress fields can be seen in Figure 16. The connection plate deformed out-of-plane much less than the previous retrofits, but stress values were higher than found after the other retrofits were applied. It should also be noted that the previous retrofits might result in new problem where the stiffener deforms out-of-plane because the angles used were not long enough. From the *4Angles* retrofit, it can be seen that a longer angle prevents out-of-plane distortion of the transverse stiffener.
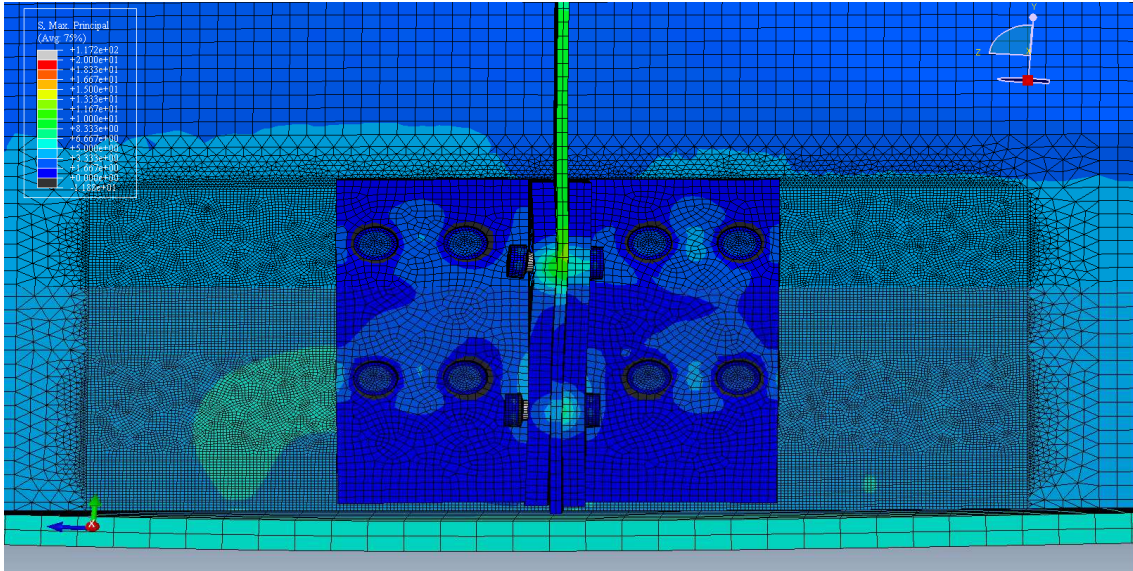
Figure 16. Stress in the bottom web gap of Girder C for the 4Angles retrofit. (Stress scale is from 0 – 140 MPa (0 – 20 ksi; Deformation scale = 100).

In Figure 17, the four retrofits investigated are compared to HSS 1 and HSS 2 values from a cracked bridge model with no retrofit. In all five models compared, cracks in the welds connecting the flange-to-web and stiffener-to-web were included. Similar stress reductions were found when angles were attached to the stiffener and web with either an angle or backing plate on the fascia side of the web. HSS 1 stresses were reduced the most when a backing angle was attached to the fascia side of the web and the bottom flange, while HSS 2 decreased the most when a backing plate was applied. After these two retrofits, the next most effective retrofit was the labor intensive retrofit connecting angles to every corner of the cross-frames.
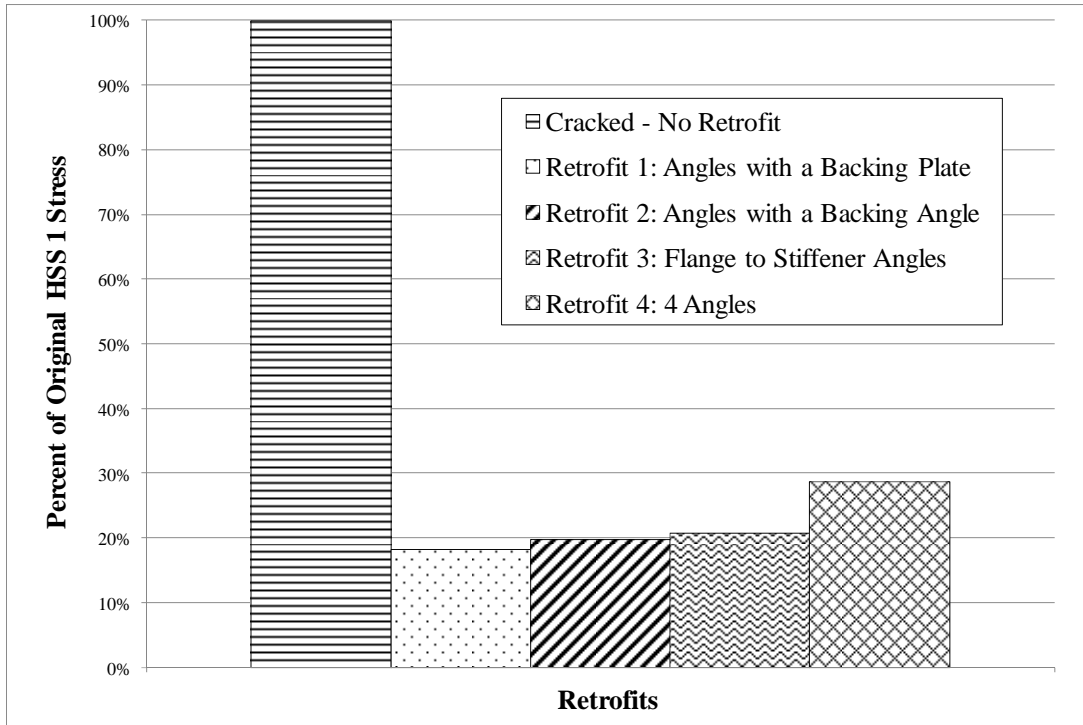
(a)
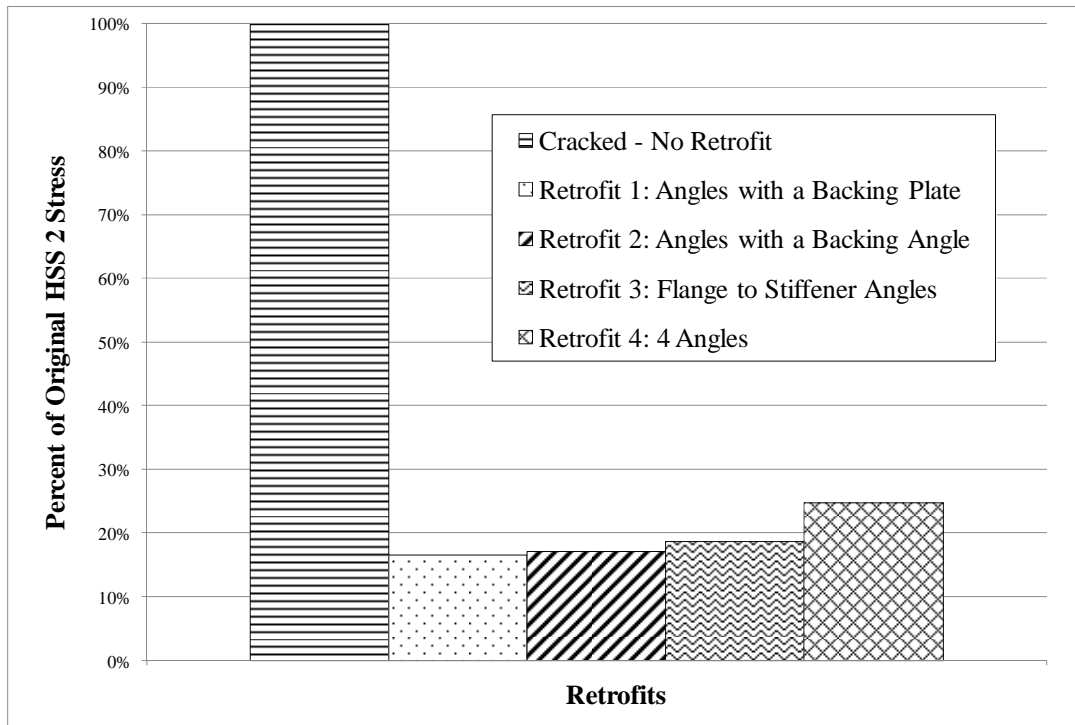
(b)

Figure 17. (a) Percent of original HSS 1 stress and (b) HSS 2 stress for four retrofits compared with an unretrofitted bridge. All models contain a 25-mm (1-in.) web-to-stiffener weld crack and a 51-mm (2-in.) web-to-flange weld crack.

Conclusions

Distortion-induced fatigue is a complex issue in steel bridges with varying problem locations depending on the bridge configuration. One retrofit does not always work for all bridge types or locations within a bridge due to bridge geometry. When selecting a retrofit it is also important to consider the amount of labor and materials required to install a retrofit. Based on the retrofits studied the following conclusions can be formed:

1. When 94-mm (3.7-in.) long angles were used with retrofit 1, HSS 1 decreased by 80% and HSS 2 decreased by 82% when compared to a cracked, unretrofitted bridge. When a longer angle, 305-mm (12-in.), was applied on the right side of the connection plate, HSS 1 and 2 decreased by an additional 2% and 1%, respectively. Although this did not seem to significantly reduce the stresses in the web gap region, the longer angle did stop the connection plate from deforming out-of-plane.

2. Retrofit 2 replaced the backing plate used in Retrofit 1 with a backing angle. Bolts were used to connect the backing angle to the web and bottom flange. The percentage of stress reduction was slightly greater than with Retrofit 1; HSS 1 decreased by 80% and HSS 2 decreased by 83%. With the increased amount of work required during installation with little additional stress reduction, the use of the backing angle is not merited.

3. Retrofit 3 involved bolting angles to the connection plate and bottom flange, which is a common retrofit in the field. When a 152×152×16-mm (6×6×0.63-in.) angle was applied, HSS 1 and 2 decreased by 72% and 77%, respectively. If the vertical leg of the angle on the right side of the connection plate was extended to 305-mm (12-in.), HSS 1 decreased by an additional 9% and HSS 2 an additional 6%.

4. The fourth retrofit required all cross-frames to first be removed due to the 305-mm (12-in.) long angles used in the bottom web gap of Girder C and the top web gap of Girder D. HSS 1 and HSS 2 stresses in the bottom web gap of Girder C were reduced by 71% and 75%, respectively. Retrofits 1 - 3 successfully reduced the stress in the web gap region without requiring removal of all cross-frames.

The angles with backing plate retrofit have been shown to be effective in a full bridge model. This retrofit is recommended in both the top and bottom web gaps because there are no conflicts with a concrete deck, the cross-frames do not need to first be removed, and minimal materials are required when applying the retrofit.

References

1. American Association of State Highway and Transportation Officials (AASHTO). (1983). *Standard Specifications for Highway Bridges*, Washington, D.C.

2. Grondin, G.Y., Fraser, R., and D'Andrea, M. (2002). "Testing and Evaluation of Fatigue Damaged Girders." *Fourth Structural Specialty Conference of the Canadian Society for Civil Engineers*, Montreal, Quebec, Canada, 1935-1944.

3. Fisher, J. W.,Jian, J., Wagner, D. C., and Yen, B. T. (1990). "Distortion-Induced Fatigue Cracking in Steel Bridges." *National Cooperative Highway Research Program Report #336,* Transportation Research Board, National Research Council, Washington, D. C.

4. Hassel, H., Bennett, C.R., Matamoros, A.B., Rolfe, S.T.

5. Hartman, A., Hassel, H., Adams, C. (2010) "Effects of Cross-Frame Placement and Skew on Distortion-Induced Fatigue in Steel Bridges." *Transportation Research Board of the National Academies*, 2200(8), 62-68.

6. Alemdar, F. (2011). "Repair of bridge steel girders damaged by distortion-induced fatigue," thesis, presented to University of Kansas, at Lawrence, KS, in partial fulfillment of the requirements for the degree of Doctor of Philosophy in Civil Engineering.

7. Nagati, A.D. (2012). "Repair of steel bridge girders damaged by distortion-induced fatigue," thesis, presented to University of Kansas, at Lawrence, KS in partial fulfillment of the requirements for the degree of Master of Civil Engineering.

8. Richardson, T.I., Alemdar, F., Bennett, C.R., Matamoros, A.B., Rolfe, S.T. (2012) "Evaluation of the performance of retrofit measures for distortion-induced fatigue using finite element analysis." *World Steel Bridge Symposium*.

9. Barker, R.M. and Puckett, J.A. (2007). Design of Highway Bridges: An LRFD Approach. Second Edition. Hoboken, NJ: John Wiley & Sons, Inc. (p. 725).

10. Fisher, J. W. and Mertz, D. R. (1984). "Fatigue and Fracture in Steel Bridges." *The Conference on Bridges*, Pittsburgh, PA, 10-21.

11. Barth (Grider), A.S. and Bowman, M.D. (2001). "Fatigue Behavior of Welded Diaphragm-to-Beam Connections." *Journal of Structural Engineering*, 127(10), 1145-1152.

12. AISC (2005). *Steel Construction Manual*, 13th Edition, American Institute of Steel Construction, Inc., Chicago, IL.

Appendix A: I-135 – 87 (43 and 44) Original Bridge Plans
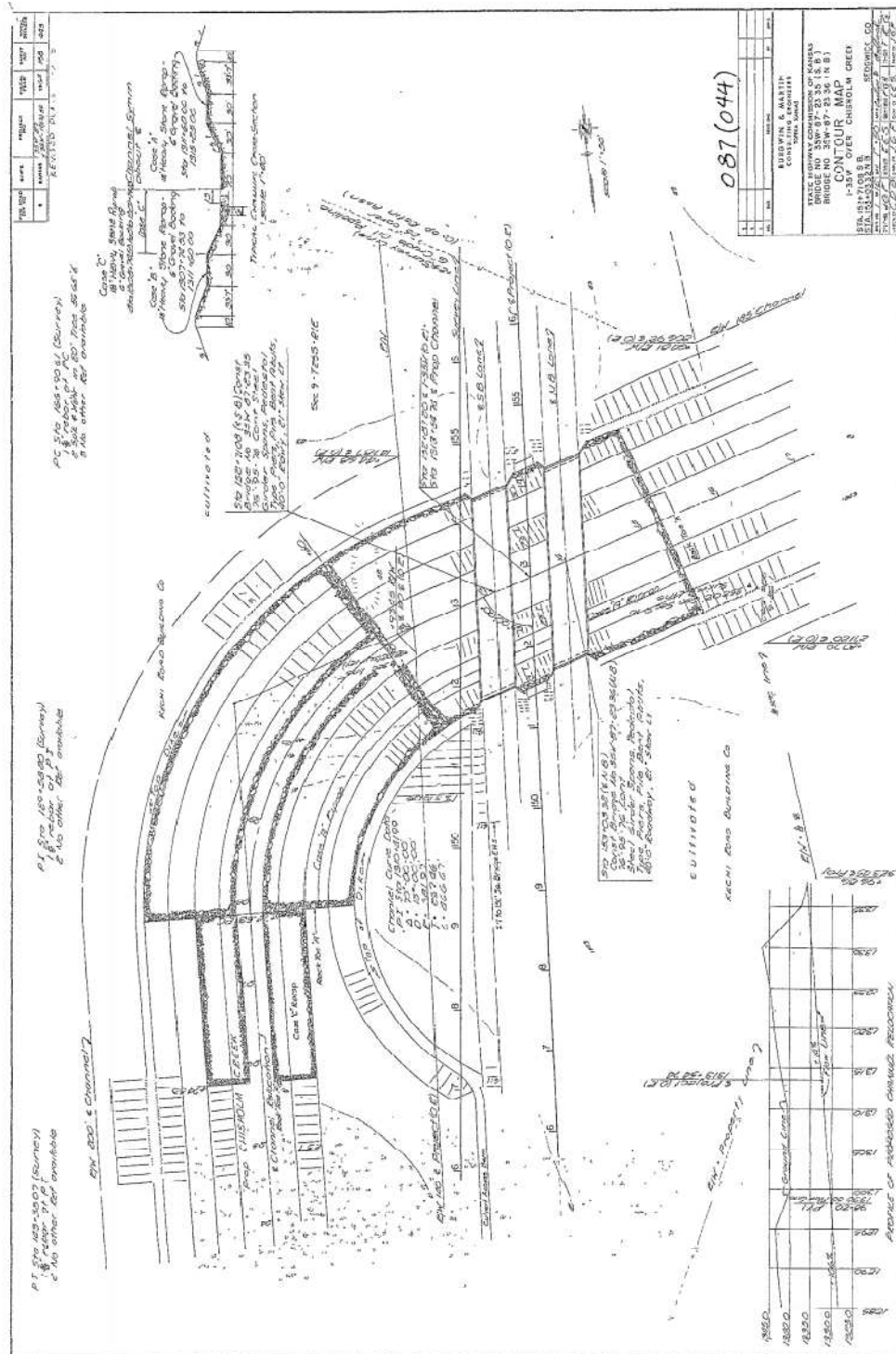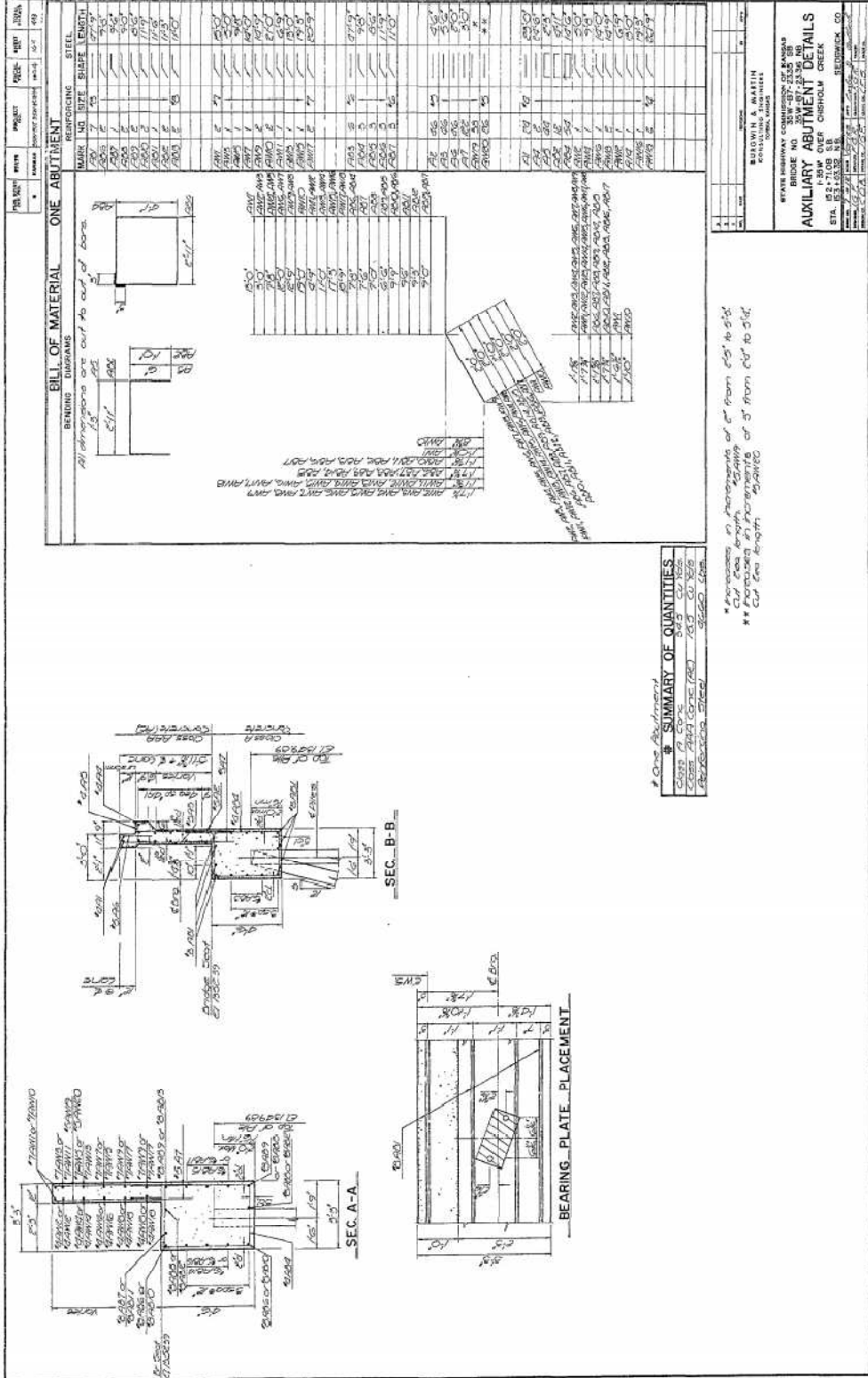

Figure A.1. Contour map.

Figure A.2. Construction layout of southbound I-135 bridge.

Figure A.3. Construction layout of northbound I-135 bridge.
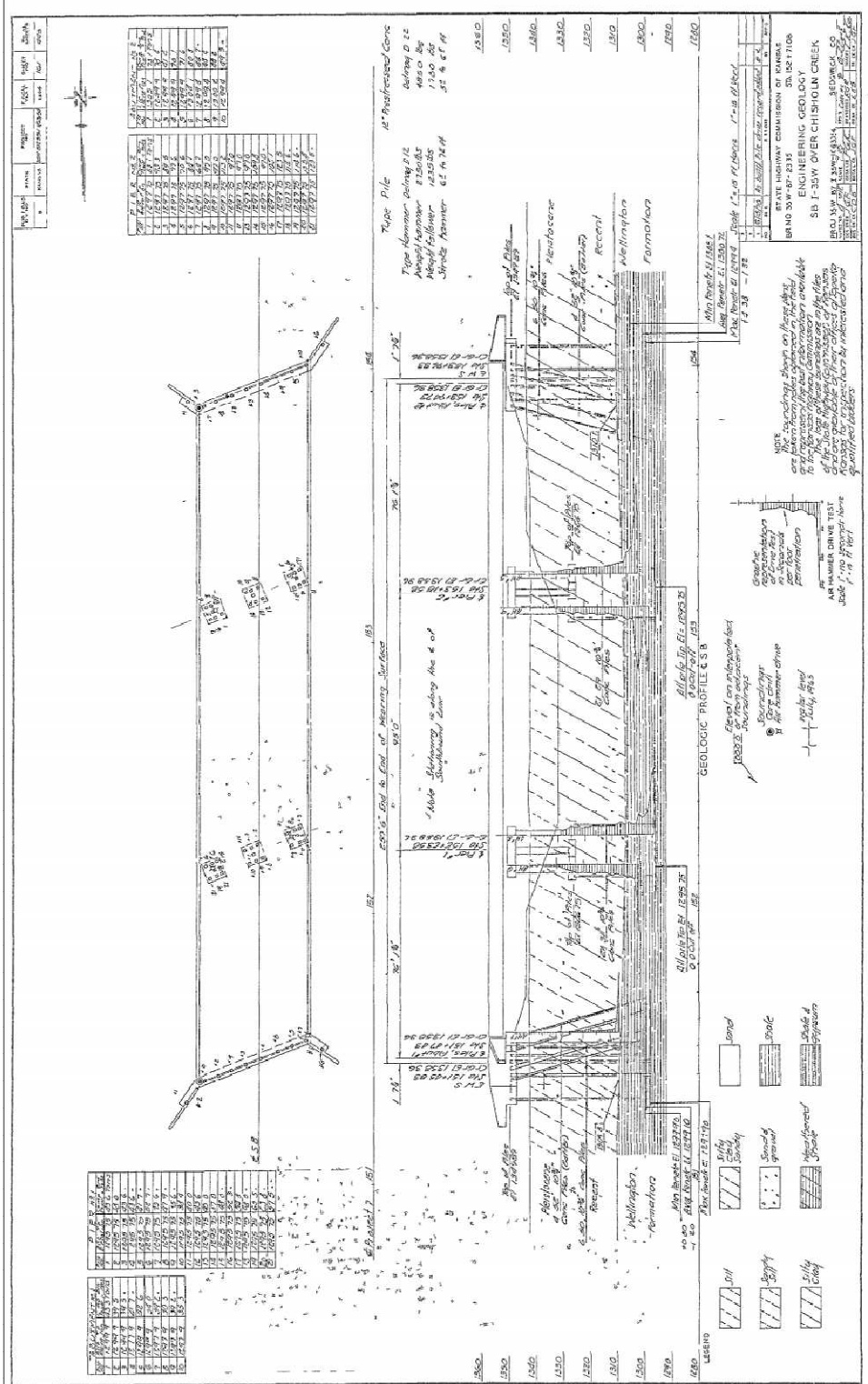
Figure A.4. Engineering geology.

Figure A.5. Abutment details.

Figure A.6. Auxiliary abutment details.

Figure A.7. Pier details.
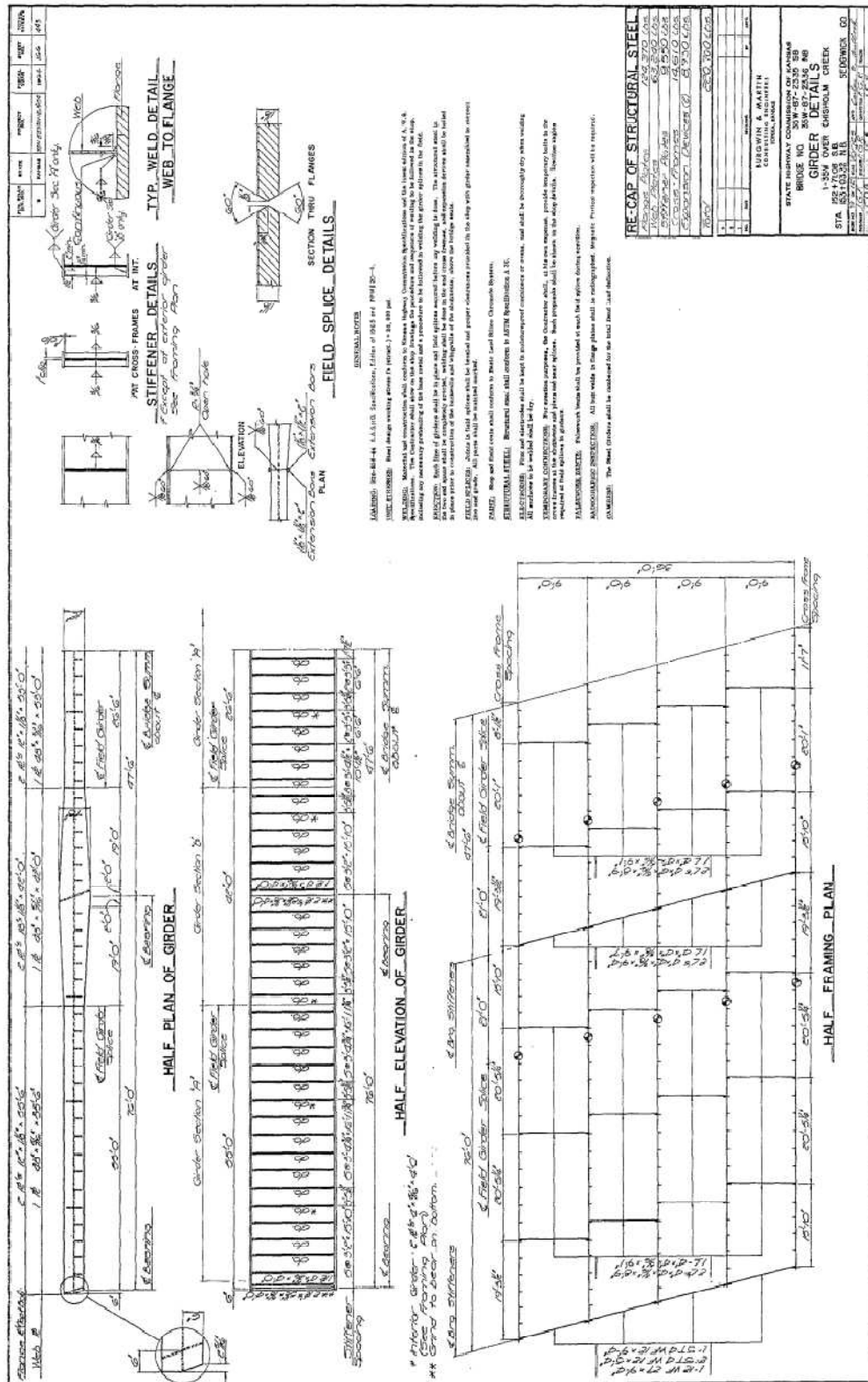
Figure A.8. Girder details.

Figure A.9. Concrete details.

Figure A.10. Bearing device details.
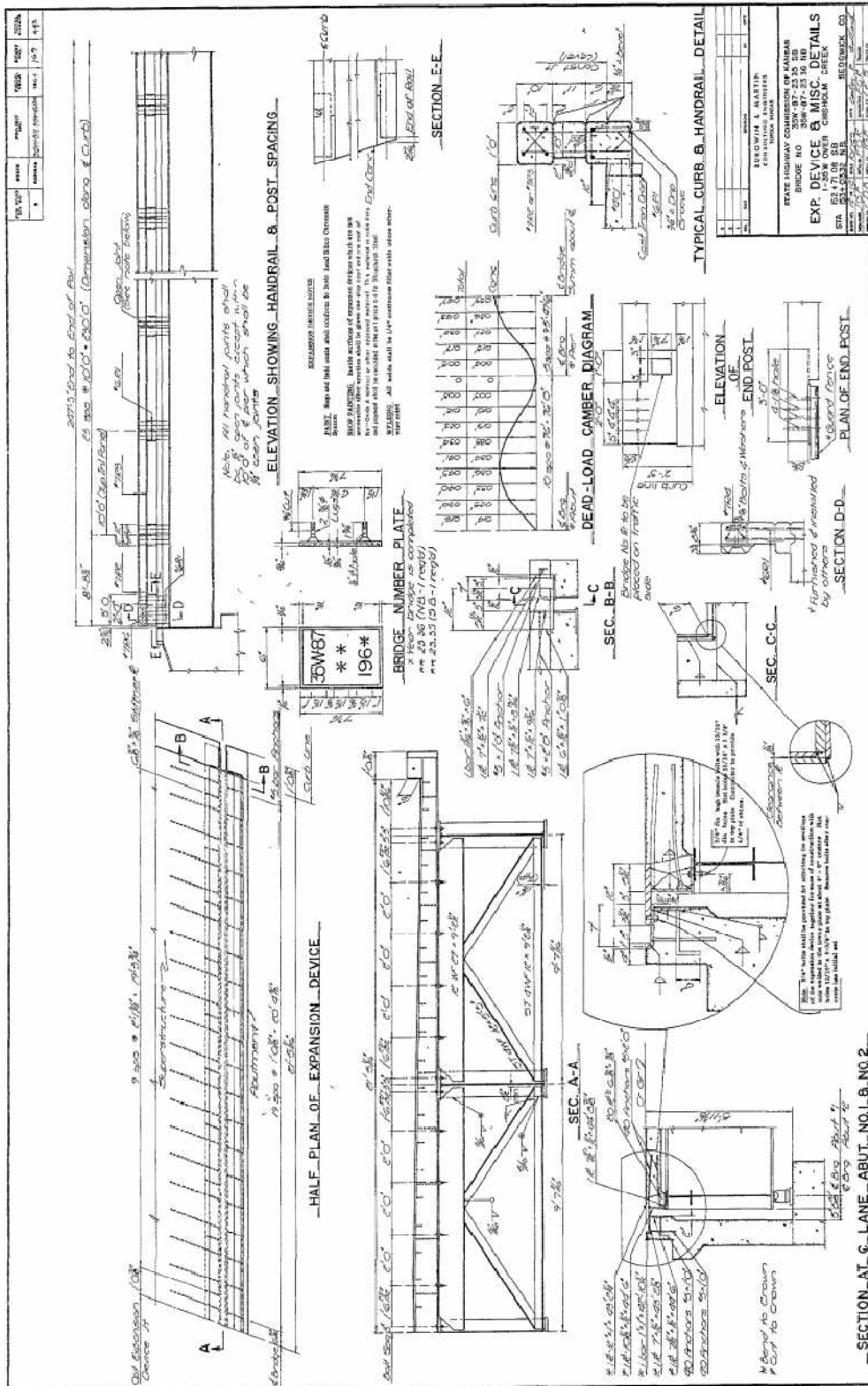
Figure A.11. Expansion device and miscellaneous details.

APPENDIX B: BOLT MODELING TECHNIQUES

Steps to create a bolt and apply a bolt load

1. Create a 3-dimensional shank and nut as two separate parts in the *Parts Module* with the diameter needed. The AISC Specification lists all bolts dimensions.

2. Apply section properties for the shank and nut.

3. Partition the shank perpendicular to its longitudinal axis in the middle of the shank.
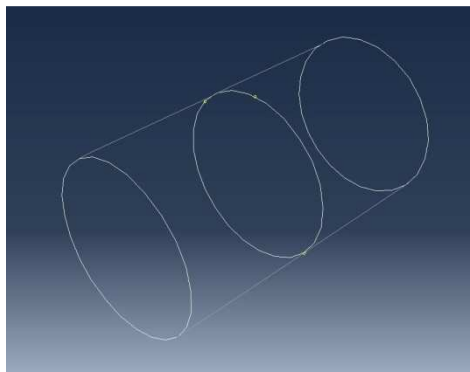
Figure B.1. Bolt in the *Parts Module* with a partitioned surface in the middle of the bolt.

4. Create a pre-tensioning step after the Initial Step and before the Load Step.

5. Insert one shank and two nuts into the *Assembly*. One nut will be the head of the bolt and the other will be the nut.
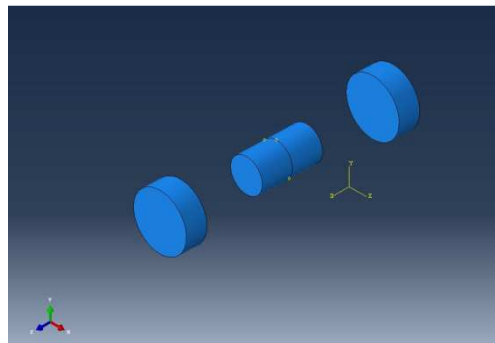
Figure B.2. One shank, head, and nut in the *Assembly*.

6. Merge the three parts into one bolt. Do not delete the old instances because they can be altered later to make bolts with different dimensions.
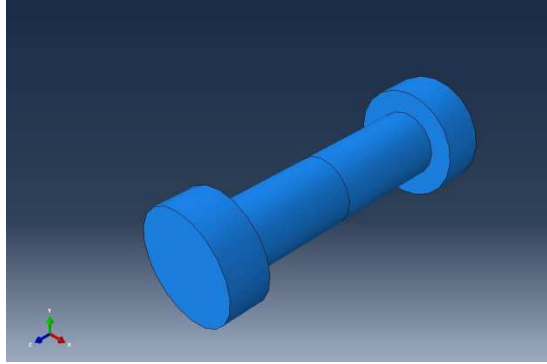
Figure B.3. All three bolt parts merged into one part.

7. Apply a pre-tensioning load to the interior surface of the shank based on the AISC Specification in the Pre-Tensioning Step. In the Loads Module select Create Load, and name the load. Choose the Pre-Tensioning Step, Mechanical under *Category*, select Bolt Load under the section entitled *Types for Selected Step*.
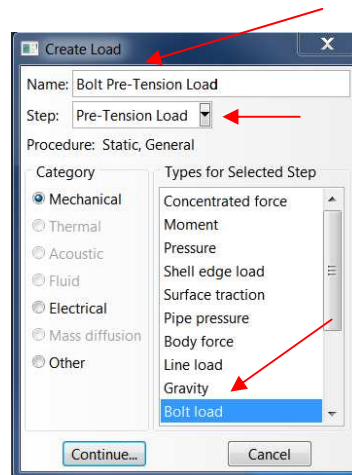

Figure B.4. The bolt load must be named. The bolt load should be applied in the step before the load is applied.

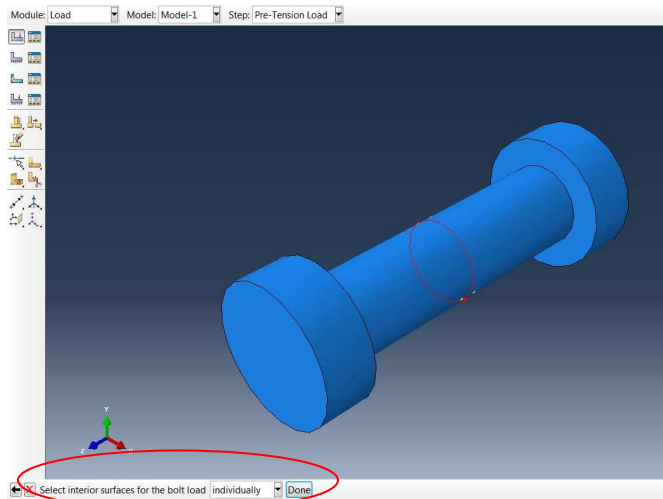8. The program will prompt you to select interior surfaces for the bolt load.

Figure B.5. Apply bolt load to the interior surface of the shank.

9.   Next it will ask you to choose a side for the shell or internal faces- brown or purple. Select

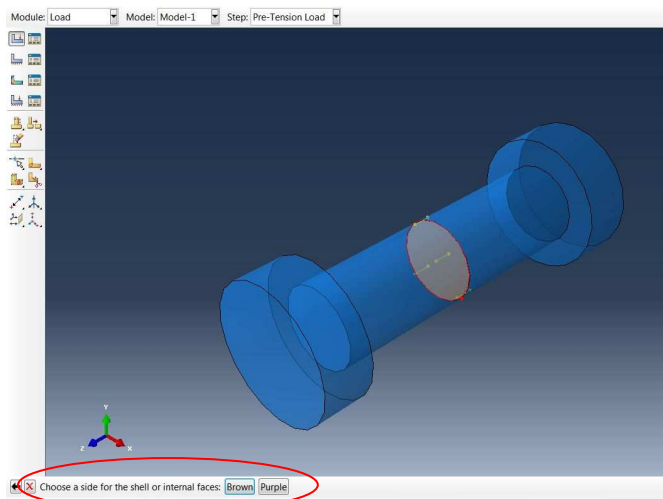the color that appears on the interior surface you selected.

Figure B.6. Select a side for the internal surface depending on what color is shown. In this figure, the interior surface is highlighted brown, therefore select brown.

10. Select the datum axis that is aligned with the bolt centerline. This specifies in what direction

the load will be applied. Frequently you have to display all instances in order to see the
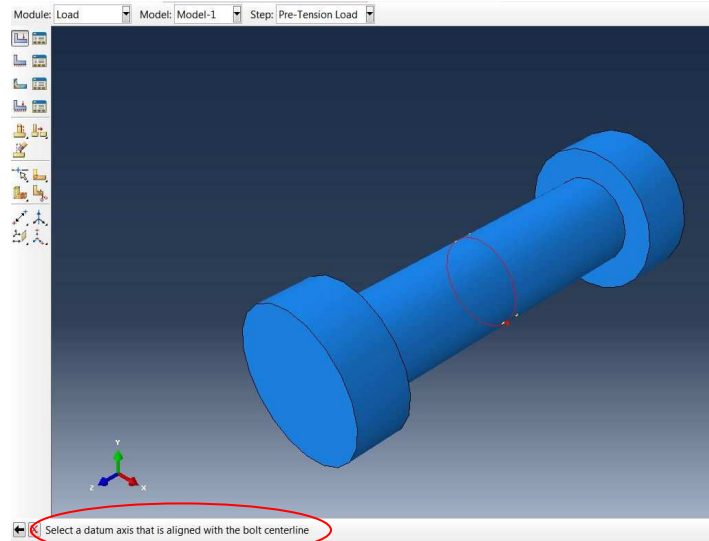
datum axis.

Figure B.7. Select the datum axis that corresponds to the longitudinal axis of the bolt. In this case, the datum axis should be z.
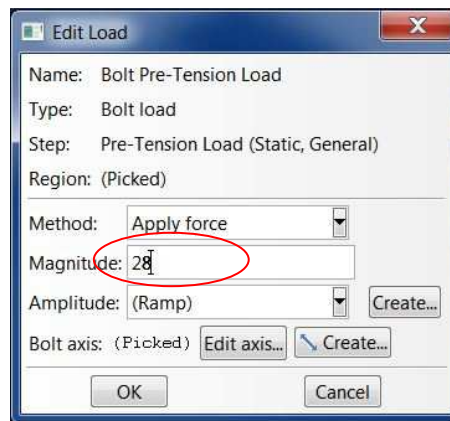
11. Enter the pre-tensioning load.

Figure B.8. Enter the bolt load found in the AISC Specification.

12. Select the loading step next. From the drop down menu to the right of *Menu*, click on *Fix at current length*. This stops the tensioning load during the loading step.
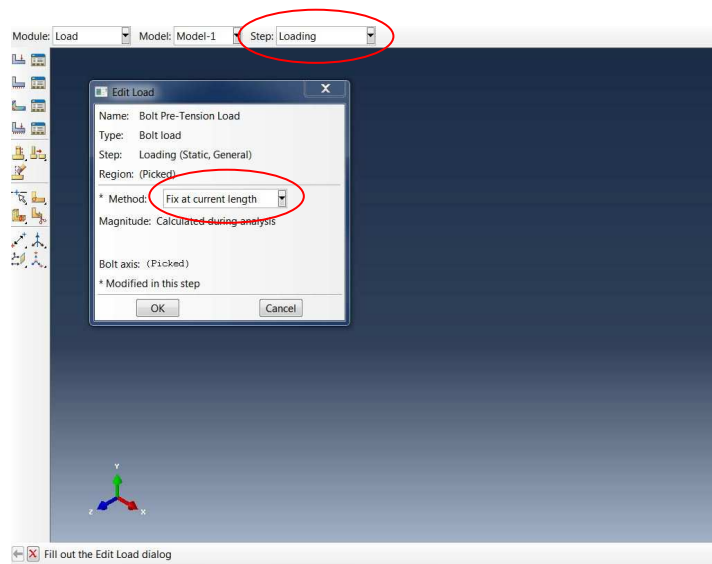
Figure B.9. Fix the length of the bolt in the step where a global load is applied to the model. This stops the bolt from continuing to have a pre-tension load.

13. Tie the back of the head/nut to the front of the steel surface you are bolting to.

14. Create an interaction between the shank of the bolt and the hole that the bolt will go into to

    avoid the two surfaces from intersecting each other.